creative commons

COMMONS DEED

저작자표시 2.0 대한민국

이용자는 아래의 조건을 따르는 경우에 한하여 자유롭게

- 이 저작물을 복제, 배포, 전송, 전시, 공연 및 방송할 수 있습니다.
- 이차적 저작물을 작성할 수 있습니다.
- 이 저작물을 영리 목적으로 이용할 수 있습니다.

다음과 같은 조건을 따라야 합니다:

저작자표시. 귀하는 원저작자를 표시하여야 합니다.

- 귀하는, 이 저작물의 재이용이나 배포의 경우, 이 저작물에 적용된 이용허락조건을 명확하게 나타내어야 합니다.
- 저작권자로부터 별도의 허가를 받으면 이러한 조건들은 적용되지 않습니다.

저작권법에 따른 이용자의 권리는 위의 내용에 의하여 영향을 받지 않습니다.

이것은 이용허락규약(Legal Code)을 이해하기 쉽게 요약한 것입니다.

Disclaimer

dCollection

[UCI]I804:48009-200000171981

Doctor of Philosophy

Density Functional Study of Ionic Adsorption and Diffusion on Two-Dimensional Materials

The Graduate School

of the University of Ulsan

Department of Physics

Abdus Samad

Density Functional Study of Ionic Adsorption and Diffusion on Two-Dimensional Materials

Supervisor: Prof. Young-Han Shin

This dissertation is submitted to University of Ulsan in partial fulfillment of
the requirements for the degree of
Doctor of Philosophy in physics

by

Abdus Samad

Department of Physics
University of Ulsan
February, 2019

University of Ulsan

Department of Physics

This dissertation, "Density Functional Study of Ionic Adsorption and Diffusion on Two-Dimensional Materials" is hereby approved in partial fulfillment of the requirements for the degree of Doctor of Philosophy in physics.

Committee Chair: Prof. Tae Heon Kim
Department of Physics, University of Ulsan

Myg Won Lee

External Examiner: Prof. Myung Won Lee
Department of Chemistry,
Pukyong National University, Busan

류 광 선

Examiner: Prof. Ryu Kwang-Sun
Department of Chemistry, University of Ulsan

Examiner: Dr. Hye Jung Kim
Department of Physics, University of Ulsan

YoungHan Shin

Supervisor: Prof. Young-Han Shin
Department of Physics, University of Ulsan

Dedicated to my loving parents, elder brother Mukhtar Ali, and niece Nida Mukhtar

Declaration

I hereby declare that except where specific reference is made to the work of others, the contents of this dissertation are original and have not been submitted in whole or in part for consideration for any other degree or qualification in this, or any other university.

Abdus Samad

Acknowledgments

I would like to express my sincere gratitude to my supervisor Prof. Young-Han Shin for giving me the opportunity to work in the *Multiscale Materials Modeling Lab*. of the University of Ulsan. His continuous support is essential to everything I have achieved in my Ph.D. time. He teaches me almost everything related to research from the basics of density-functional theory to the writing of a scientific paper. Special thanks to Dr. Hye Jung Kim for her continues and selfless support. I also want to thank all the other colleagues and friends. Finally, exceptional thanks to my loving parents, other family members, and friends for their mental and moral support.

List of Publications

1. **Abdus Samad**, Mohammad Noor-A-Alam, Young-Han Shin "First principles study of a SnS_2/graphene heterostructure: a promising anode material for rechargeable Na ion batteries" *J. Mater. Chem. A* **2016**, 4, 14316

2. **Abdus Samad**, Aamir Shafique, Young-Han Shin "Adsorption and diffusion of mono, di, and trivalent ions on two-dimensional TiS_2" *Nanotechnology* **2017**, 28, 175401

3. **Abdus Samad**, Aamir Shafique, Hye Jung Kim and Young-Han Shin "Superionic and electronic conductivity in monolayer W_2C: *ab initio* predictions" *J. Mater. Chem. A* 2017, 5, 11094

4. **Abdus Samad**, Young-Han Shin "MoS_2@VS_2 Nanocomposite as a Superior Hybrid Anode Material" *ACS Appl. Mater. Interfaces* **2017**, 9, 29942

5. **Abdus Samad**, Hye Jung Kim, Young-Han Shin "Stability, spontaneous and induced polarization in monolayer MoC, WC, WS, and WSe" *J. Phys.: Condens. Matter* **2019**, 31, 045301

6. **Abdus Samad**, Hye Jung Kim, Young-Han Shin "Structure Stability and High Li Storage Capacity of the Unzipped Graphene Oxide Monolayer" *Appl. Surf. Sci.* DOI https://doi.org/10.1016/j.apsusc.2018.12.116

Abstract

Search for efficient functional nanomaterials for the future nanotechnology is one of the main focus of the material scientists and engineers. Computational methods have been playing a leading role in the atomistic understandings of structure and properties analysis of nanomaterials for the last two decades. The central theme of this thesis is to use density functional theory calculations to introduce new nanomaterials with boosted efficiency and understand the physics and chemistry behind it.

Rechargeable Li ion batteries (LIBs) are playing a crucial role in the development of portable electronic technology. On the other hand, to avoid global warming and reduce the dependence on the limited energy fossil fuel, sustainable energy resources should be utilized. Since the production of energy from such resources fluctuates highly, short time storage of energy is needed. In this context, we studied different anode materials for LIBs and possible alternatives to boost their efficiency, lower the cost and toxicity. Experimentally possible nanosheets of the TiS_2, W_2C, and unzipped graphene oxide (UGO) have been considered for metal ion adsorption and diffusion. These materials are found to have high metal ion storage capacity, high electronic and ionic conductivity and suitable anodic open circuit voltage. Monolayer SnS_2 has high Na storage capacity, but its high expansion under sodiation and poor electrical conductivity are barriers to be used as anode. On the other hand, graphene is metallic and mechanically very strong, but its Na binding energy is not enough to be used as an anode. A heterostructure of graphene and SnS_2 becomes a perfect anode material where all the problems are solved adequately. Similarly, the stable monolayer MoS_2 has a high band gap and low Li/Na storage capacity while monolayer VS_2 is metallic and has a high Li/Na storage capacity, but it is chemically unstable. Suspended single-layer of VS_2 is not grown in the laboratory till today. Because of low lattice mismatch and similar geometry, it is easy to make VS_2/MoS_2 heterostructure. The heterostructure stabilizes of the VS_2 layer and boosts the Li/Na capacity of MoS_2 simultaneously. The enhancement in stability and electrochemical performance of the VS_2/MoS_2 nanocomposite is attributed to the charge redistribution in the formation of the nanocomposite.

Besides new anode materials for rechargeable LIBs, we also report on the possible existence of new single-layer materials, namely MoC, WC, WS, and WSe. These materials have

spontaneous switchable out-of-plane polarization. An in-plane uniaxial or biaxial strain can change the magnitude of the out-of-plane polarization while to produce the in-plane piezoelectric effect, a uniaxial strain along the armchair direction is necessary.

Contents

Contents **vii**

List of Figures **xi**

List of Tables **xvii**

1 Introduction **1**
- 1.1 2D materials 1
- 1.2 The least stability criteria 2
  - 1.2.1 Environmental Stability 6
- 1.3 Classification of monolayers 6
  - 1.3.1 Structure-Based Classification 7
  - 1.3.2 Properties Based Classification 10
- 1.4 Van der Waals heterostructures 11
- 1.5 Motivation 12

2 First-principles Tools **15**
- 2.1 The Schrödinger Equation 15
- 2.2 The Hartree-Fock method 17
- 2.3 The Density Functional Theory 18
- 2.4 The Kohn-Sham Formulation 18
- 2.5 Approximations used in Exchange-Correlation Functional 19
  - 2.5.1 Local Density Approximation (LDA) 19
  - 2.5.2 Generalized Gradient Approximation (GGA) 19
  - 2.5.3 The Hybrid Functionals 20
- 2.6 Blöch states 20
- 2.7 Pseudopotentials and Projector augmented waves (PAW) 21
  - 2.7.1 Pseudopotentials 21
  - 2.7.2 PAW 22

3 TiS_2 sheet as anode material 23
3.1 Introduction . . . 23
3.2 Computational details . . . 24
3.3 Results and discussion . . . 25
  3.3.1 Structure and adsorption sites . . . 25
  3.3.2 Adsorption and specific capacity . . . 26
  3.3.3 Voltage . . . 28
  3.3.4 Diffusion of metal ions . . . 29
  3.3.5 Electronic properties . . . 30
3.4 Conclusions . . . 31

4 Monolayer W_2C as anode material 33
4.1 Introduction . . . 33
4.2 Computational details . . . 34
4.3 Results and discussion . . . 35
  4.3.1 Structural stability . . . 35
  4.3.2 Adsorption . . . 37
  4.3.3 Diffusion . . . 42
4.4 Conclusions . . . 43

5 Structure and applications of the UGO monolayer 45
5.1 Introduction . . . 45
5.2 Computational details . . . 46
5.3 Results and discussion . . . 47
  5.3.1 Energetic and dynamic stability . . . 47
  5.3.2 Li adsorption capacity . . . 50
  5.3.3 Open circuit voltage . . . 53
  5.3.4 Diffusion . . . 54
  5.3.5 Electronic properties . . . 55
5.4 Conclusions . . . 56

6 Polarization in the MX monolayers 57
6.1 Introduction . . . 57
6.2 Computational details . . . 58
6.3 Results and discussion . . . 59
  6.3.1 Structure stability . . . 59
  6.3.2 Spontaneous Polarization and Piezoelectricity . . . 61

6.4 Conclusions . . . 66

7 **SnS_2/graphene as anode material** **67**
7.1 Introduction . . . 67
7.2 Computational methods . . . 68
7.3 Results and discussion . . . 69
7.3.1 1T SnS_2 monolayer . . . 69
7.3.2 Na adsorption at the SnS_2 surface . . . 69
7.3.3 Na diffusion on the SnS_2 surface . . . 73
7.3.4 Na insertion in the SnS_2/graphene heterostructure . . . 75
7.3.5 Na diffusion in the SnS_2/graphene heterostructure . . . 77
7.3.6 Electronic structure . . . 78
7.3.7 Mechanical stability . . . 79
7.4 Summary . . . 80

8 **MoS_2@VS_2 as a superior anode** **83**
8.1 Introduction . . . 83
8.2 Computational details . . . 85
8.3 Results and discussion . . . 85
8.3.1 Adsorption and diffusion of Li/Na ions on MoS_2, VS_2 . . . 85
8.3.2 Stacking stability . . . 87
8.3.3 Adsorption and diffusion in MoS_2@VS_2 . . . 90
8.4 Conclusions . . . 93

9 **Summary** **97**

References **99**

List of Figures

1.1 Energy against lattice constants for silicene and germanene in planer (PL), low-buckled (LB), and high buckled (HB) structures. Reproduced from reference [19]. 3

1.2 (a) Top and side views of the penta-graphene. The yellow and black colored spheres are for sp^3 and sp^2 carbon atoms respectively. (b) Phonon band structure and corresponding density of states for penta-graphene. Reproduced from reference [21]. 4

1.3 Prototype structures for two-dimensional materials. Row 1 shows side and top views for (a) graphene, (b) silicene, (c) black phosphorene, (d) blue phosphorene (e) β borophene. Row 2 shows side and top views for monolayer (a) $h-$BN, (b) SiS, (c) SnO, (d) SnSe, (e) InSe. Row 3 shows side and top views of monolayer (a) 2H MoS_2, (b) 1T SnS_2, (c) 1T′ $MoTe_2$, (d) 1T″ WS_2. Row 4 shows side and top views of monolayer (a) $PdSe_2$, (b) TiS_3, (c) VBr_2, $CrCl_3$. Row 5 shows the side and top views of monolayer (a) Mo_2C, (b) $MnSiCl_3$, and (c) Bi_2Te_2Se. 8

1.4 Construction of a heterostructure of different layered materials. Reproduced from reference [64] 11

3.1 Top and side views of the monolayer TiS_2 (a) in 1T and (b) 2H phases. The black and light green colored spheres represent Ti and S atoms, respectively. . 25

3.2 Formation energy (E_f) of monolayer TiS_2 with Li, Na, K, Be, Mg, Ca, or Al atoms on the H-site as a function of metal ion concentration. 28

3.3 (a) A comparison of the open circuit voltage of different metal ions adsorbed at H-sites of the monolayer TiS_2 as a function of metal ion content (n). (b) A comparison of the averaged open circuit voltage of the monolayer TiS_2 as an anode material for different metal ions in the range of $1 \leq n \leq 9$. 29

3.4 Relative energy profile for the diffusion of (a) monovalent and (b) divalent metal ions on the surface of monolayer TiS_2 from an H-site to its nearest neighboring H-site via the T-site between these two H-sites. (c) Top and side views of the trajectory of Li ion diffusion over the surface of monolayer TiS_2. The trajectories for the diffusion of other metal ions are similar to that for Li. 30
3.5 Total density of states for (a) TiS_2, (b) Li_1TiS_2, (c) Na_1TiS_2, (d) K_1TiS_2, (e) Mg_1TiS_2, and (f) Ca_1TiS_2. It shows that TiS_2 is a semimetallic with a small bandgap of 0.62 eV in its pristine state, but becomes metallic after the adsorption of metal ions. The data shown here is calculated by the HSE06 method. . 31

4.1 Top and side views of a portion of monolayer W_2C in the 2H phase. (b) Left-hand panel: phonon modes for the 1T phase of the monolayer W_2C, showing that the 1T phase is dynamically stable. Right-hand panel: phonon modes for the 2H phase of monolayer W_2C, showing that the 2H phase is dynamically stable. (c) Snapshot of the 2H phase of monolayer W_2C taken after 1000 steps at 300 K, showing that the monolayer is stable at room temperature. (d) Electronic band structure and density of states of the monolayer W_2C (the Fermi level is scaled to zero), showing that the pristine monolayer W_2C is metallic. 36
4.2 Top and side views of the charge density difference ($\Delta\rho$) for Li (left-hand panel) or Na (right-hand panel) adsorbed at the H-site of the monolayer W_2C. Electron gain upon Li/Na adsorption is indicated in yellow at an isosurface of 1.89×10^{-3} e/Å^3 and loss in light blue at an isosurface of 1.89×10^{-3} e/Å^3. . . 38
4.3 Top and side views of the adsorption sites at high concentrations (14 atoms per supercell) of Li (left-hand panel) and Na (right-hand panel). Li atoms are fixed to the energetically favorable H- or C-sites. Na atoms are uniformly distributed over the surface of the monolayer W_2C irrespective of the favorable adsorption sites. 39
4.4 (a) Total formation energy ($E_{b(x)}$) and (b) OCV versus concentration of A-adatoms on a $3\times3\times1$ W_2C supercell. After loading 14 Na ions, no further Na storage is possible. In the Li adsorption case, all the top and bottom H-sites can be filled without the formation of metallic clusters. 40
4.5 Partial density of states per atom for (a) 1-Li-, (b) 1-Na-, (c) 18-Li-, and (d) 14-Na-adsorbed monolayer W_2C in a $3\times3\times1$ supercell. 41
4.6 (a) Relative energy profile for the diffusion of Li/Na from an H-site to a nearby H-site through three different paths, where path 1 has the lowest energy barrier. (b) Schematics of the different diffusion paths. 43

5.1 Top panel shows the side and top views of possible geometries for UGO monolayer based on the electric dipole configurations. (a) All the dipoles aligned in the same direction, (b) alternating up and down dipoles along both the armchair and zigzag directions, (c) dipoles parallel along the armchair direction and alternating along the zigzag direction, (d) dipoles parallel along the zigzag direction and alternating along the armchair direction. The cross (⊗) and dot (⊙) symbols indicate the directions of local dipole moments induced by oxygen atoms while the rectangles show the unit cells. The configuration (d) is energetically the most stable, and the relative energies of four configurations are given below the top paneleach configuration. The yellow and red colored spheres represents C and O atoms, respectively. Bottom panel shows the phonon dispersion curves corresponding to the configurations (a-d). 48

5.2 The upper panel of (a), (b), (c), (d), and (e) shows the top and side views of the MLWFs associated with the non-bonding sp^2-like lone pairs, p-like lone pairs, C-O σ bonds, a C-C σ bond, and a C-C π bond, respectively. The lower panel of (a), (b), (c), (d), and (e) shows the contribution of each MLWF in the electronic band structure with a color scale. 49

5.3 Top and side views for Li adsorption sites and charge density difference between the Li adsorbed UGO monolayer and the UGO monolayer and Li atoms at the adsorption sites (a) O_{TC}, (b) C_T, (c) OC, (d) O_B, (e) O_{BC}, and (f) O_T. The electron depletion upon Li adsorption is presented by blue color at the isosurface of -2$\times$10^{-3} e/Å^3 while the electron accumulation is shown by purple color at the isosurface of 2$\times$10^{-3} e/Å^3. The Li atom in the top and side views is indicated by arrows. 51

5.4 Open circuit lithiation voltage of the UGO monolayer. Insets show the top views of Li attachment with the UGO monolayer while one at the right top corner shows the perspective view for a fully lithiated UGO monolayer. The grey colored spheres are for Li adsorbed at the lower and top surfaces of the UGO monolayer. 52

5.5 Minimum energy path for Li diffusion on the UGO monolayer, from a stable OC-site to a nearby OC-site via a metastable C_T-site. The Li diffusion trajectory along the minimum energy path is shown. 54

5.6 Electronic band structure and total density of states of the UGO monolayer calculated with the PBE functional. The Dirac cone between the Y and Γ points shows that this material can have high electron and hole mobilities. The band gap of the UGO monolayer calculated with the HSE06 functional is 0.6 eV. Band structure near the Dirac cone is magnified in the inset at left. . . 55

6.1 The top and side views of (a) buckled and (b) flat geometries of monolayer WC and (c) the top view of the electronic charge distribution (light green color shows electron density at the isosurface of 8×10^{-2} e/Å^{-3}) in the buckled monolayer WC. The dark pink and brown colored spheres are for W and C atoms respectively. 59

6.2 Molecular dynamics simulations of the MX monolayers 60

6.3 Paraelectric and antiferroelectric structures for monolayer WC. 61

6.4 Stable phonon dispersion modes for the buckled hexagonal MX monolayers . 62

6.5 Energy barriers for ferroelectric-to-paraelectric phase transition for the MX monolayers. The schematic figures of the atomic configurations at each image are shown with purple circles for Mo and W and brown circles for C, S, and Se. 63

6.6 The change in polarization (P_z) is linear under uniaxial strain along x or y directions. The inset shows the direction of the polarization for the MX monolayers. 64

6.7 Band structures and total density-of-states for monolayer (a) MoC, (b) WC, (c) WS, and (d) WSe. Fermi-level is set to the top of the valence band. The band structures of monolayer MoC and WC resemble Mexican-hat band dispersions at the K symmetry point. 65

7.1 Top and the side views of a portion of monolayer SnS_2 with (left panel) Na at an H-site, (middle panel) Na at a T-site, and (right panel) monolayer SnS_2 with all top and bottom H-sites occupied by Na. The black, green, and blue solid spheres represent Sn, S, and Na atoms respectively. 70

7.2 (a) E_b of the Na adatom, on the H-sites of monolayer SnS_2 and interface H-sites of the SnS_2/graphene heterostructure, (b) averaged net charge on Na, and (c) percent change in the area as a function of increasing Na content (x). . . . 72

7.3 (a) MEP for the Na diffusion from one H-site to the adjacent H-site via a T-site with an energy barrier of 0.13 eV. Trajectory of Na along the H–T–H path is shown in the inset. (b) MEP for the Na diffusion from one H-site to the adjacent H-site via a top S-site with an energy barrier of 0.60 eV. The trajectory of Na diffusion along the H–S–H path is shown in the inset. 74

7.4 MEP for Na diffusion in the SnS_2/graphene heterostructure. The structure at the top left corner is the side view of the heterostructure with all the interface H-sites filled with Na. The structure at the top right corner is the top view of the SnS_2/graphene heterostructure, and the zigzag trajectory of Na along H1–T1–H3–T3–H1 is shown by the blue colored solid spheres. 77

7.5 Total DOS (a) for the $2\times2\times1$ SnS_2 and $3\times3\times1$ graphene heterostructure, (b) $3\times3\times1$ SnS_2 with all the top and bottom H-sites occupied by Na, and (c) $3\times3\times1$ pristine SnS_2 shows different band gaps ranging from 0 to 1.54 eV. . 79

8.1 Relative energy profiles through the minimum energy paths for the diffusion of Li/Na ions on the surface of (a) monolayer MoS_2 from Mo_{sur} site to Mo_H site and (b) monolayer VS_2 from the V_{sur} site to the V_H site. 87

8.2 Top and side views of (a) AA stacking, (b) AB stacking, (c) S atom of MoS_2 above the V atom of VS_2, and (d) S atom of VS_2 above the Mo atom of MoS_2 of monolayer MoS_2 and VS_2. Values given with the top views show the stacking energy in eV/atom; values given with the side views show the vertical distance between Mo and V in Angstroms. Dark blue and yellow spheres represent the S atoms of monolayer VS_2 and monolayer MoS_2, while red and gray spheres are for V and Mo, respectively. Stacking order shown in d is energetically the most stable stacking. 88

8.3 Top and side views of the charge density difference ($\Delta\rho$) of the $MoS_2@VS_2$ nanocomposite and monolayer MoS_2 and monolayer VS_2. Electron gain is indicated by yellow at the isosurface of 2.5×10^{-4} $|e|/Å^3$ and loss by light blue at the isosurface of 2.5×10^{-4} $|e|/Å^3$. 89

8.4 (a) Phonon dispersion modes for the $MoS_2@VS_2$ nanocomposite. (b) Electronic band structure and total density of states for the $MoS_2@VS_2$ nanocomposite. 90

8.5 Schematic view of the Li/Na adsorption sites on the surfaces and interface of the $MoS_2@VS_2$ nanocomposite 91

8.6 Total binding energy of Li/Na adsorption as a function of increasing specific capacity 92

8.7 Top and side views of maximum possible Li storage (584 mAh/g) in $MoS_2@VS_2$ nanocomposite. Both layers of the heterostructure maintain their structure shape, but the interlayer distance is increased by 2.99 Å. 92

8.8 Minimum energy paths and saddle points for the diffusion of a Li/Na ion (a) from a V_{sur} site to a nearby V_H site on the VS_2 surface of MoS_2@VS_2 nanocomposite and (b) from a Mo_{sur} site to a nearby Mo_H site. Insets of (a) and (b) show the pathways. Energies of the saddle points are given in eV. . . 94

8.9 Minimum energy path for the diffusion of a Li/Na ion at the interface from a V_i site to a nearby V_{Hi} site. Inset shows the diffusion path schematically. . . 94

List of Tables

3.1 Formation energy, charge, and M-S bond distance of a single metal ion, when adsorbed at the H- and T-sites. 27

4.1 Distance from W (d), binding energy (E_b), and charge transferred (q) by Li/Na adatoms on adsorption at the H- (hollow) or C-site (above-carbon) of monolayer W_2C 35

5.1 Binding (E_b) and adsorption (E_{ad}) energies and Bader charges (q) of a Li atom on $C_{16}O_4$ monolayer adsorbed at sites as shown in Fig. 5.3. The OC site is found to be energetically the most favorable one whereas the O_B and O_{BC} sites are equally favorable for Li adsorption. 49

6.1 Energy of buckled structures relative to their flat allotropes per unit cell (ΔE in eV), lattice constant (a in Å), bond distances (M-X in Å) and vertical distances (d_z in Å) between M and X atoms in the buckled structures, band gap calculated with the HSE06 functional (E_g in eV), Bader charges on M and X atoms (q in e), spontaneous polarization (P_s in pC/m), polarization switching barrier (E_b in eV), and piezoelectric stress coefficients ($e_{31} = e_{32}$ and $e_{22} = e_{12}$ in 10^{-10} C/m) for MX monolayers 62

6.2 In-plane elastic constants (C_{11}, C_{12}), Young's modulus (Y), and Poisson's ratio (ν) calculated for MX monolayers. 63

7.1 Geometric parameters, charge, and energetics of a single Na adsorption on a $3\times3\times1$ SnS_2 supercell. 70

7.2 Net charge (q), binding energy (E_b), and nearest Na-to-S distance ($d_{\mathrm{Na-S}}$) of a single Na adsorbed at the H-sites of the interface (H1-, H2-, H3-, and H4-), T-sites of the interface (T1-, T2-, T3-, and T4-), an H-site of the SnS_2 surface (H_S -site), a T-site of the SnS_2 surface (T_S-site), and above the center of a graphene ring (G_{cen}) of the SnS_2/graphene heterostructure 75

7.3 In-plane Young's modulus (Y), Poisson's ratio (ν), and elastic moduli (C_{11} and C_{12}) for monolayers of graphene, MoS_2, SnS_2, and SnS_2 with all top H-sites filled with Na and heterostructures of SnS_2/graphene and SnS_2/graphene with all interface H-sites filled with Na 78

8.1 Formation energy, charge, and M-S bond distance of a single metal ion, when adsorbed at the H- and T-sites. 86

8.2 Binding energy (E_b) and charge (q) transferred from Li/Na atoms intercalated in a 3×3×1 supercell of the MoS_2@VS_2 nanocomposite at the interface site below V (V_i), interface site below Mo (Mo_i), surface site above V (V_{sur}), surface site above Mo (Mo_{sur}), surface site above the center of V–S Hexagon (V_H), surface site above the center of Mo–S hexagon (Mo_H), and interface site below the V–S hexagon (V_{Hi}) 90

Chapter 1

Introduction

1.1 2D materials

Many physical and chemical properties of functional materials, such as catalytic and chemical activity, electronic, magnetic, thermal, mechanical, and optical properties of the functional materials vary with changing their dimensionality. It stimulated the studies on the dimensionality control of materials for the last few years. Thus the materials miniaturization has lead the materials scientists and engineers to synthesize a suspended single-atom-thick layer of carbon, called graphene. Besides its applications in the advanced nanotechnology, this material has exposed new physical and chemical aspects of the materials, and since then, the interest in the search for other two-dimensional (2D) materials is growing day by day [1–5]. Soon after graphene was realized, *h*-BN, silicene, phosphorene, borophene, transition metal dichalcogenides (TMDs), transition metal monochalcogenides (TMMs), transition metal halides (TMXs), transition metal carbides(TMCs), and *M*Xenes have been found in free standing single layers. All these materials differ in structure, chemical and physical properties [6–12]. Furthermore, it is found that the properties of these materials as mentioned earlier can be tailored by functionalization, vacancy engineering, impurity doping, and external stimuli (such as electric and magnetic fields, temperature and pressure)[6, 13, 14]. Besides their applications in nanotechnology, these materials have opened doors to debates on new physical phenomena, such as topological insulators, massless Dirac fermions, Rashba, and quantum anomalous Hall effects[15–18]. Although these materials have shown a backbone role in the future nanotechnology, synthesis and characterization of these materials in the laboratory is costly and time-consuming, while its commercialization is challenging. From the last three decades, the tendency of researchers to use computational tools in the materials design is highly increasing. It has three primary reasons, the development of new computer codes, agreement of the simulated data with the experimental one, and availability of highspeed computers. Another advantage of the computation is its easy atomistic analysis of the materials. The computational methods have played a leading role in the three dimensional (3D) materials design in general and in the 2D materials in particular. Besides, the material characterization, the computational methods have also played a valuable role in the prediction of new 2D materials and their phase transitions under different conditions. As an example, silicene and germanene (single layers of silicon and germanium) were predicted first by using first-principles methods [19]. As contrary to other monolayers the parent materials (bulk silicon and germanium) for these monolayers were not in layered structures, experimentalist did not believe in its synthesis at that time. However, later on, they were synthesized in the laboratory which proved the significance of the computational methods in finding new 2D materials [20]. As most of the 2D materials are still far away from their synthesis in laboratories, before considering a new material for applications or properties it should first pass through stability criteria.

1.2 The least stability criteria

Nowadays it is generally well known that most of the material properties are related to the nature of its chemical bondings and geometry. For example, both the graphite and diamond are made of carbon atoms, but their chemical and physical aspects are different. Similarly, 2H MoS_2 is a direct bandgap semiconductor whereas 1T MoS_2 is metallic. Searching for new material compositions and geometries with required functionalities is of high interest to chemists and material scientists. Computational methods are more effective in atomistic materials modeling for advanced nanotechnology [21–24]. Subject to the materials quality control, contamination, different preparation methods, and isolation, properties of a 2D material can be changed. That is why before discussing some unique features of 2D materials, we briefly introduce the least stability criteria, and materials should pass through, particularly in case a material is not yet synthesized in the laboratory.

Thermodynamic stability

Let us consider the simplest binary reaction in which $n_1X_1n_2X_2$ is a product, formed by the combining reactants of species X_1 and X_2 in molar ratio $n_1 : n_2$ i.e $n_1X_1 + n_2X_2 \rightarrow n_1X_1n_2X_2 + \triangle H$ (eV). Here

$$\Delta H = \frac{E(n_1X_1n_2X_2) - E(n_1X_1) - E(n_2X_2)}{n_1 + n_2}$$

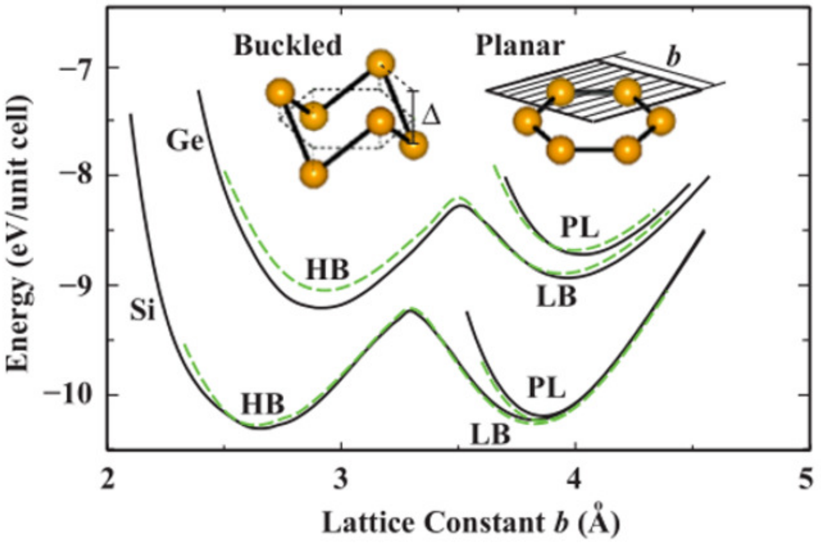

Figure 1.1: Energy against lattice constants for silicene and germanene in planer (PL), low-buckled (LB), and high buckled (HB) structures. Reproduced from reference [19].

is the heat of formation, where $E(n_1X_1n_2X_2)$, $E(n_1X_1)$, and $E(n_2X_2)$ are the total energies of the product $n_1X_1n_2X_2$ and reactants n_1X_1 and n_2X_2, respectively. $\triangle H$ generally depends upon the nature of the atomic species, combination ratios, coordinations, geometry, and stoichiometry. ΔH defines how favorable a reaction is and how strong are the resulting chemical bonds. For starting a reaction, some ignition temperature may also require. Since most of the single-layered 2D materials are still limited to computational analysis only, there can be multiple choices for combining a set of reactants to make a structure. However one with the lowest $\triangle H$ will be the most stable and thus the most favorable configuration. If a new structure is not reported in an experiment, its phase having lowest $\triangle H$ can be considered for analysis. As $\triangle H$ values may vary with changing computational methods, therefore for comparison the same method should be used for all structures under consideration. For example, there are too many pseudopotentials for each element. Using different pseudopotentials may result in different energies. Also, some methods are best suited for particular elements as for examples the GGA+U method is to be used for the strongly correlated materials rather than GGA method. A proposed composition can be relaxed in different geometries, each results in different energy, even if the symmetry breaking is allowed. It is because it can have multiple local and a single global minimum. For structure relaxation of silicene and germanene, the planer and low-buckled structures were found as local while the high-buckled structure was found as a global minimum, as shown in Fig. 1.1. Structure of the experimentally available silicene agrees well with the theoretically predicted one. Using the existing monolayers as a prototype and taking help of the periodic table, one can estimate the structure of other compounds like

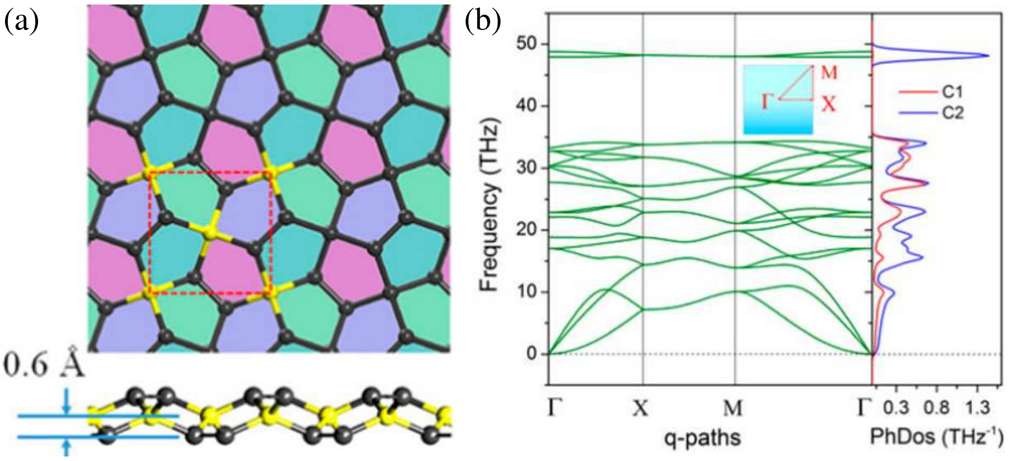

Figure 1.2: (a) Top and side views of the penta-graphene. The yellow and black colored spheres are for sp^3 and sp^2 carbon atoms respectively. (b) Phonon band structure and corresponding density of states for penta-graphene. Reproduced from reference [21].

it. We will categorise these structures in the next section.

Dynamical Stability

Although searching for a structure with lowest $\triangle H$ for a composition to be stable is necessary but not sufficient. The lattice of the crystal oscillates continuously around the equilibrium position by exchange of kinetic and potential energies. These oscillations continue even at 0K, and the related vibrational energy is called the zero point energy. The amplitude of lattice vibrations increases with the increasing temperature. Thus the phase transition with increasing temperature is obvious. However, at a given temperature (at 0K at least) a material to be stable dynamically, the atoms of the material should behave like a bound system which can be understood from its phonon dispersion. The geometry, phonon band structure, and density of states for dynamically stable pent-graphene is shown in Fig. 1.2.

Softening of a phonon branch in the Brillouin zone of a material indicates dynamical instability. It means that the square of the frequency given by the dynamical matrix is negative and generates imaginary frequency. The restoring force generated by this particular mode is therefore not enough to perform lattice vibrations which means that the system is in a transition state. Phonon spectrum of a material consists of three acoustic modes, called the longitudinal acoustic mode (*LA*), the transverse acoustic mode (*TA*), and the flexural acoustic mode (*ZA*), respectively. In bulk materials, all these three branches are linear as $q \rightarrow 0$ however in a monolayer the *ZA* branch shows quadratic nature [25]. The softness of the *ZA* branch in phonon dispersion of monolayers is natural compared to the other branches. The softness of *ZA* branch at $q \rightarrow 0$ in some of the monolayers arises due to the instability against longwavelength transversal waves. Such an instability can be removed by introducing defects [19]. Although, most often the soft modes in the phonon dispersion of a material indicate its dynamical instability, it may not be the case in general. In some rare cases, the softness of the *ZA* mode at a point away from the Γ-point is attributed to the charge density wave instability, which can be removed by increasing the electronic smearing [26]. A detailed theory of the relation between phonon modes and dynamic stability of crystalline materials can be found in ref [27]. A code called phonophy is developed by Togo *et al.* used by researchers to find the materials properties related to lattice dynamics.

Mechanical stability

A new structure with suspended single layer should fulfill the mechanical stability criteria to sustain its unstrained structure. Born stability criteria for high symmetry crystalline structures was published in 1954, and since then it has been used by many researchers. However, this criteria is not enough to put a critical condition on complex symmetries. Later on, it has been generalized for other structures as well.

The second order elastic constant C_{ij} of a crystalline lattice with equilibrium volume V_0 and energy E is given by

$$C_{ij} = \frac{\partial^2 E}{V_0 \partial \varepsilon_i \partial \varepsilon_j}$$

where $\varepsilon_{i,j}$ denotes the strain. It is a 6×6 elastic matrix with 15 dependent and 21 independent elements. Producing a virtual displacement by a homogenous infinitesimal strain in a crystal, its energy will change as:

$$E = E_0 + \frac{V_0}{2} \sum_{i,j=1}^{6} C_{ij} \varepsilon_i \varepsilon_j + O(\varepsilon^3)$$

. If for all $\varepsilon \neq 0$ $E > 0$ then the crystal will be mechanically stable. The Born has derived four necessary and sufficient conditions for stability of a crystalline structure regardless of its symmetry. As discussed in ref. [28], some necessary but not sufficient conditions in terms of elastic coefficients can be derived from the Born stability criteria:

$$C_{ii} > 0, C_{ij}^2 < C_{ii} C_{ij}, \forall_{i,j}$$

We summarize the necessary and sufficient stability conditions for some of the crystal systems from ref. [28].

Cubic systems:

$$C_{11} - C_{12} > 0, C_{11} + 2C_{12} > 0, C_{44} > 0$$

Hexagonal and tetragonal systems:

$$C_{11} > C_{12}, 2C_{13}^2 < C_{33}(C_{11}+C_{12}), C_{44} > 0, 2C_{16}^2 < C_{66}(C_{11}-C_{12})$$

Rhombohedral systems:

$$C_{11} > |C_{12}|, C_{44} > 0, C_{13}^2 < \frac{1}{2}C_{33}(C_{11}+C_{12}), C_{12}^2 + C_{15}^2 < \frac{1}{2}C_{44}(C_{11}-C_{12}) \equiv C_{44}C_{66}$$

Orthorhombic systems:

$$C_{ii} > 0, C_{ii} + C_{jj} - 2C_{ij} > 0, C_{11} + C_{22} + C_{33} + 2(C_{12} + C_{13} + C_{23}) > 0.$$

Because 3D periodic boundary conditions are used in DFT calculations, the elastic constants C_{ij}^{2D} are to be renormalized with respect to the distance c between the periodic layers [29], that is

$$C_{ij}^{2D} = cC_{ij}^{3D}$$

Since some of the C_{ij} are meaningless, the Born stability criteria become more straightforward in the case of 2D materials.

1.2.1 Environmental Stability

Although conditions discussed in section 2.0 are necessary and sufficient to say a material is stable but they may or may not be stable on ambient conditions. This instability will inevitably lead to a new structure, and therefore its band structure and other physical and chemical properties will change. For example, phosphorene has a direct band gap and high carriers mobility, computational studies show degradation of its properties when exposed to air [30, 31]. Chemical stability of materials against oxygen, nitrogen, and water can be estimated from their adsorption energies on the proposed structure. Similarly, the thermal stability of a material can be checked by using *ab initio* molecular dynamics.

1.3 Classification of monolayers

Classification of materials based on structure or properties makes it easy to start research with a material of your interest. We therefore, classify the computationally known single layer materials firstly based on their structure and then their functionalities.

1.3.1 Structure-Based Classification

Most of the know single layer materials occur in hexagonal geometry whereas a few in orthorhombic geometries as well.

Elemental Monolayers

The history of monolayers starts from elemental monolayer, the graphene. Although after graphene much of the attention on searching single layer materials was given to TMDs, TMMs, and other layered materials, nowadays there are various elemental monolayers, each having its importance. Up to now graphene (C), silicene (Si), germanene (Ge), stanene (Sn), phosphorene (P), arsenene (As), antimonene (Sb), Bi monolayer, and borophene are computationally known monolayers. While graphene, silicene, germanene, stanene, phosphorene, and borophene have been synthesized and characterized in the laboratory as well [15, 20, 30, 32–34]. The parent material for graphene (graphite) and phosphorene are the only elemental layered materials.

Graphene has a flat hexagonal structure while silicene, germanene, stanene, arsenene, antimonene, and Bi have buckled hexagonal structures. Phosphorene has two polymorphs, known as the black phosphorene and the blue phosphorene. The black phosphorene has orthorhombic geometry whereas the blue phosphorene has a buckled hexagonal geometry. Borophene has been found to have many allotropes. Graphene is found to be dynamically stable in the low buckled pentagonal rings of mixed sp^2 and sp^3 bonded carbons atoms called the pentagraphene, but its energy is too higher than that of flat hexagonal graphene. Other structures for graphene have also been designed but none of those is synthesized. Structures of graphene, silicene, phosphorene, and borophene are shown in Fig. 1.3.

Binary Monolayers

Monolayers consisting of two type atoms in 1:1 are called binary monolayers. The $h-$BN monolayer is a prototype binary monolayer, realized soon after the graphene synthesis [15]. In 2009 Sahin *et al.* proposed nineteen binary monolayers including PB, AlN, GaN, and SiC, with flat or low buckled hexagonal geometries. Similarly, the SnX and GeX (X = S, Se) monolayers have orthorhombic structures [35]. These monolayers are also called the TMMs. Group-III monochalcogenide MX (with M = In and Ga, X = S, Se, and Te) monolayers have four sublayers with a stacking sequence $X-M-M-X$ as can be seen in Fig. 1.3 [36, 37]. Similarly, SnO, PbS, and PbSe monolayers have cubic structures [38, 39].

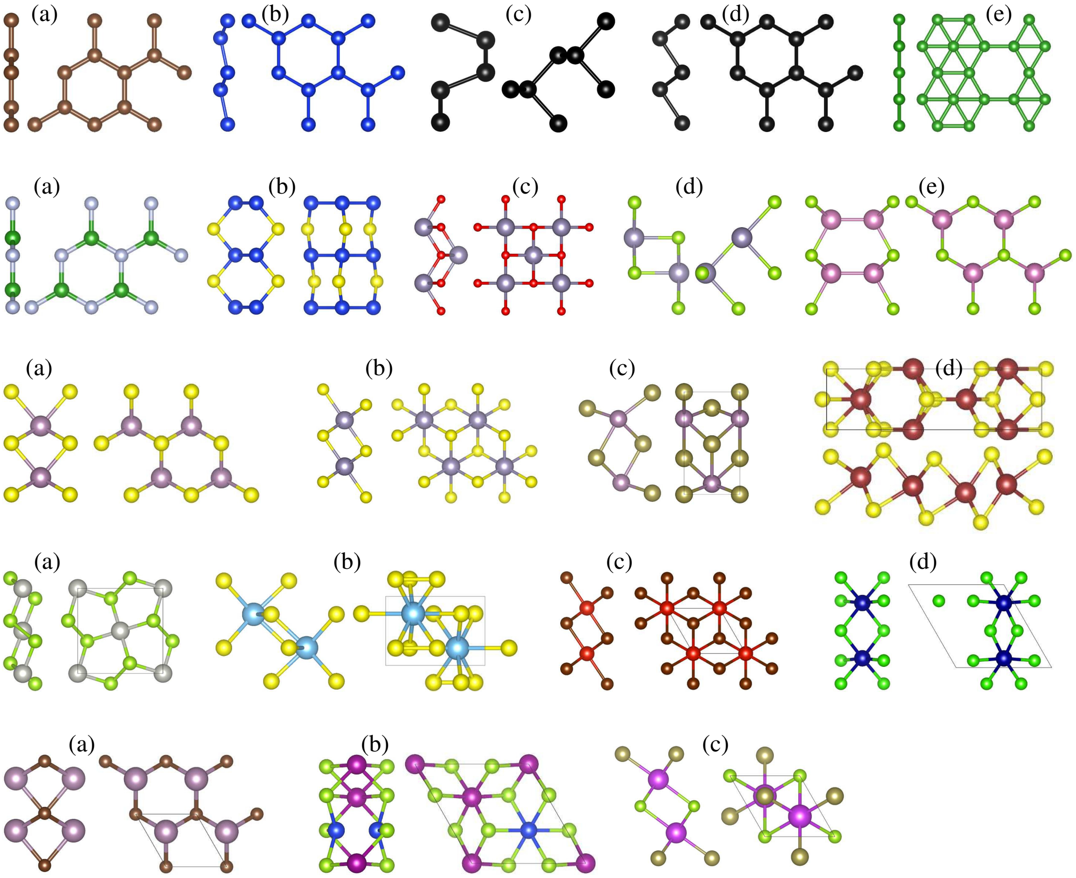

Figure 1.3: Prototype structures for two-dimensional materials. Row 1 shows side and top views for (a) graphene, (b) silicene, (c) black phosphorene, (d) blue phosphorene (e) β borophene. Row 2 shows side and top views for monolayer (a) h−BN, (b) SiS, (c) SnO, (d) SnSe, (e) InSe. Row 3 shows side and top views of monolayer (a) 2H MoS_2, (b) 1T SnS_2, (c) 1T$'$ $MoTe_2$, (d) 1T$''$ WS_2. Row 4 shows side and top views of monolayer (a) $PdSe_2$, (b) TiS_3, (c) VBr_2, $CrCl_3$. Row 5 shows the side and top views of monolayer (a) Mo_2C, (b) $MnSiCl_3$, and (c) Bi_2Te_2Se.

Transition Metal Dichalcogenides

TMDs (MX_2, where M is a transition metal and X= S, Se, Te) monolayers is one of the largest family of single-layered materials. Because of its easy synthesis, high environmental stability, and interesting electronic and optical properties, they have shown high promise in nanotechnology. So far there have been five different structures predicted for TMD chalcogenides [40–46]. However, in each case, a transition metal atomic layer is sandwiched between two layers of a chalcogen family. In case the chalcogen layers are different, they are called the Janus monolayers. Most of the TMDs are found to be stable in the 1T or 2H hexagonal structures. In both 1T and 2H monolayers, a triangular transition metal plane is sandwiched between two triangular chalcogen planes with ABC stacking for a 1T and ABA stacking for a 2H phase. For example monolayer MoS_2, $MoSe_2$, WS_2, WSe_2, and VX_2 prefers the 2H phase whereas monolayers SnX_2, TiX_2, and ZrX_2 prefer the 1T phase. Fig. 1.3 row 3(a), (b), (c), and (d) depicts the 2H, 1T, 1T′, and 1T″ phases, respectively. Monolayer MoS_2 has also been prepared in 1T phase. Monolayer $MoTe_2$ is found in 1T′ phase whereas the 1T″ phase is still only theoretical. Monolayer $PdSe_2$ is found in pentagonal geometry as shown in row 4(a) of Fig. 1.3 [23, 47]. However, this phase is very rare for TMD monolayers. Some of the monolayer TMDs are found in multiple phases, depending on the synthetic techniques .

*MX*enes

*MX*enes is a new family of two-dimensional materials. *MX*enes consists of transition metal carbides and carbonitrides (M= Transition metal, X=C/N) [7, 46, 48, 49]. They are either metallic or superconductors. Monolayers Ti_2C, Mo_2C, W_2C, Sc_2C, Mo_2C, Ti_3C_2, are few of the examples. Their electronic and chemical properties can be easily tailored by functionalization with F, Cl, H, and OH functional groups [48, 50–56]. Side and top view of monolayer Mo_2C are shown in row 5(a) of Fig. 1.3.

Transition Metal Halides

Monolayer transition metal halides consist of an atom from the transition metals and two or three atoms from halogens. The first one is called transition metal dihalide whereas the last one is called transition metal trihalide. Both these types have a hexagonal geometry. Top and side views of the monolayer BiI_2 and $CrCl_3$ are shown in row 4(c, d) of Fig.1.3, respectively. A detailed review paper on transition metal di and trihalides is published recently [11].

Besides these, there are many other two dimensional structures like $MnSiCl_3$, $CrSiCl_3$, Bi_2Te_2Se, Bi_2Se_3 (top and side views are shown in row 5(b, c) of Fig. 1.3 respectively.) and many others. Two many derivatives have been found. Vacancy formation, substitution, and functionalization have increased their number even more. These materials have shown a magnetic moment and interesting electronic structures.

1.3.2 Properties Based Classification

Up to now, we have discussed different stability conditions and 2D structural prototypes to help the readers in finding new stable 2D materials. Now we are going to classify these materials based on their physical and chemical properties to make the research in the field of 2D materials easier.

Metals

Metals are an important part of the electronic circuits in nanotechnology. Graphene, silicene, borophene, MXenes, few of the TMDs are metallic. In TMDs monolayers the TiX_2, VX_2, CrX_2, and NbX_2 (X = S, Se, or Te) are metallic. 1T and 1T$'$ phase of the MoX_2 and WX_2 are also metallic. The borophene, Mo_2C, and some other monolayers are proved to be superconductors.

Semiconductors

Most of the TMDs monolayers, like 2H MoX_2, WX_2, ZrX_2, HfX_2 and SnX_2, etc are semiconductors. The $h-$BN and SnO monolayers are large bandgap insulators whereas the GaN, AlN, BP, SnX, GeX, InX, and GaX monolayers are semiconductors. The band structures of monolayer SnO, GaX, and InX are found to have Mexican hate like dispersion, and thus they can be multiferroic by electron or hole doping.

Magnetic

Most of the transition metal dihalide and transition metal trihalide monolayers are magnetic. In TMD monolayers the VX_2 and CrX_2 families are ferromagnetic. The CrSiX_3 and $MnSiCl_3$ (with X= Cl, Br, I) are also magnetic.

Ferroelectrics and Piezoelectrics

Ferroelectric polarization in the ultra-low thin films of the ferroelectric materials reduces with decreasing thickness, but still, some 2D ferroelectrics are engineered. In-plane piezoelectricity in these materials can be produced by applying a uniaxial strain to destroy the mirror symmetry. Such materials are useful in designing memory storage and sensing devices. Chandrasekaran *et al.* [57] proposed a functionalized MXene monolayer (Sc_2CO_2)

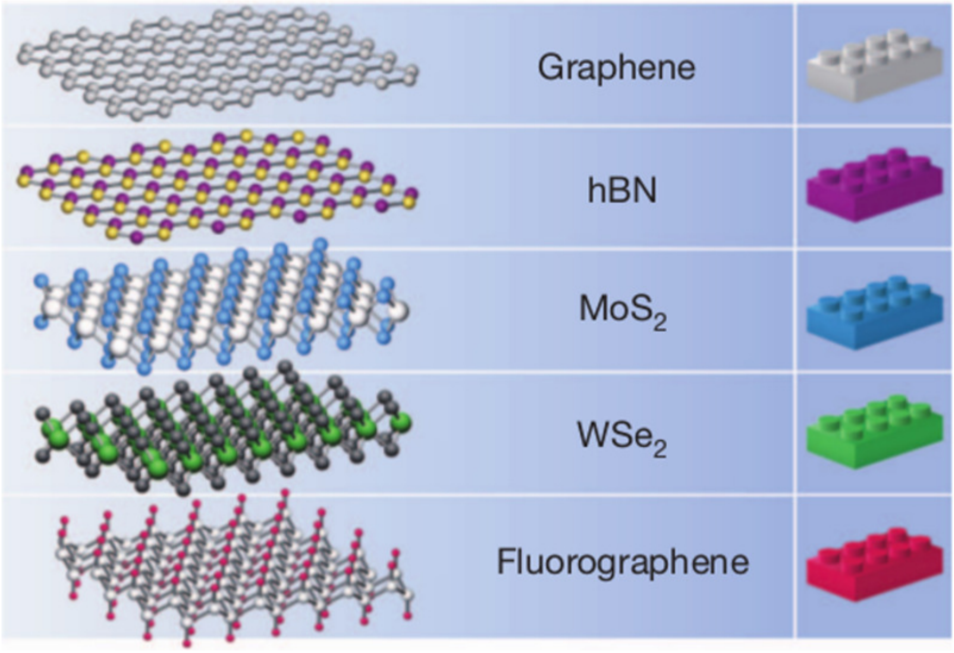

Figure 1.4: Construction of a heterostructure of different layered materials. Reproduced from reference [64]

with high switchable out-of-plane polarization. Similarly, the metal adsorbed graphene and Janus monolayers have also shown a high spontaneous out-of-plane polarization and piezoelectricity [58, 59]. Monolayer TMDs, SnS, SnSe, GaS, GaSe, InS, IndSe, and some of the Janus monolayers are found to have significan in-plane piezoelectric coefficients [60–63].

1.4 Van der Waals heterostructures

A single 2D material may not be enough to make a nanodevice, therefore combining these materials to manufacture a nanodevice or enhance its efficiency has received considerable interest in the last few years [64, 65]. Two different kinds of heterostructures for 2D materials are possible, the leteral heterostructure and the vertical heterostructure. Since the van der Waals materials have intralayer strong covalent bonds and a weak interlayer bonds, they can be easily isolated and combined in vertical heterostructures. Fig. 1.4 shows how easily the van der Waals materials can be combined in heterostructures. If two unit cells of different materials with high lattice mismatch are combined in a heterostructure, it will induce strain and properties of the unstrained heterostructure may not be found. A lattice mismatch of less than 3% is however acceptable.

1.5 Motivation

Computational methods have a valuable role in the exploration of new two-dimensional materials. The new materials are passed first through some optimization procedure to know about its stability and then considered for further characterization. In my thesis I have studied monolayer TiS_2 as anode material for Li, Na, K, Be, Mg, Ca, and Al ion batteries. The TiS_2 monolayer is found to be stable in a 1T hexagonal structure. It has a high capacity of all the considered ions except Be and Al. The ion diffusion barrier and electronic properties of TiS_2 monolayer recommend it as all times anode material. A reducing diffusion barrier with increasing ionic size is noticed both for monovalent and divalent ions. Next, I have studied a new *MX*ene monolayer named W_2C. This monolayer fulfills all the stability conditions, and its mechanical strength is found to be the highest after the graphene in 2D materials. This new material is metallic and has a high Li/Na capacity. The most promising property of this material is that that it has only a few meV diffusion barrier for Li/Na diffusion which provides ultra-fast conducting paths for the Li/Na diffusion. This unique property of monolayer W_2C makes it a high power rate anode material. There are few conflicting theoretical reports on the possible structure of crystalline unzipped graphene oxide (UGO) monolayer. By considering, all possible dipolar structures of UGO to find its stability in energy and lattice dynamics, we found that UGO monolayer has a zigzag antiferroelectric structure. Furthermore, the oxygen atom in the UGO monolayer produces electron excess anddeficient regions where the Li ions can be trapped in the electron deficient regions. Also, the band structure of UGO has a Dirac cone with a small bandgap opening which is a symbol of interesting transport properties. We found that monolayers of the MoC, WC, WS, and WSe are stable in the buckled hexagonal structure. Due to the lack of inversion symmetry, these materials have large out-of-plane polarization. In-plane polarization in these materials is seen to induce due to the homogenous uniaxial strain.

In the second part of my thesis, I have studied the stability and functionality enhancement by heterostructuring. SnS_2 monolayer has a high Na storage capacity of 550 mAh/g but shows a large expansion on the Na intercalation. Furthermore, it has a high bandgap which can degrade its electronic properties as an anode. We grow the SnS_2 monolayer on graphene as a substrate which overcomes these deficiencies. The graphene layer strengthens the SnS_2 sheet mechanically and provides paths for the electronic conduction. On the other hand, the addition of the SnS_2 layer to graphene activates it for Na adsorption. Similarly, the MoS_2@VS_2nanocomposite is also studied. The monolayer VS_2 has not been synthesized yet because it is chemically very active. However, the Li/Na adsorption energies on monolayer VS_2 and its metallic nature makes it a promising anode material if its synthesis is made possible. On the other hand monolayer $MoS_2$is a stable material but has a high band gap and its

Li/Na adsorption energy is not enough to have an appreciable capacity. Both these monolayers preferred the 2H hexagonal structures and have negligible lattice mismatch. We, therefore, grow the monolayer VS_2 on monolayer MoS_2 which stabilizes the VS_2 layer and activates the MoS_2 layer for Li/Na adsorption. The system as a whole becomes conducting which makes the MoS_2@VS_2 nanocomposite promising anode materials for Li/Na ion batteries.

Chapter 2

First-principles Tools

2.1 The Schrödinger Equation

In general, the quantum state of a system, consisting of N number of electrons and M number ions can be adequately described by a wave function $\psi(r_i,\, \mathrm{R}_A)$, with r_i and R_A representing the electronic and ionic position vectors, respectively. A nonrelativistic and time-independent Schrödinger wave equation for such a system can be written as:

$$\hat{H}\psi = E\psi$$

where $\hat{H}$ represents the Hamiltonian operator and E its eigenvalue. $\hat{H}$ can be decomposed as:

$$\hat{H} = \hat{T}_{\mathrm{e}} + \hat{T}_{\mathrm{A}} + \hat{V}_{\mathrm{Ae}} + \hat{V}_{\mathrm{ee}} + \hat{V}_{AA}$$

Here $\hat{T}$ is for the kinetic and $\hat{V}$ for the potential energy of N electrons and M ions. All these terms are defined as below:

$$\begin{aligned}
\hat{T}_{\mathrm{e}} &= -\frac{\hbar^2}{2m_{\mathrm{e}}} \sum_{i=1}^{N} \nabla_i^2 \\
\hat{T}_{\mathrm{A}} &= -\frac{\hbar^2}{2} \sum_{A=1}^{M} \frac{\nabla_A^2}{M_A} \\
\hat{V}_{\mathrm{Ae}} &= -\frac{1}{4\pi\varepsilon_0} \sum_{i=1}^{N} \sum_{A=1}^{M} \frac{Z_A e^2}{|\mathrm{r}_i - \mathrm{R}_A|} \\
\hat{V}_{\mathrm{ee}} &= \frac{1}{4\pi\varepsilon_0} \sum_{i=1}^{N} \sum_{j>1}^{N} \frac{e^2}{|\mathrm{r}_i - \mathrm{r}_j|} \\
\hat{V}_{\mathrm{AA}} &= \frac{1}{4\pi\varepsilon_0} \sum_{j=1}^{M} \sum_{B>A}^{M} \frac{Z_A Z_B e^2}{|\mathrm{R}_A - \mathrm{R}_B|}
\end{aligned}$$

The Schrödinger wave equation for this system therefore becomes:

$$[-\frac{\hbar^2}{2m_\mathrm{e}}\sum_{i=1}^{N}\nabla_i^2-\frac{\hbar^2}{2}\sum_{A=1}^{M}\frac{\nabla_A^2}{M_A}-\frac{1}{4\pi\varepsilon_0}\sum_{i=1}^{N}\sum_{A=1}^{M}\frac{Z_Ae^2}{|\mathrm{r}_i-\mathrm{R}_A|}+\frac{1}{4\pi\varepsilon_0}\sum_{i=1}^{N}\sum_{j>1}^{N}\frac{e^2}{|\mathrm{r}_i-\mathrm{r}_j|}]$$

ψ=$E\psi$

Solution to this equation is complicated without making some suitable approximations. An approximation to this equation was firstly made by **Born-Oppenheimer** [66]. Since the mass of an ion is too larger compared to the mass of the electrons that the kinetic energy of the ions can be neglected. To overcome the difficulties in solving the dynamics of the electrons in a frozen nuclei layout, the kinetic energy of the electrons and ions is dissociated. That is:

$$\psi(r_i,R_A)=\psi(r_i)\psi(R_A)$$

$$\hat{H}_e\psi(r_i)=E_e\psi(r_i)$$

where

$$\hat{H}_e=[-\frac{\hbar^2}{2m_\mathrm{e}}\sum_{i=1}^{N}\nabla_i^2-\frac{1}{4\pi\varepsilon_0}\sum_{i=1}^{N}\sum_{A=1}^{M}\frac{Z_Ae^2}{|\mathrm{r}_i-\mathrm{R}_A|}+\frac{1}{4\pi\varepsilon_0}\sum_{i=1}^{N}\sum_{j>1}^{N}\frac{e^2}{|\mathrm{r}_i-\mathrm{r}_j|}+\frac{1}{4\pi\varepsilon_0}\sum_{j=1}^{N}\sum_{B>A}^{N}\frac{Z_AZ_Be^2}{|\mathrm{R}_A-\mathrm{R}_B|}]$$

But the above Hamiltonian is still challenging enough that further simplifications are essential to make it handy. The **Slater Determinant** for electrons in a system is found which fulfills the anti-symmetric property and Pauli exclusion principles. The probability of finding an electron within a given point of space $d\vec{x}_1d\vec{x}_2d\vec{x}_3.....d\vec{x}_N$ is

$$|\psi(\vec{x}_1,\vec{x}_2,\vec{x}_3,....\vec{x}_N)|^2d\vec{x}_1d\vec{x}_2d\vec{x}_3.....d\vec{x}_N$$

Being identical particles, the exchange of two electrons can only change the sign of wave function.

That is:

$$\psi(\vec{x}_1\vec{x}_2.....\vec{x}_N)=-\psi(\vec{x}_2,\vec{x}_1,.....\vec{x}_N)$$

But the probability of finding an electron in space $d\vec{x}_1d\vec{x}_2d\vec{x}_3.....d\vec{x}_N$ does not change.

That is:

$$|\psi(\vec{x}_1\vec{x}_2.....\vec{x}_N)|^2=|\psi(\vec{x}_2,\vec{x}_1,.....\vec{x}_N)|^2$$

Let $\chi_i(x_i)$ be representing a set of wave functions (spin orbitals) for a group of electrons.

Then the N-electrons system can be illustrated by an anti-symmetrized product, written as:

$$\phi_{SD} = \frac{1}{\sqrt{N!}} = \begin{vmatrix} \chi_1(x_1) & \chi_2(x_1) & .... & \chi_N(x_1) \\ \chi_1(x_2) & \chi_2(x_2) & .... & \chi_N(x_2) \\ : & : & : & : \\ \chi_1(x_N) & \chi_2(x_N) & .... & \chi_N(x_N) \end{vmatrix}$$

2.2 The Hartree-Fock method

Handling a many-body wave function to calculate the energy of the system is a too tough. For such a case, the Hartree-Fock method is found to simplify the calculation by calculating the energy of each electron in the averaged static field. The Hartree-Fock Hamiltonian is written as:

$$f_i = -\frac{1}{2}\nabla_i^2 - \sum_k^{core} \frac{Z_k}{r_{ik}} + V_i^{HF}$$

where V_i^{HF} is the Hartree-Fock potential which is the average repulsive potential of an electron to the rest N-1 electrons. It can be written as:

$$V_i^{HF}(\vec{x}_1) = \sum_i^N \hat{J}_i(\vec{x}_1) - \hat{K}_i(\vec{x}_1)$$

where $\vec{x}_1$ stands for the position of one electron, $\hat{J}_i$ for the Coulomb operator, and $\hat{K}_i$ for the exchange contribution to the Hartree-Fock potential.

$\hat{J}_i$ is defined as:

$$\hat{J}_i(\vec{x}_1) = \int |\chi_i(\vec{x}_2)|^2 \frac{1}{r_{12}} d\vec{x}_2$$

and $\hat{K}_i$ operating on spin-orbital is defined as:

$$\hat{K}_j(\vec{x}_2)\chi_i(\vec{x}_1) = \int \chi_j^*(\vec{x}_2) \frac{1}{r_{12}} \chi_i(\vec{x}_2) d\vec{x}_2 \chi_i(\vec{x}_1)$$

Likewise, the HF potential V_i^{HF} is non-local which relies on the initially unknown spin-orbitals χ_i. To compute V_i^{HF}, the Hartree-Fock Self-Consistent Field (HF-SCF) process is employed. An initial set of spin orbitals χ_i is estimated and used to make a new V_i^{HF}. With the HF potential then new spin-orbitals are calculated. The process continues until the result reaches the convergence criteria. Since the HF method neglects the dynamic correlation between the electronic movements, the HF energy is above the total energy.

2.3 The Density Functional Theory

Density Functional Theory (DFT) uses the total density of electrons as a fundamental tool rather than the N-body wave functions for the electrons. The electron density is a physical characteristic. It is easier to calculate the electron density with increasing number of electrons. Furthermore, this scheme overcomes the major weakness of the Hartree-Fock scheme, which neglects the electron correlation. Hence, the DFT makes the calculation more precise, whereas the exchange part is precisely defined in the HF scheme.

Hohenberg and Kohn [67] presented the first basic theorem of DFT with the principal idea "the external potential $V_{ext}(\vec{r})$ (the external potential applied by the nuclei) is the unique functional of the electronic density $\rho(\vec{r})$".

The second fundamental DFT theorem of Hohenberg Kohn is "the functional $F_{HK}[\rho]$ that yields the ground state energy of a system, yields the lowest energy if and only if the input density is the real ground state density".

2.4 The Kohn-Sham Formulation

Kohn and Sham [68] introduced a new technique for solving the Schrödinger equation. The interactive system was replaced by anon-interactive one with the assumption that all the electronic ground-states are identical. All contributions in the total energy can be determined from the density $\rho(r)$. Energy of the system is the lowest only when the density is at its original state $\rho(r) = \rho_o(r)$, which means that the system is in its ground state. The total energy ($E[\rho]$) of the electron cloud is written as:

$$E[\rho] = T[\rho] + V_{ee}[\rho] + E_{xc}[\rho] + \int V_{ext}(r)\rho(r)d^3r$$

where $T[\rho]$ is the kinetic energy term for the non-interacting electrons, $V_{ee}[\rho]$ is the Coulombic electron-electron interaction term, $E_{xc}[\rho]$ is the exchange-correlation term, and $\int V_{ext}(r)\rho(r)d^3r$ is the interaction of the electrons with the potential due to nuclei.

So far, the DFT theory is exact since it doesn't contain any approximation. $E_{xc}[\rho]$ is the only unknown term where approximations are necessary. We discuss several approximations in the following section.

2.5 Approximations used in Exchange-Correlation Functional

Several methods have been proposed to compute the $E_{xc}[\rho]$ term, e.g., the Local Density and the Generalized Gradient Approximations (LDA and GGA).

2.5.1 Local Density Approximation (LDA)

Let us consider the electrons in a system as a uniform gas, the assumption of the LDA approximation then says that the charge density changes slowly on the atomic level, so that the heterogeneous electronic systems can be taken as locally homogeneous. The exchange-correlation energy for an unpolarized-spin system is written as:

$$E_{xc}^{LDA}[\rho] = \int \rho(r)\varepsilon_{xc}(\rho)dr$$

As an example, the LDA functional formed by Vosko, Wilk, and Nusair is the Monte Carlo computation for a homogeneous electron gas. The exchange-correlation energy for the spin-polarized system in the local spin-density approximation (LSDA) is to be written as:

$$E_{xc}^{LSDA}[\rho_\alpha, \rho_\beta] = \int dr\rho(r)\varepsilon_{xc}(\rho_\alpha, \rho_\beta)$$

where ρ_α and ρ_β represent the electronic spin density.

This scheme yields a reasonable accuracy for molecular properties calculations. For example, structures, charge moments, and vibrational frequencies, etc. But in case of rapidly changing density, it leads to poor results for the energetics of the system, such as energy barriers, and bond energies.

2.5.2 Generalized Gradient Approximation (GGA)

To solve the previous issue, the Generalized Gradient Approximation (GGA) was suggested. It upgrades the LDA scheme by considering the system as an inhomogeneous gas of electrons and taking in to account the effects of non-local electrons in the functional. The exchange-correlation term is a function of ρ and $\nabla\rho$:

$$E_{xc}^{GGA}[\rho] = \int \varepsilon_{xc}(r)[\rho(r), \vec{\nabla}\rho(r)]d^3r$$

The GGA group, which include PBE, PAW91, and BLYP, etc [69, 70]. can be produced by applying various approximations for the equation given above. Since GGA allows more generous fluctuations than the LDA, the GGA usually yields a more accurate result than the

LDA. For example, in the case of total energies, energy barriers, atomization energies, and differences in structural energy. The PBE functional (an exchange-correlation functional made by Perdew, Burke, and Ernzerhof) is an upgraded gradient-corrected GGA functional. This functional has an easy derivation where all the parameters are basic constants. This functional is the most frequently used, both for molecules and solids.

2.5.3 The Hybrid Functionals

The exchange terms of the previously proposed functionals are crudely illustrated due to the electrons self-interaction issue, while the exchange part in the HF method is precisely defined. But a direct combination of the DFT correlation part and HF exchange part provides poor results. The hybrid functionals, which are a combination of HF and DFT, regroups the exchange and correlation terms of both methods, can avoid this issue. As an example, the B3LYP [71] is the most frequently used hybrid functional. It is written as:

$$E_{xc}^{B3LYP} = E_X^{LDA} + a_0(E_X^{HF} - E_X^{LDA}) + a_X(E_X^{GGA} - E_X^{LDA}) + E_C^{LDA} + a_C(E_C^{GGA} - E_C^{LDA})$$

where E_X^{GGA} and E_C^{GGA} are the GGA exchange and correlation functionals, E_C^{LDA} is the LDA to the correlation functional, with $a_0 = 0.20$, $a_X = 0.72$, and $a_C = 0.81$.

2.6 Blöch states

The periodic boundary conditions can be used to model a system can be by repeating a unit-cell in all three dimensions of space. The model is considered to be stable if the total energy and the force on the system converge. Here the electron density is described by a plane wave basis set. The Bloch's theorem is written as:

$$\psi_{\vec{k}}(\vec{R} + \vec{T}) = e^{i\vec{k}\vec{T}} \psi_{\vec{k}}(\vec{R})$$

where $\psi_{\vec{k}}(\vec{R})$ represents the electronic wave function,$\vec{R}$ represents the position vector in a direct space, $\vec{T}$ represents the position vector in a reciprocal space,and $\vec{k}$ represents a set quantum number k_x, k_y, k_z.

In case of a finite solid, the quantum numbers are necessarily continuous. But a cut-off energy is employed to confine the set to a sphere in the reciprocal space in use:

$$E_{cutoff} > \frac{\hbar^2 \left|k + T\right|^2}{2m}$$

where m represents the mass of an electron.

Now, to have a excellent result for a likely calculation cost, the selected cut-off energy should be neither too high nor too low. The Bloch's functions are defined usually over an infinite number of $\vec{k}$ points in the Brillouin zone. The equation for Bloch function $\psi_{i,R}$ is necessary to be solved for each $\vec{k}$ point. The total energy of the system can be found by integrating the band energy of each $\vec{k}$ point:

$$E = \sum_i \frac{1}{\Omega_{BZ}} \int E_{i,k} g_i(\vec{k}) d\vec{k}$$

where Ω_{BZ} is the Brillouin zone volume, and $g_i(\vec{k})$ is the electron occupation of the ith state and point $\vec{k}$. This equation can be brought to a discrete one as:

$$E = \sum_i \sum_{\vec{k}} \omega_{\vec{k}} E_{i,\vec{k}} g_i(\vec{k})$$

here $\omega_{\vec{k}}$ is a factor which corresponds to each $\vec{k}$ point.

2.7 Pseudopotentials and Projector augmented waves (PAW)

The single-electron wavefunctions for the valence states of atoms have too many oscillations to fulfill the orthogonality condition for the core states. These oscillations are restricted to the core part which is not critical for the interaction between atoms and needs a lot of plane waves for an actual description. Therefore it will become handy if these oscillations are removed. Various tactics have been used to deal with this, two of the frequently used are discussed in the following.

2.7.1 Pseudopotentials

The most often used in my work is that of pseudopotentials, composed of two steps. In the first step, the core electrons are eliminated while in the second step wavefunctions of the valence electrons are replaced by a flat pseudo-wave-functions where few plane waves are needed for their description. The core electrons wave functions of an atom are enough compact that remains almost unaltered during the interatomic interactions. It is therfore not a close enough approximation to consider these core states as fixed and neglect them in calculations. The core electrons can be included into the potential acting on the valence electrons. The valence wave functions with different angular momentum encounter a different potential due to the orthogonality condition for the core states. E.g., consider the case of a carbon atom, where the

2s valence electrons encounter a distinct potential in comparison to the 2p valence electrons. It is because a 2s state is to be orthogonal to a 1s core state. The refined potential is consequently non-local in the angular coordinates, named as pseudopotential.

The second step in the pseudopotential scheme is the replacement of the full ionic core interaction potential with a softer pseudopotential to have smoother and node-less wave functions in the result. Additionally, the pseudopotentials can be made in such a way that their scattering properties (i.e. the phase shifts) are similar to the actual atomic potential to first order in energy. This last criterion is satisfied if the radial part of the smooth pseudo-wave-function is identical to the real wave function outside core radius r_C. Also, the pseudo-wave-function matching to its derivative at r_C is to be continuous. While the norm of the wave function inside the core region is maintained simultaneously. A true pseudopotential is made the other way around, i.e., one makes a pseudo-wave-function that satisfies these criteria and inverts the Schrödinger's wave equation to obtain the pseudopotential.

2.7.2 PAW

The projector augmented wave (PAW) method has been frequently used in my thesis. Contrary to the pseudopotential scheme, the PAW scheme has the core electrons and the full all-electron valence wave functions. The core wave functions are brought directly from all-electron calculations for the atom under consideration. The actual wave functions are replaced by smooth wave functions within some core radius r_C (similar to the pseudopotential scheme). A linear transformation operator is constructed to obtain the real wave function from the smooth one. In the PAW potentials scheme, based on a linear transformation of the pseudo wave function $\tilde{\psi}$ to the all-electron wave function ψ :

$$|\psi_n\rangle = |\tilde{\psi}_n\rangle + \sum_i |\phi_i\rangle \langle\tilde{p}_i|\tilde{\psi}_n\rangle - \sum_i |\tilde{\phi}_i\rangle \langle\tilde{p}_i|\tilde{\psi}_n\rangle$$

with $\tilde{\psi}_n$ variational quantities. The index i means a sum over the atomic site, reference energies, and the angular momentum. ϕ and $\tilde{\phi}$ are the all-electron and pseudo partial waves, matching at the core radius. Similarly, p_i represents the projector functions which are to be generated dual to the partial waves:

$$\langle\tilde{p}_i|\tilde{\psi}_j\rangle = \delta_{ij}$$

The PAW scheme implemented in VASP works directly with the all-electron valence potentials and all-electron valence wave functions.

Chapter 3

TiS_2 sheet as anode material

3.1 Introduction

The invention of rechargeable Li ion batteries (LIBs) has brought a revolution in the wireless electronic technology. It has widespread applications ranging from portable devices like smartphones and laptop computers to electric vehicles and green grids. A battery with high power density, fast recharge, and long cycle life will be a key to the development of smart electronic technology while a huge stationary battery with cheap ingredients is required for the green grids [72–75]. The electrochemical storage of energy in LIBs is one of the most efficient and applied ways for storing energy. Due to the small size and low weight of Li, LIBs have high volumetric and gravimetric capacity. On the other hand, there are some deficiencies in LIBs because of its toxic nature and limited resources of Li, and the increasing demand for batteries increases the price of scarce Li. Although the use of rechargeable LIBs in the small portable devices is satisfactory, the increase in power density and rate capability is still demanded. To boost the power density and lower the price of LIBs, Na, Mg, Ca, and Al ions are under consideration as alternatives to Li [72, 76–82].

The nontoxic, cheap, and abundant Na is the most studied alternative to Li. The intercalation of Na in the electrode materials is generally tricky compared to Li because of its larger ionic size. That is why the storage capacity of Na in the electrode materials is less than that of Li and the volume expansion due to Na intercalation is higher than that due to Li. [83–88] The partial replacement of LIBs with Na ion batteries (NIBs), especially in the stationary cells for green grids, where the weight of the battery will not be a problem, is expected in the next few years [76, 89].

Science monovalent Li, Na, and K can store a single electronic charge per metal ion, multivalent metal ions with low electronegativity and small size are of high interest for of high charge storage density. Mg, Ca, and Al has been recently studied for this purpose while Mg is the most effective ion as it has high charge storage density, small ionic size, and high cell voltage [78–82].

The selection of proper electrode material is one of the basic strategies to upgrade the electrochemical performance of a rechargeable metal ion battery (MIB) [90–92]. Most of the two-dimensional layered materials are reported to have high metal ion adsorption energies and low diffusion barriers [93, 94]. Pristine graphene is not feasible for the adsorption of alkali or alkaline earth metals. However, the studies on defective graphene have shown high storage capacity for Li, Na, Mg, and Ca [80, 95]. One of the diverse applications of transition metal dichalcogenides (TMDs) is its use as the electrode material for MIBs in bulk, a-few-layer, and monolayer phases [96]. Among the two-dimensional materials, MoS_2 and defective graphene are the most studied electrodes [80, 90, 95, 97]. However, these materials are insulating [98], whereas electronically conducting electrodes are required in batteries.

Monolayer TiS_2, one of the most important two-dimensional TMDs, has been successfully synthesized by the electrochemical lithium interaction and exfoliation method [99]. We select the 1T structured monolayer TiS_2 as a common anode material for all possible MIBs because of its low electronic band gap and metal adsorption capability. Due to its structural symmetry it can provide multi-directional easy paths for the diffusion of metal ions. The work here aims to compare the electrochemical performance of all possible MIBs with that of the Li and search out suitable alternatives to the toxic and costly LIBs. Divalent Mg and Ca are expected to have higher charge storage density than Li, which will be applicable in boosting the power density for smart portable devices. As a high net cell voltage requires as low as possible open circuit voltage from the anode material, we also compare the voltage profile of all these ions. The rate capability is another important issue which will be discussed here. Finally, the suitable alternatives for LIBs will be pointed out, keeping in mind the requirements of a device.

3.2 Computational details

All calculations were performed using the density functional theory as implemented in the Vienna Ab-initio Simulation Package [100]. The electron–electron exchange-correlation was processed using the generalized gradient approximation (GGA) with the Perdew–Burke–Ernzerhof parameterization scheme [70]. The projector augmented wave (PAW) method was used to describe the electron–ion interactions [69, 101]. The density of states calculations were performed with the HSE06 method as well [102]. The cutoff energy of 350 eV was chosen for the plane-wave expansion of the electronic eigenfunctions of monolayer TiS_2. The force criterion for the structure relaxation was chosen as 0.001 eV Å. A spacing of 25 Å between periodic images normal to TiS_2 layers was used to avoid the interlayer coupling. The Γ-point sampling

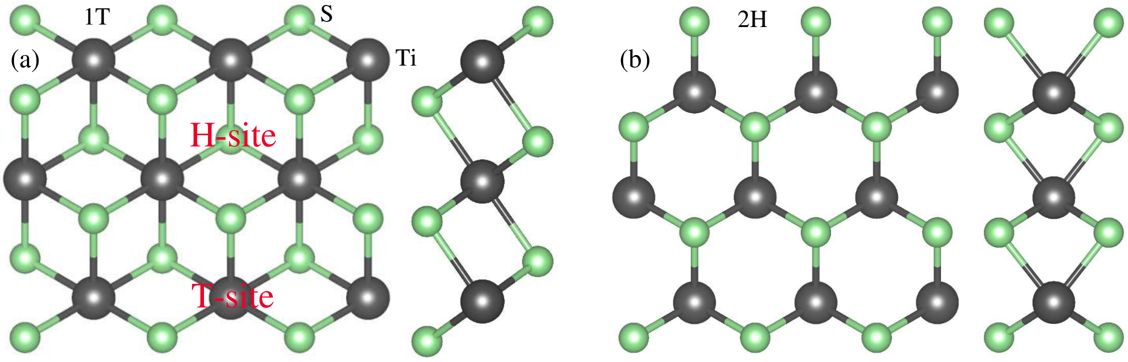

Figure 3.1: Top and side views of the monolayer TiS_2 (a) in 1T and (b) 2H phases. The black and light green colored spheres represent Ti and S atoms, respectively.

was used with a $7 \times 7 \times 1$ k-point mesh for the integration of the Brillouin zone. A $3 \times 3 \times 1$ supercell of monolayer TiS_2 (containing nine Ti and eighteen S atoms) was considered for the adsorption and diffusion of metal ions. The nudged elastic band (NEB) [103] method was used to optimize the minimum energy path along the saddle points for the diffusion of metal ions on the surface of monolayer TiS_2. The Bader charge integration [104] was used to find out the amount of charge transferred by the adsorbed metal ions.

3.3 Results and discussion

3.3.1 Structure and adsorption sites

TiS_2 is one of the layered TMDs. Most TMD monolayers are found either in 1T or 2H (hexagonal) structures under normal conditions of pressure and temperature. Both these structures consist of three atomic sub-planes. The subplane of transition metal atoms is sandwiched between the two sub-planes of chalcogen atoms. In the former case the sub-planes are in ABC stacking order (Fig. 3.1(a)) while in the latter case they are in ABA stacking order (Fig. 3.1(b)). Monolayer TiS_2 is energetically more stable in its 1T phase (space group p3m1) than its 2H phase, which is the reason why we select the 1T structure of monolayer TiS_2 for this study. Previous reports show that the 1T phase is the most stable phase for the family of monolayers TiX_2 (X= S, Se, Te) [105–108]. The scanning transmission electron microscope (STEM) image of the TiS_2 nanoflakes shows that its geometry is 1T [109]. The phonon calculations for TiS_2 show that bulk TiS_2 is stable but when the number of layers is less than four a soft mode is observed at the M symmetry point. The soft mode has been attributed to the charge density wave instability near to 0 K in TiS_2 thinner than four layers. The soft mode for monolayer TiS_2 disappears if the calculations are run by the LDA+U method [107].

Monolayer TiS_2 has been confirmed experimentally as well [99]. Our calculated lattice parameters for the 1T structured TiS_2 (a=b=3.40 Å) and the Ti–S bond length (2.43 Å) agree well with the literature [106]. The lattice parameters of the 2H structured monolayer TiS_2 are a=b=3.33 Å and the Ti–S bond length is 2.45 Å. The side and top views of the 1T and 2H monolayer TiS_2 are shown in Fig. 1(a),(b) respectively. 1T monolayer TiS_2 is metallic with the GGA calculations while with the hybrid functional method (HSE06) it shows a band gap of 0.62 eV. The 2H phase is a semiconductor (GGA band gap is 0.70 eV and hybrid band gap is 1.6 eV). Similar to monolayer SnS_2, the favorable adsorption sites of metal ions on the monolayer TiS_2 surface are located at the H- and T-sites. The H- and T-sites are shown in Fig. 3.1(a) and also have been broadly discussed in our work on monolayer SnS_2 as anode material for NIBs [110]. Monolayer TiS_2 has the in-plane stiffness of 74 Nm^{-1}, which shows that it is mechanically stronger than the monolayer SnS_2. It also completes the Born stability criterion [111], which confirms that the monolayer TiS_2 is mechanically stable.

3.3.2 Adsorption and specific capacity

First, the adsorption of a single metal atom on a 3×3×1 supercell of TiS_2 is examined, and then the adsorption of multiple atoms is examined as a function of increasing metal ion concentration. The total formation energy (E_f) of metal ion adsorption is defined as:

$$E_f = E(\mathrm{TiS_2}) - E(M_n\mathrm{TiS_2}) + nE_{M_{bulk}}$$

where $E(\mathrm{TiS_2})$ is the total energy of a 3×3×1 pristine TiS_2 supercell in its 1T phase, $E(M_n\mathrm{TiS_2})$ is the total energy of a 3×3×1 TiS_2 supercell with n metal ions adsorbed at the H- or T-sites, and $E(M_{bulk})$ is the total energy of bulk metal in its most stable structure. We consider the body-centered cubic structure for the alkali metals, the hexagonal close-packed structure for Be and Mg, and the face-centered cubic structure for Ca and Al. We define the adsorption energy (E_{ad}) for a single metal ion as:

$$E_{ad} = E(\mathrm{TiS_2}) - E(M_n\mathrm{TiS_2}) + nE(M)$$

is the energy of a metal ion in its gaseous state. The adsorption of a single metal ion on the H- and T-sites of the monolayer TiS_2 is summarized in Table 3.1. The E_{ad} decreases and the M–to–S distance (M–S) of the metal ion increases down the group, while Mg is an exceptional case. This brings about the weakening of metal ion interaction with the surface of TiS_2 due to the increasing ionic size. The data in Table 3.1 shows a tiny difference in the E_{ad} of a metal ion at the H- and T-sites, which is due to the existence of a similar S environment at these

Table 3.1: Formation energy, charge, and M-S bond distance of a single metal ion, when adsorbed at the H- and T-sites.

	Li	Na	K	Be	Mg	Ca	Al
$E_{f(H)}$ (eV)	1.75	1.66	2.11	0.86	0.92	2.46	0.02
$E_{f(T)}$ (eV)	1.71	1.61	2.08	0.63	0.80	2.36	-0.06
$E_{ad(H)}$ (eV)	3.35	2.74	2.66	4.56	2.42	4.31	3.19
$E_{ad(T)}$ (eV)	3.31	2.71	2.63	4.32	2.30	4.21	3.11
E_{coh} (eV)	1.60	1.10	0.55	3.70	1.50	1.85	3.52
$q_{(H)}$ (|e|)	0.87	0.85	0.88	1.58	1.57	1.45	1.37
$q_{(T)}$ (|e|)	0.87	0.85	0.88	1.56	1.55	1.44	1.13
M-$S_{(H)}$ (Å)	2.34	2.69	3.03	1.98	2.32	2.56	2.37
M-$S_{(T)}$ (Å)	2.38	2.71	3.05	2.00	2.36	2.60	2.47

adsorption sites. Due to the small difference in the E_{ad} at the H- and T-sites, one expects the minimum energy path for the diffusion of metal ions through H-T-H. The charge imbalance (q) in Table 3.1 shows that the adsorbed Alkali and Alkaline earth metals are singly and doubly charged, respectively, while the Al is not fully ionized. Therefore, monolayer TiS_2 may not be applicable as an anode material in Al ion batteries.

The data plotted in Fig. 3.2 is the total formation energy (E_f) as a function of the metal ion concentration for the most favorable distribution of metal ions over the monolayer TiS_2 by filling the top H-sites. The E_f profile shows that all the metal ions except Be and Al can occupy all the available H-sites without the formation of metallic clusters. Fig. 3.2 shows that TiS_2 can have the highest storage for Li but filling the T-sites when all the H-sites are already filled brings the metal ions so close that the Coulombic forces between the metal ions destroys the monolayer TiS_2. So filling only the H-sites is useful for safe storage. The Bader analysis shows that Ca and Mg are divalent to store two charges per ion adsorption, which makes them store twice as much as charge compared to the monovalent Li, Na, and K. This result has a good resemblance with the previous studies [80]. The maximum specific capacity of an electrode can be defined as:

$$C = \frac{nZF}{M_{\mathrm{TiS}_2}}$$

(mAh/g) where n is the number of adsorbed metal ions on a 3×3×1 supercell of TiS_2, Z is the valance of adsorbed metal ions (1 for Alkali metal ions and 2 for Alkaline earth metal ions), F (26801 mAh mol^{-1}) is the Faraday's constant, and M_{TiS_2} is the molar mass of the 3×3×1 supercell of TiS_2. If only the top and bottom H-sites of the monolayer are filled with the metal ions then without considering the atomic weight of the metal ions, the highest specific capacity for Li, Na, and K ions is 478.6 mAhg^{-1}, and 957.2 mAhg^{-1} for the Mg and Ca ions. If the T-sites are also considered together, maximum capacities of 957.2 mAhg^{-1} for alkali metal

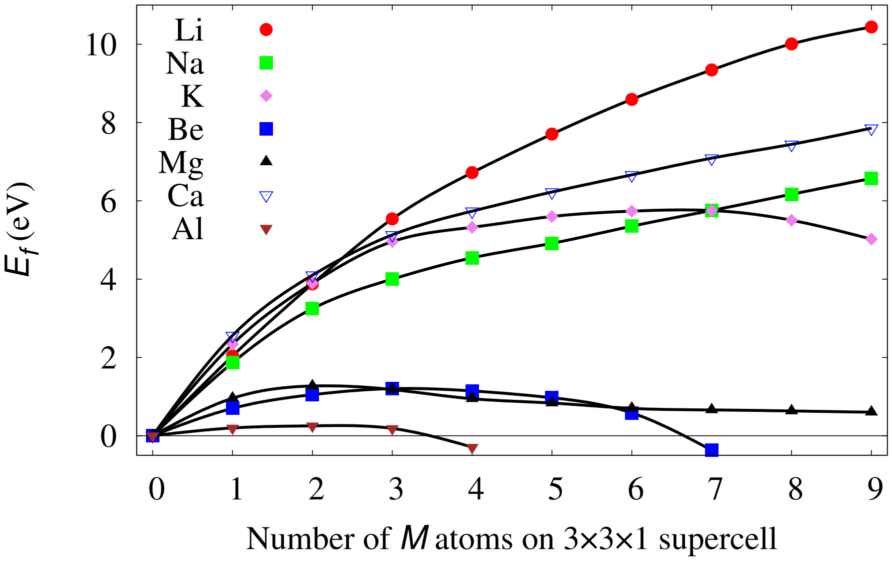

Figure 3.2: Formation energy (E_f) of monolayer TiS_2 with Li, Na, K, Be, Mg, Ca, or Al atoms on the H-site as a function of metal ion concentration.

ions and 1914 $mAhg^{-1}$ for alkaline earth metal ions are possible. This shows that the specific capacity of monolayer TiS_2 is much higher than that of monolayer SnS_2 [110]. These results are comparable with those reported for the defective graphene [80].

3.3.3 Voltage

A cell with high voltage is one of the requirements of an efficient battery. Theoretically, the open circuit voltage (OCV) of the electrode material can be measured to estimate the net voltage of a cell roughly. A low OCV of the anode means the possibility of a high net cell voltage. Fig. 3.3(a) shows the OCV profile for the metal ion adsorption over the surface of the monolayer TiS_2 as a function of the increasing number of metal ions ($M_n\mathrm{TiS}_2$: $1 \leqq n \leqslant 9$), while Fig. 3.3(b) shows the averaged OCV of these ions. The reversible reaction at the anode can be written as:

$$\mathrm{TiS}_2 + nM^{Z+} + Zn\bar{e} \rightleftharpoons M_n\mathrm{TiS}_2$$

where $\bar{e}$ is the charge on an electron. The OCV for the metal ions is defined as:

$$V = -[E(M_n\mathrm{TiS}_2) - E(\mathrm{TiS}_2) - nE(M_{bulk})]/Ze$$

where $E(M_{bulk})$ is the energy per atom in the most stable bulk structures of metal atoms. The voltage profile for all the metal ions has been calculated by filling the top H-sites of a 3×3×1

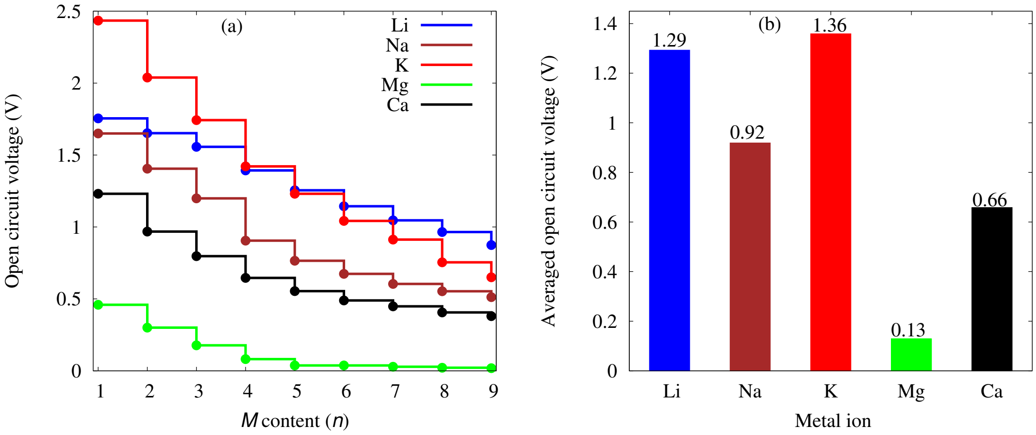

Figure 3.3: (a) A comparison of the open circuit voltage of different metal ions adsorbed at H-sites of the monolayer TiS_2 as a function of metal ion content (n). (b) A comparison of the averaged open circuit voltage of the monolayer TiS_2 as an anode material for different metal ions in the range of $1 \leq n \leq 9$.

TiS_2 supercell using the definition of V in the equation above. The dropping voltage with the increasing metal ion concentration has also been reported for graphite and other anode materials in previous studies [95, 112]. A low OCV of the anode is useful to have a net high cell voltage however the OCV should be higher than 0 which otherwise means metal cluster formation is possible. Fig. 3.3(b) shows that Mg has the lowest OCV, a high voltage cell is expected for the Mg ion battery compared to the LIBs.

3.3.4 Diffusion of metal ions

The diffusion kinetics of alkali and alkaline earth metal ions on the surface of TiS_2 is important as it is related to the charge/discharge rate. A high diffusion rate is required for fast recharge [113]. A minimum energy path (MEP) for the diffusion of alkali and alkaline earth metal ions is optimized with the NEB method by using the linear interpolation of three images between the H- and T-sites. Table 3.1 shows only a small difference in the adsorption energy of a metal ion at the H- and T-sites, so all the metal ions are expected to have a MEP for the diffusion from an H-site to the nearest neigh- boring H-site via the T-site.

All the metal ions have the same trajectory of diffusion in a curved zigzag path as shown in Fig. 3.4(c). This path is similar to the diffusion path of a Na ion on the surface of the monolayer SnS_2 [110]. The relative energy profile in Fig. 3.4 is symmetric both about the H- and T-sites (because of its three-fold rotational symmetry about the H- and T-sites) of the monolayer TiS_2. Each metal ion at the H- or T-sites can move along three similar paths, located at an in-plane angle of 120°. All the metal ions studied here have the highest adsorption energy

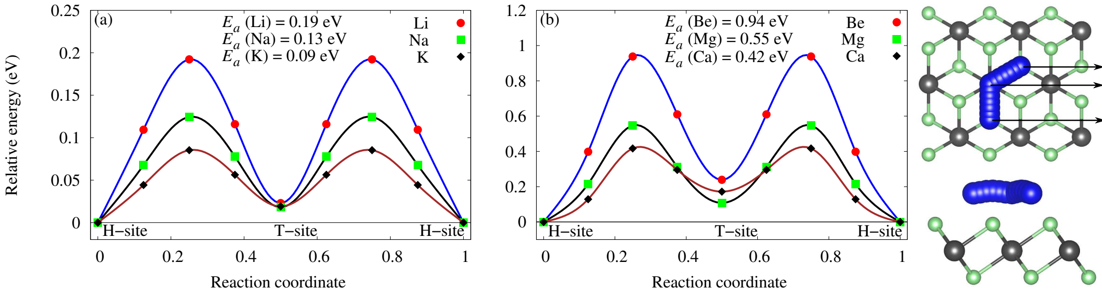

Figure 3.4: Relative energy profile for the diffusion of (a) monovalent and (b) divalent metal ions on the surface of monolayer TiS_2 from an H-site to its nearest neighboring H-site via the T-site between these two H-sites. (c) Top and side views of the trajectory of Li ion diffusion over the surface of monolayer TiS_2. The trajectories for the diffusion of other metal ions are similar to that for Li.

at the H-site. The E_{ad} of each atom at the H-site in Fig. 3.4 is taken as a reference while the energy at all other points is relative to the E_{ad} at the H-site. Fig. 3.4(a) shows the relative energy profile and the activation energy barriers (E_a) for the diffusion of monovalent alkali metal ions. The calculated E_a along the MEP for Li, Na, and K are 0.19 eV, 0.13 eV, and 0.09 eV, respectively. A decreasing trend in the E_a of alkali ions is found. A similar behavior is observed in the E_{ad} as well while the M–S distance has shown an increasing trend down the group because of the increasing ionic size. These interactions depend upon the charge and distance, independent of the mass of the ions. The difference in the charge transferred by an ion of the same group is so negligible that the E_a for the ions in the same group decreases down the group. This behavior of the alkali metal ions is consistent with previous reports [53, 114]. The results in Fig. 3.4(b) show the energy profile for alkaline earth metal ions relative to their corresponding E_{ad} at H-sites. The trend of the relative energy profile for the diffusion of alkaline earth metal ions is similar to that of the alkali metal ions. However, the E_a of the divalent Be, Mg, and Ca is much higher than E_a of alkali metal ions. The increase in E_a for the divalent ions is due to their higher charges which produce higher perturbation in the monolayer TiS_2 compared to the monovalent alkali ions.

3.3.5 Electronic properties

There have been many anode materials studied for metal ion batteries, but most of them are insulators (for example MoS_2, phosphorene, and SnS_2) [115–118]. An intrinsically conductive electrode material is necessary for high recyclability. It allows for the full discharge of a battery which is needed for the optimum performance of a rechargeable battery. Fig. 3.5 shows the total density of states for the pristine monolayer TiS_2, monolayer TiS_2 with Li, Na, K, Mg, or Ca ions adsorbed, occupying the top H-sites of the monolayer, using the HSE06

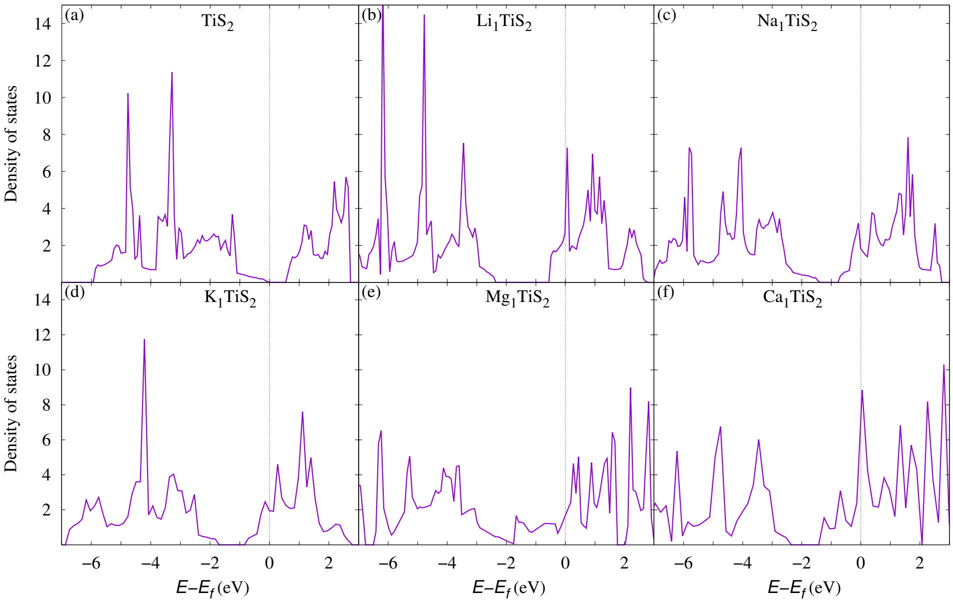

Figure 3.5: Total density of states for (a) TiS_2, (b) Li_1TiS_2, (c) Na_1TiS_2, (d) K_1TiS_2, (e) Mg_1TiS_2, and (f) Ca_1TiS_2. It shows that TiS_2 is a semimetallic with a small bandgap of 0.62 eV in its pristine state, but becomes metallic after the adsorption of metal ions. The data shown here is calculated by the HSE06 method.

method. We also have these calculations with the GGA method. The Fermi level is scaled to zero. It shows that the 1T phase of pristine monolayer TiS_2 is semi-metallic with a band gap of 0.62 eV, which matches well with the previous report [109]. It becomes metallic with the adsorption of metal ions. The increase in electronic con- ductivity is due to the extra electrons donated by the metal atoms. On the other hand, GGA calculations show that even the pristine monolayer TiS_2 is also metallic. The previous studies have demonstrated a reduction of the band gap of the anode materials with the increasing metal ion concentration, which is consistent with our results [115, 118].

3.4 Conclusions

We systematically studied the adsorption and diffusion of alkali and alkaline earth metal ions on the surface of monolayer TiS_2 in search of efficient alternatives to Li. Our calculations show that the 1T structured monolayer TiS_2 is energetically more stable than the 2H one. It is found that all the metal ions have two favorable adsorption sites (the H- and T-sites), while the H-site is a more favorable adsorption site. Monolayer TiS_2 has a high adsorption capacity for the metal ions studied, except Be and Al. The divalent Ca and Mg ions give the highest specific capacity (1914 $mAhg^{-1}$) that is double of the specific capacity of the Li, Na, and K (957 $mAhg^{-1}$) ions. The monolayer TiS_2 can have a very low storage capacity for the Be and Al ions, which is due to the fact that these ions have very high cohesive energies in their stable bulk metallic structures. The Mg ions have the lowest averaged open circuit voltage of 0.13 V over an Mg adsorption range Mg_nTiS_2, ($1 \leq n \leq 9$). The NEB calculations show that all the metal ions easily diffuse from an H-site to the nearby H-site via the T-site between them through a curved zigzag path. The activation energy barrier for the diffusion of metal ions decreases down the group due to the increased M-to-S distance (because of the increasing ionic size) and the decreased adsorption energy. The diffusion energy barriers for the divalent metal ions are higher than those of the monovalent alkali metal ions. The pristine monolayer TiS_2 is semi-metallic and it becomes metallic with the adsorption of metal ions, because of the extra electrons donated by the metal ions. Our study shows that Li can be replaced by Mg, where high energy density storage and a high cell voltage is required, while Na can replace it in large stationary batteries.

Chapter 4

Monolayer W_2C as anode material

4.1 Introduction

Numerous properties of thin films are dependent on the thickness of the films [119]. The successful isolation of graphene and its robust properties have brought a breakthrough in the science of nanomaterials [1, 2]. It attracted the focus of researchers to the synthesis, characterization, and theoretical study of monolayer, bilayer, and few-layer two-dimensional materials with a thickness of the order of atomic diameters. Soon after the successful isolation of graphene, many freestanding monolayers like MoS_2, WS_2, SnS_2, BN, etc. were discovered [120]. Owing to the variety of band gaps, adsorption, and mechanical and chemical properties these materials have shown potential for use in nano-sized electronic, optoelectronic, energy harvesting, and data storage devices [110, 121–127].

Nanoscale rechargeable batteries can be used as a power supply for the regular operation of nano-devices. There have been many research studies in this area. Computational methods can provide an atomic-level understanding of crystal structures, phase transformations, electronic and ionic transport mechanisms, charge transfer, and binding energies of adatoms, and important properties such as reversible ion storage capacity, stability under high capacity, charge/discharge rate, open circuit voltage (OCV), etc. can be well-estimated [113, 128–130].

Na, the most abundant, cheap, and non-toxic metal, has a similar chemical nature to the scarce and costly Li. However, its ionic size and weight are larger than those of Li. The increasing demand for rechargeable batteries requires a suitable alternative to Li. Studies on batteries show that Na is the most possible candidate as an alternative to Li when high energy density is not the first priority [86, 89, 131, 132].

The electrochemical performance of Li/Na ion batteries depends mainly upon the choice of electrodes and electrolytes. A great research struggle has been devoted to the discovery of valuable component materials for rechargeable batteries [133]. Li/ Na conductive solid inorganic electrolytes are highly expected to replace flammable organic liquid electrolytes to ensure safety and reduce leakage as well [134–136]. Si and SnO_2 have been reported as the highest capacity anode materials, but a large volume expansion is observed with increasing Li/Na concentration [137, 138]. Transition metal dichalcogenides also have high Li/Na storage capability and low diffusion barriers for the migration of Li/Na ions, but most of them are insulators [139–141]. Two-dimensional carbon-related materials have been studied for Li/Na adsorption. Graphene is ideal as an anode material because it is metallic and has high mechanical strength. Its low adsorption capacity for Li/Na can be increased by the formation of vacancies or the partial substitution of C with B or N. Graphene has been used as a conductive additive in electrode materials. However, these strategies may lower the charge/discharge rate of batteries [95, 110, 121, 142–147].

In this article, the density functional theory (DFT) method is applied to explore freestanding monolayer W_2C. The structure, energetic, mechanical, dynamic, and thermodynamic stabilities, electronic band structure, and density of states of monolayer W_2C are discussed. After this, the adsorptions of single and multiple Li/Na, and their transport mechanism over the monolayer W_2C is broadly discussed. The monolayer W_2C is intrinsically metallic as required for electrodes of rechargeable batteries. Its high mechanical stiffness is valuable to avoid large expansion during the adsorption of Li/Na ions. It has a low OCV, which is crucial in producing high voltage cells. Its structural symmetry provides multi-directional minimum energy pathways for the easy transport of Li/Na ions. All these properties can make the monolayer W_2C a long-life and ultrafast rechargeable anode material.

4.2 Computational details

All our results are based on the spin-polarized DFT implemented in the Vienna Ab initio Simulation Package using the projector augmented wave method [100]. The generalized gradient approximation with the parameterization scheme of Perdew–Burke–Ernzerhof [70] is used for the exchange-correlation functional. A cutoff energy of 600 eV is chosen, for the plane-wave expansion of the electronic eigenfunctions, for the monolayer W_2C. The force criterion for the atomic relaxation is selected as 0.001 eV/Å. The periodic images of monolayer W_2C are separated by a distance of 20° Å to bypass the interlayer interactions. The k-point sampling with a $6\times6\times1$ mesh is used for the integration of the Brillouin zone (BZ). The finite difference method is used to calculate the elastic constants. The displacement step size is selected as 0.015 Å using four displacements for each ion in the x and y directions. Phonon calculations are performed using the finite displacement method, as implemented in the Phonopy program [148]. A $5\times5\times1$ supercell of monolayer W_2C with the atomic displacements of 0.01 Å is

Table 4.1: Distance from W (d), binding energy (E_b), and charge transferred (q) by Li/Na adatoms on adsorption at the H- (hollow) or C-site (above-carbon) of monolayer W_2C

	d (Å)		E_b (eV)		q (e)	
	H-site	T-site	H-site	T-site	H-site	T-site
Li	2.90	2.91	0.87	0.86	0.87	0.86
Na	3.19	3.20	0.88	0.87	0.76	0.76

considered for the phonon calculations. A 6×6×1 supercell is considered for ab initio molecular dynamics simulations at 300 K with each time step of 3 fs to test the thermal stability of the monolayer W_2C at room temperature. A 3×3×1 supercell of W_2C is examined for the adsorption and diffusion of Li/Na ions. The nudged elastic band method [103] is used to find the minimum energy paths for the diffusion of Li/Na ions on the surface of the monolayer W_2C. Bader charge analysis is used to measure the charge transferred by the Li/Na adatoms [149].

4.3 Results and discussion

4.3.1 Structural stability

Fig. 4.1(a) shows the top and side views of a portion of the 2H phase of monolayer W_2C. Its geometry is similar to that of the 2H phase of monolayer WS_2, where the S positions have been occupied by the W atoms and the W positions by the C atoms. The optimized lattice parameters of monolayer W_2C in its 2H phase are a=b=2.84 Å, whereas the W–C bond length is 2.15 Å. For the 1T phase of monolayer W_2C, both a and b lattice parameters are 2.87° and the W–C bond length is 2.12 Å. The formation energy per atom (E_f) for the monolayer W_2C is defined by

$$E_f = (E_{W_2C} - 2E_W - E_C)/3$$

, where E_{W_2C} is the total energy of a unit cell of the monolayer W_2C, and E_W and E_C are the energies of an isolated atom of W and C, respectively. By this definition, E_f for monolayer W_2C in its 2H phase is 9.39 eV per atom, whereas it is 9.22 eV per atom for its 1T phase. It shows that the monolayer W_2C is energetically more stable in the 2H phase than in the 1T phase.

The evolution of high amount of energy in the formation of the monolayer W_2C from W and C atoms shows the high strength of the W–C bond. Its in-plane stiffness

$$Y = (C_{11}^2 - C_{12}^2)/C_{11}$$

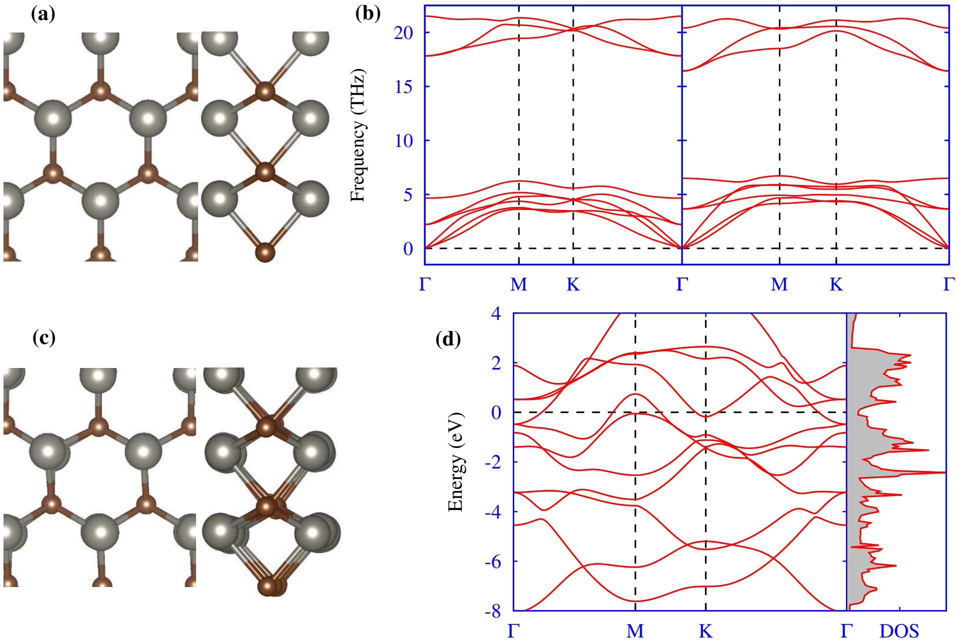

Figure 4.1: Top and side views of a portion of monolayer W_2C in the 2H phase. (b) Left-hand panel: phonon modes for the 1T phase of the monolayer W_2C, showing that the 1T phase is dynamically stable. Right-hand panel: phonon modes for the 2H phase of monolayer W_2C, showing that the 2H phase is dynamically stable. (c) Snapshot of the 2H phase of monolayer W_2C taken after 1000 steps at 300 K, showing that the monolayer is stable at room temperature. (d) Electronic band structure and density of states of the monolayer W_2C (the Fermi level is scaled to zero), showing that the pristine monolayer W_2C is metallic.

is 278.6 N/m, while the Poisson ratio $\nu = C_{12}/C_{11}$ is 0.438. Here the elastic constants $C_{11} = C_{22}$=344.67 N/m, and $C_{12} = C_{21}$=150.92 N/m due to the hexagonal symmetry. The in-plane stiffness of monolayer W_2C is much higher than that of monolayer MoS_2 (120 N/m) and is less than that of graphene (340 N/m) [150, 151]. The lattice dynamics of the monolayer W_2C both in the 1T and 2H phases are studied by calculating their phonon dispersion relations. The result for the 1T phase of the monolayer W_2C is shown in the left-hand panel, while the result for the 2H phase is shown in the right-hand panel of Fig. 4.1(b). The absence of soft modes over the entire BZ of monolayer W_2C in the 1T and 2H phases confirms its dynamical stability in both these phases. There are three acoustic and six optical modes in the phonon spectra of the monolayer W_2C. The dispersion of the in-plane longitudinal and transverse acoustic modes is linear, whereas that of the out-of-plane acoustic mode is quadratic near the Γ-point. This behavior of the phonon modes is similar to that of other dynamically stable monolayers [21, 51, 152]. Although both the 1T and 2H phases of the monolayer W_2C are dynamically stable, the 2H phase is energetically more stable by 170 meV per formula unit than the 1T phase; therefore, we consider the 2H phase of the monolayer W_2C for the adsorption and diffusion of Li/Na ions. Fig. 4.1(c) shows a snapshot of the geometry of the monolayer W_2C after being run for 1000 steps (3 ps) at room temperature. Small deviations of W and C from their original positions with geometric reconstructions and no bond breaking confirm its thermal stability at room temperature. The electronic band structure and the density of states of the pristine monolayer W_2C with a Fermi level scaled to zero are shown in Fig. 4.1(d). Both the band structure and the density of states show no band gap for the monolayer W_2C, as highly desired for electrode materials.

4.3.2 Adsorption

It is important to understand the binding strength (E_b) per adatom A (A = Li and Na) with the monolayer W_2C as a substrate because most of the key terminologies associated with batteries, such as reversible storage capacity, OCV, and power density, for example, are derived from the E_b of the ions adsorbed by the electrode material. We define the E_b of the A-atom with the monolayer W_2C with respect to the bulk energy of the A-metal ($E_{A_{bulk}}$) so as to exclude the metallic clustering of the adsorbed ions:

$$E_b = -(E_{A_x\mathrm{W_2C}} - E_{\mathrm{W_2C}} - xE_{A_{bulk}})/x$$

[145]. $E_{A_x\mathrm{W_2C}}$ and $E_{\mathrm{W_2C}}$ are the total energy of a 3×3×1 supercell of the monolayer W_2C plus x number of A-adatoms and the total energy of a 3×3×1 supercell of the pristine monolayer W_2C, respectively. To find the energetically most favorable position for the adsorption of a

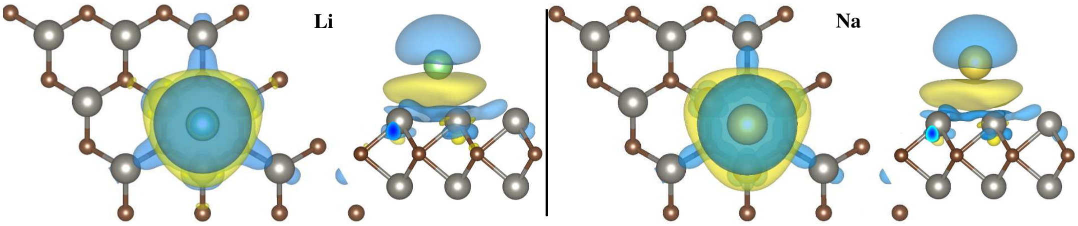

Figure 4.2: Top and side views of the charge density difference ($\Delta\rho$) for Li (left-hand panel) or Na (right-hand panel) adsorbed at the H-site of the monolayer W_2C. Electron gain upon Li/Na adsorption is indicated in yellow at an isosurface of 1.89×10^{-3} e/Å^3 and loss in light blue at an isosurface of 1.89×10^{-3} e/Å^3.

single A-atom, we examine the E_b of a single A-atom at different positions over the monolayer. The most favorable position is above the center of a W–C hexagon, as shown in Fig. 4.6(b). We call this position the H-site. The second favorable position is above each C atom, which we call the C-site. Some basic information about a single A-atom adsorption is given in Table 4.1.

The charge density difference ($\Delta\rho$) is defined by

$$\Delta\rho = \rho_{\mathrm{W_2C}+A} - \rho_{\mathrm{W_2C}} - \rho_A$$

(in the unit of eÅ^{-3}), where $\rho_{\mathrm{W_2C}+A}$ is the charge density of a $3\times3\times1$ monolayer W_2C with a single A-atom adsorbed on its H-site, $\rho_{\mathrm{W_2C}}$ is the charge density of the $3\times3\times1$ monolayer W_2C, and ρ_A is the charge density of an isolated A-atom where all the atoms always have the same positions as in the whole system. The side and top views of $\Delta\rho$ upon the adsorption of a Li and a Na atom are shown in the left and right-hand panels of Fig. 3.2. It clearly shows that A-atoms are ionized when they are adsorbed on the surface of monolayer W_2C, and it is consistent with the Bader charge analysis results, as listed in Table 3.1. It means that the monolayer W_2C is equally useful for Li and Na adsorption at low concentrations. However, in Fig. 3.3 we explain why the monolayer W_2C has comparatively low intrinsic quantum capacitance for Na adsorption than that for Li.

After a detailed discussion on the adsorption of a single A-atom, we study the effect of increasing concentration of adsorbed A-atoms on the total binding energy of the x A-atoms ($E_{b(x)} = xE_b$). $E_{b(x)}$ puts an upper limit on the adsorption concentration of A-atoms. Fig. **??**(a) shows the plot of the $E_{b(x)}$ against the number of A-atoms. It shows that the $E_{b(x)}$ for Li is almost linear with increasing Li concentration throughout filling all the available H-sites, while in the case of Na it suddenly drops after filling 14 H-sites (seven from the top and seven from the bottom of the monolayer). It shows that the intrinsic quantum capacitance of the monolayer W_2C reaches saturation before filling all the available H-sites in the case of Na

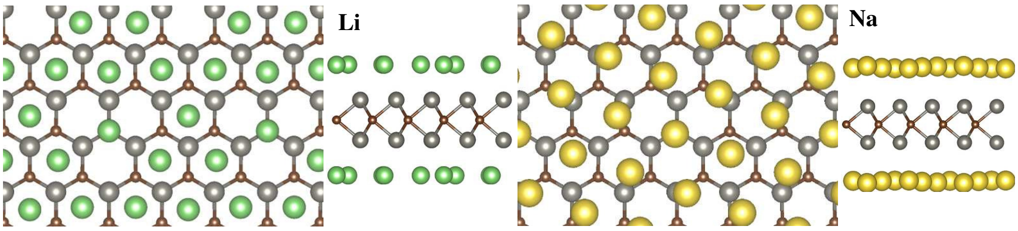

Figure 4.3: Top and side views of the adsorption sites at high concentrations (14 atoms per supercell) of Li (left-hand panel) and Na (right-hand panel). Li atoms are fixed to the energetically favorable H- or C-sites. Na atoms are uniformly distributed over the surface of the monolayer W_2C irrespective of the favorable adsorption sites.

adsorption, while in the case of Li adsorption all the H-sites can be loaded without metallic clustering. This result is consistent with our Bader charge analysis. The Bader charge on a Li adatom (0.87 e) is more than that on a Na adatom (0.76 e) when adsorbed on the H-site of the monolayer W_2C. In the Li adsorption case, even filling the C-sites when all the H-sites are already filled is energetically possible.

The specific capacity of the monolayer W_2C with the unit mAh/g is defined by the equation

$$C = xF/M_{\mathrm{W_2C}}$$

where x is the number of Li/Na ions stored on the selected supercell of monolayer W_2C, F (26801 mAh/mol) is the Faraday constant and $M_{\mathrm{W_2C}}$ is the molar mass of the supercell. The maximum specific capacity of monolayer W_2C by this formula turns out to be 292 mAh/g for Li and 113 mAh/g for Na. To further highlight the difference in the adsorption of Li and Na ions at high concentrations, the top and side views of monolayer W_2C with 14 Li (left-hand panel) or 14 Na (right-hand panel) adatoms are shown in Fig. 4.3. The H- or C-sites are selected as the initial adsorption positions for both Li and Na adatoms. However, after relaxation, it is observed that the Li ions are still stacked in their initial positions while the Na ions are uniformly distributed over the surface of the monolayer irrespective of their initial positions. It is because the binding strength of the Li adatoms with the monolayer W_2C is higher than that of the Na adatoms. In other words, the adsorption capability of the monolayer W_2C for the Li atoms is more than that for the Na atoms. This result is consistent with our $E_{b(x)}$ calculations.

Fig. 4.4(b) depicts the voltage profile of the anode with increasing Li/Na concentration. The OCV of a commercial anode should be lower than 0.8 V to have enough high cell voltage, but not too close to zero to avoid dendrite formation [153]. The voltage ranges of 0.84–0.55 V for Li and 0.88–0.37 V for Na are thus quite suitable. The expansion of anodes with increasing A-atom concentrations has been reported as a genuine issue [137]. However, the

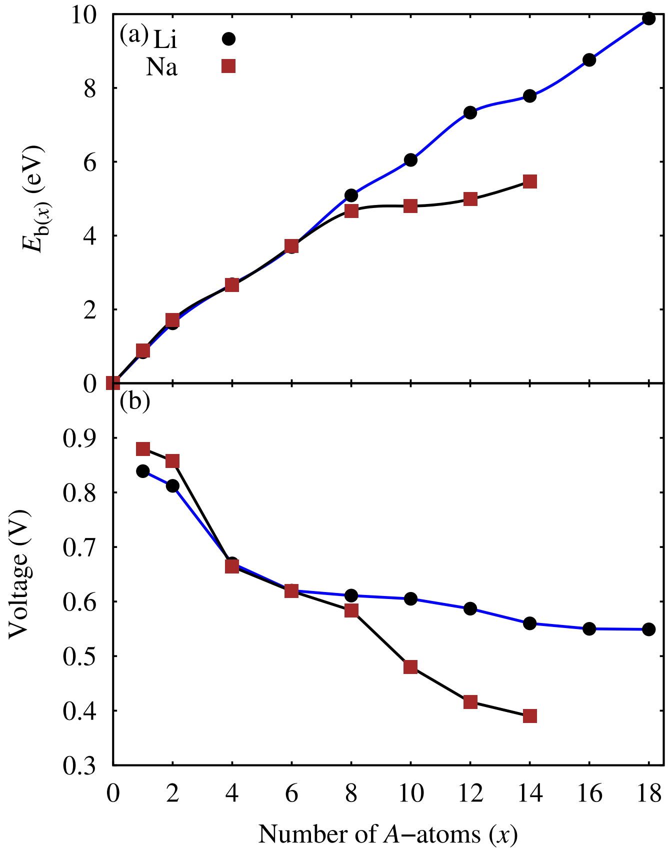

Figure 4.4: (a) Total formation energy ($E_{b(x)}$) and (b) OCV versus concentration of A-adatoms on a 3×3×1 W$_2$C supercell. After loading 14 Na ions, no further Na storage is possible. In the Li adsorption case, all the top and bottom H-sites can be filled without the formation of metallic clusters.

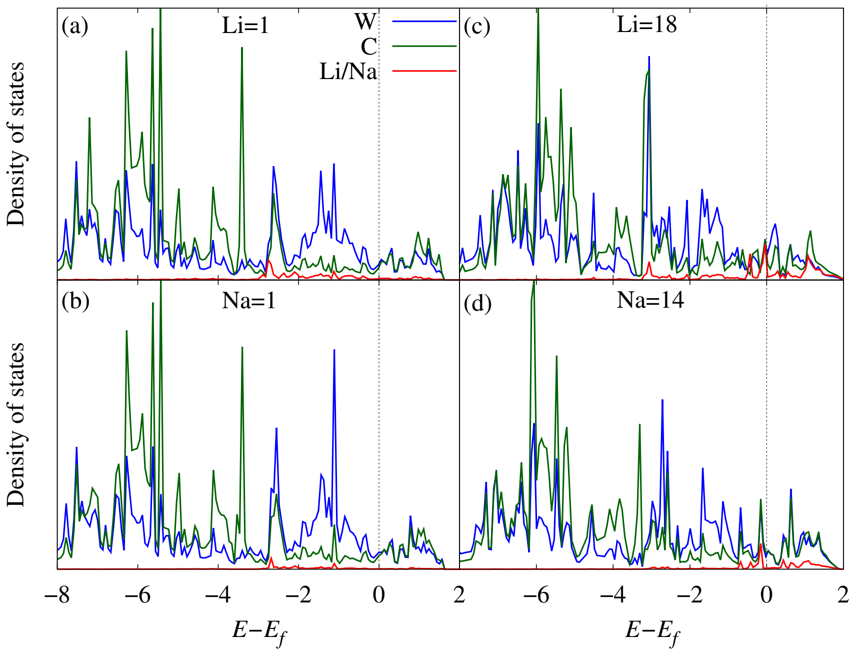

Figure 4.5: Partial density of states per atom for (a) 1-Li-, (b) 1-Na-, (c) 18-Li-, and (d) 14-Na-adsorbed monolayer W_2C in a $3\times3\times1$ supercell.

area expansion, even for a fully loaded monolayer W_2C, is negligible both for Li and Na adsorptions. This low expansion is due to the high in-plane stiffness of the monolayer.

During the charge/discharge process of an A-ion battery, a reversible electrochemical reaction occurs both at the anode and cathode. The reversible reaction at the anode is given by:

$$xA + x\bar{e} + \mathrm{W_2C} \rightleftharpoons A_x\mathrm{W_2C}$$

The electrons produced in this reaction move through the outer circuit of the battery, while the positive A-ions move through the electrolyte between the electrodes. The reaction can be accelerated by introducing electrode materials having high mobility both for electrons and the A-ions. We have already shown that the pristine monolayer W_2C is metallic which will be helpful in the full recovery of the charge carriers.

To study the effect of the incoming A-ions on the electronic structure of the monolayer W_2C, the partial density of states per atom for a single A-atom adsorbed monolayer W_2C is shown in Fig. 4.5(a) and (b). Fig. 4.5(a) and (b) show that the electronic structures of monolayer W_2C with the adsorption of Li or Na adatoms are similar and the contribution of the A-atom is negligible, but the system as a whole is metallic. Increasing the number of A-atoms (Fig. 4.5(c) and (d) for 18 Li and 14 Na adatoms, respectively) causes the density of states for A-atoms to cross the Fermi-level, which means that the increasing concentration of

A-atoms increases the electronic conductivity of the system. Most of the reported electrode materials are insulating; that is why some conductive additives, graphene for example, are needed to make them metallic [110, 138]. However, the addition of graphene increases the ion diffusion barrier. Additionally, it may increase the cost of the electrode material due to the experimental complications.

4.3.3 Diffusion

Fast ion and electron transport in the electrodes are needed to decrease the charge/discharge time of batteries. Short charging time for mobile phones or laptops may not be as necessary as it is for electric vehicles. The discharge rate shows how much power a battery can deliver. We already have shown that the pristine and the *A*-atom adsorbed monolayer W_2C are metallic. The ion diffusion at a particular temperature can be studied directly by the use of AIMD simulations.

However, finding the energy barrier for the transition states of *A*-ions at 0 K by the NEB method can provide sufficient theoretical insight into the intercalation compounds. Fig. 4.6 shows three different diffusion paths for *A*-ions. The H-sites are taken as the initial and final points since they are the most favorable adsorption sites. The path from an H-site to a nearby H-site via a C-site is taken as path 1, that from an H-site to a nearby H-site via a W-site as path 2, and the direct path from an H-site to a nearby H-site as path 3. Path 1 is the minimum energy path, both for Li and Na diffusions. The energy barrier along path 1 for the diffusion of a single Li ion is 0.035 eV and 0.019 eV for a Na ion. As the diffusion rate of ions has an exponential dependence on the activation energy barrier (by the Arrhenius equation), even a small decrease in the barrier may bring a significant increase in the diffusion rate. The activation energy barrier noticed here is much lower than the reported ones of other anode materials [110, 112, 144, 147]. The activation energy for the diffusion of a Na ion is lower than that of a Li ion, which is consistent with the report for monolayer MoN_2 and our study on monolayer TiS_2 [53].

The energy barrier for the diffusion of Na ions is so small that at high concentrations the adsorbed ions have a uniform distribution over the monolayer irrespective of the favorable adsorption sites, to reduce the repulsive Coulombic forces between the positive ions (see Fig. 4.3). This superionic mobility of the monolayer can reduce the charge/discharge time of the anode.

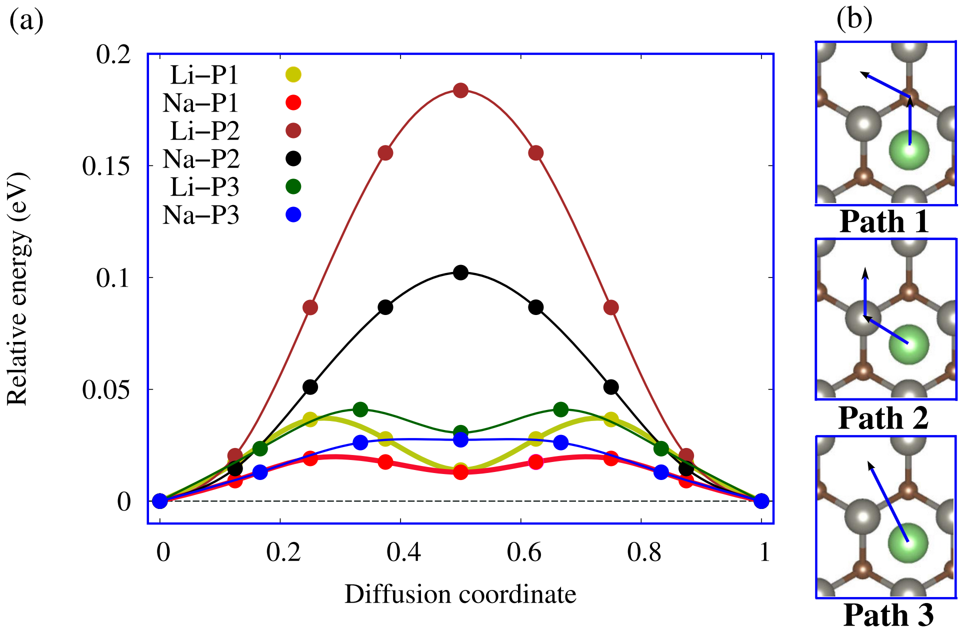

Figure 4.6: (a) Relative energy profile for the diffusion of Li/Na from an H-site to a nearby H-site through three different paths, where path 1 has the lowest energy barrier. (b) Schematics of the different diffusion paths.

4.4 Conclusions

In conclusion, our DFT-based studies show that monolayer W_2C is more stable in the 2H phase than in the 1T phase. It has a metallic electronic structure and high mechanical stiffness of 278 N/m. Its high adsorption capacity for Li/Na and metallic nature makes it a fascinating anode material. Its structural symmetry provides the adsorbed ions with multidirectional ultrafast diffusion pathways with a low activation energy barrier (of 0.035 eV for Li and 0.019 eV for Na). Its charging voltage range (0.82–0.55 V for Li and 0.88–0.37 V for Na) lies within those of commercial anodes. Its area expansion with increasing Li/Na ion concentration is negligible. This study recommends the monolayer W_2C as fast charging, long-life anode material.

Chapter 5

Structure and applications of the UGO monolayer

5.1 Introduction

Increasing the surface area by nanostructuring is one of the best approaches for enhancing the materials properties induced from the surface. This nanoscale miniaturization has led materials scientists to accomplish a suspended single layer of graphite, termed as graphene [1]. Graphene being the real thinnest material has received significant interest due to its high mechanical strength, environmental stability, and astonishing transport properties [154]. Earlier studies on graphene revealed that the pristine graphene was not proper for manufacturing electronic nanodevices because of its metallic nature and it was modified for attaining the desired properties. For instance, graphene functionalization with hydrogen and fluorine causes bandgap opening, produces polarization and piezoelectricity [155, 156].

Graphite has been effectively used as a commercial anode material in the Li ion batteries (LIBs) due to its facile Li insertion/extraction, abundant resources, low cost, high Li storage capacity (372 mAh/g), high stability, and high recyclability [157]. Even though many layered materials and their hybrids are the best fit for LIB anodes, carbonaceous materials have no substitute for LIB anodes [110, 117, 158]. Disordered carbon as an anode has been reported to have a Li storage capacity of 500 mAh/g [159]. However, the power rate capability of the porous amorphous carbon can be lower due to its low electronic conductivity. A body-centered orthorhombic carbon (bco–C_{16}) [160] has a higher capacity for storing Li and a lower diffusion barrier at high capacities than graphite [161].

Unlike graphite and amorphous carbon, Li adsorption on pristine graphene is thermodynamically unstable compared to the bulk Li [162, 163]. The graphene surface activated with double vacancy and stone Wales defects interacts strongly with the adsorbed Li ions. Furthermore, the strength of interaction strongly depends upon the type of the defect [164]. The Li adsorption capacity of graphene can also be enhanced by introducing electron deficiency via boron doping [142, 165, 166]. In this manner, the Li adsorption capacity of graphene can be increased to approach to the corresponding adsorption level of graphite. A recently discovered allotrope of the graphene, known as the penta-graphene has a high Li storage capacity of 1489 mAh/g and high electronic and ionic conductivity [21, 167]. Similarly, the monolayer carbon ene-yne graphyne and boron-graphdine have been reported to have a high Li storage capacity with an estimated diffusion barrier of 0.6 eV [168, 169]. These earlier investigations confirm that the introduction of defects or structural changes in graphene can lead to high Li storage capacity.

In this letter we present the structure of crystalline unzipped graphene oxide (UGO) monolayer (C_2O) by studying its energy, relying on the electric dipole alignments. The structure stability is then supported by providing stable phonon modes. The UGO monolayer looks like the zigzag graphene nanoribbons linked via O atoms. The interaction O lone-pair electrons with the bond-pair electrons causes structural bending and induces the electron excessive and deficient regions in the graphene. Li ions can be trapped in the electron deficient regions of the UGO monolayer with ease and thus it proves to be a good way to enhance the Li adsorption capacity of graphene. The Li adsorption capacity of the UGO monolayer is over 419 mAh/g, which is much higher than graphite and comparable to the defected graphene. The energy barrier of 0.60 eV for a Li ion migration on the UGO monolayer is not so much low but comparable to those of the recently reported anode materials [168, 170]. The high energy barrier for Li diffusion is due to the localized positive charge regions. The band structure of the UGO monolayer has the Dirac cone similar to graphene with a small band gap opening. This shows that the UGO monolayer can have high electron and hole mobility, which makes it promising for nanoscale electronics. The bandgap of the UGO monolayer is so small that even a low concentration of the Li adsorption can make metallic. The lithiation open circuit voltage of this material is in the range 0.94 to 0.19 V which is the voltage range for a typical anode materials for LIBs.

5.2 Computational details

All the results presented here are based on the density functional theory (DFT), implemented in the Vienna *Ab-initio* Simulation Package (VASP) [100]. The generalized gradient approximation (GGA) within Perdew, Burke, and Ernzerhof (PBE) parameterization [70] are used for the electron-electron exchange correlations. The ion-electron interactions are processed using the projector augmented wave (PAW) method [69, 101]. A cutoff energy of 600 eV is considered for the plane-wave expansion of the electronic eigenfunctions, for the UGO monolayer. A mesh of $7\times10\times1$ k-points is sufficiently dense for the convergence of Brillouin zone integration. Interlayer distance of the UGO is increased to 30 Å to treat the UGO monolayer as an isolated system. The DFT-D3 [171] method is used for the UGO monolayer with and without Li ions adsorbed to count for the contribution of van der Waals interactions. Phonon band structures are calculated using the finite displacement method implemented in the Phonopy program [148]. Wannier90 code is used to analyze the effects of O lone pair electrons on the crystal structure of the unzipped graphene oxide monolayer [172–174]. The nudged elastic band method (NEB) [103] is used to optimize the steepest descent minimum energy path of the Li migration. The PBE and HSE06 [175] functionals are used to analyze the band structure and electronic density of states of the pristine and Li adsorbed UGO monolayer. The electronic charge transferred by the Li adatoms is measured using the Bader charge analysis [149].

5.3 Results and discussion

5.3.1 Energetic and dynamic stability

There have been a very few studies on the structural and electronic properties of the periodic graphene oxide (GO) monolayer. Two structures were suggested for the GO monolayer. In both cases an oxygen (O) atom is bonded to two carbon (C) atoms, lying above the center of the C-C bridge. In the first case the C-C bond is not broken, and this structure of the GO is called the clamped graphene oxide (CGO) monolayer. In the second case the C-C bond is broken to unzip the graphene, and it is called the UGO monolayer. The latter looks like zigzag graphene nanoribbons interlinked by O atoms. Since the earlier reports showed that the UGO monolayer was energetically more stable than the CGO monolayer, we concentrate on the UGO monolayer in this study. The simplest possible unit cell for the UGO monolayer consists of five atoms (C_4O), four from C and one from O [176, 177]. Local electric dipole moments are produced due to the difference in electronegativity of the O and C atoms in the UGO monolayer. This unit cell, however, shows the ferroelectric alignment of the local dipoles only and misses the information of other possible dipole arrangements. In order to study energetically the most stable structure of the UGO monolayer by considering all possible alignments of the dipoles we extend the C_4O unit cell to $C_{16}O_4$. Furthermore to study the dynamical stability the phonon dispersion modes for these structures are also investigated. Fig. 5.1 illustrates four different patterns for the UGO monolayer based on the dipoles alignments.

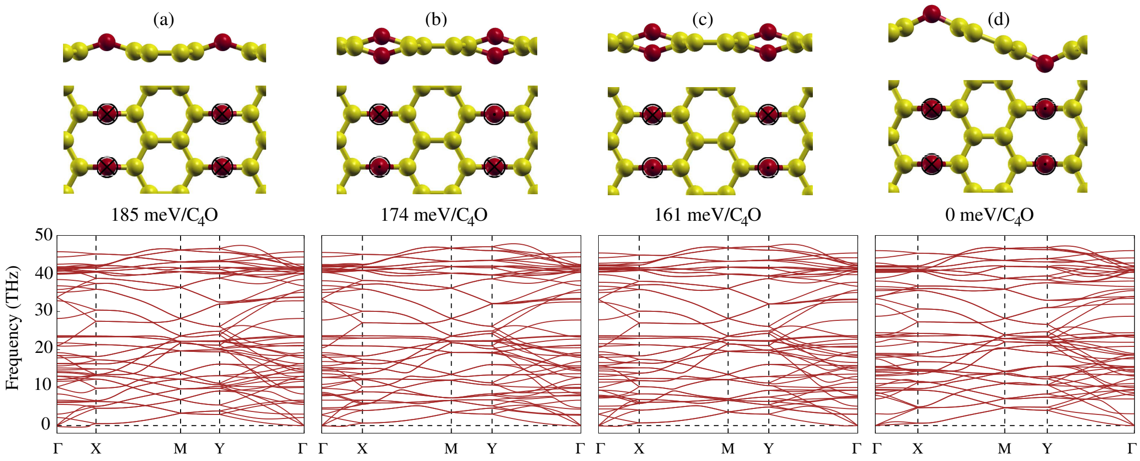

Figure 5.1: Top panel shows the side and top views of possible geometries for UGO monolayer based on the electric dipole configurations. (a) All the dipoles aligned in the same direction, (b) alternating up and down dipoles along both the armchair and zigzag directions, (c) dipoles parallel along the armchair direction and alternating along the zigzag direction, (d) dipoles parallel along the zigzag direction and alternating along the armchair direction. The cross ($\otimes$) and dot ($\odot$) symbols indicate the directions of local dipole moments induced by oxygen atoms while the rectangles show the unit cells. The configuration (d) is energetically the most stable, and the relative energies of four configurations are given below the top paneleach configuration. The yellow and red colored spheres represents C and O atoms, respectively. Bottom panel shows the phonon dispersion curves corresponding to the configurations (a-d).

a = 10.75 Å, 10.81 Å, 10.80 Å, 10.11 Å, and b = 4.97 Å, 4.95 Å, 4.94 Å, 4.97 Å are the respective lattice parameters for the four patterns in Fig. 5.1(a-d).

The pattern in Fig. 5.1(a) with ferroelectric ordering of dipoles was reported in previous studies [176–178]. However, a significant decrease in the energy of the UGO monolayer is seen as a result of altering the dipoles arrangement. Fig. 5.1(d) depicts energetically the most stable pattern for the UGO monolayer. Its energy is lower by 192 meV per C_4O than the one with ferroelectric ordering of dipoles. Stability of this structure is also supported by the stable phonon vibration spectrum. All the acoustic flexural modes (ZA) of phonon dispersion curves in Fig. 5.1(a-c) enter the negative frequency regime as $q \to 0$ excluding Fig. 5.1(d). Even though, such small negative frequencies near the Γ-point can not justify the dynamical instability of these patterns, the huge energy difference between the patterns in Fig. 5.1(a-c) and Fig. 5.1(d) proclaims the pattern shown in Fig. 5.1(d) as the most stable structure for the UGO monolayer.

Although the pattern in Fig. 5.1(a) was reported in the previous studies [176–178], this pattern shows the highest energy among the four structures. The pattern in Fig. 5.1(d) was also reported in several recent studies [178–181]. Thus our results are consistent with the earlier

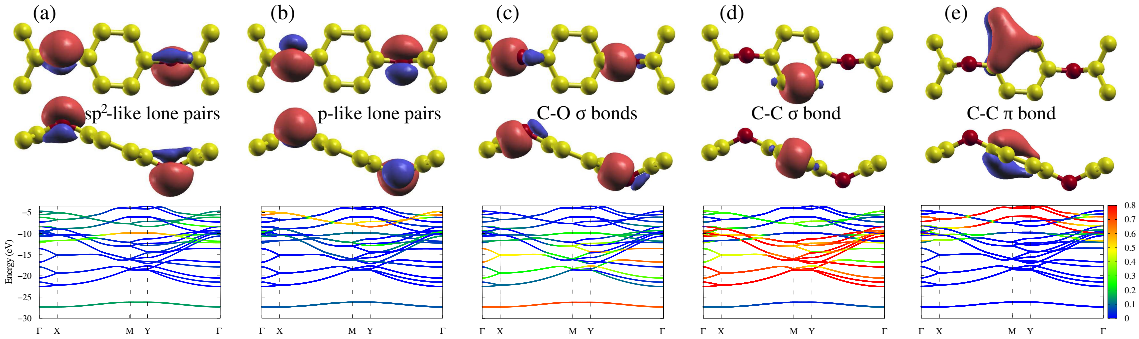

Figure 5.2: The upper panel of (a), (b), (c), (d), and (e) shows the top and side views of the MLWFs associated with the non-bonding sp^2-like lone pairs, p-like lone pairs, C-O σ bonds, a C-C σ bond, and a C-C π bond, respectively. The lower panel of (a), (b), (c), (d), and (e) shows the contribution of each MLWF in the electronic band structure with a color scale.

Table 5.1: Binding (E_b) and adsorption (E_{ad}) energies and Bader charges (q) of a Li atom on $C_{16}O_4$ monolayer adsorbed at sites as shown in Fig. 5.3. The OC site is found to be energetically the most favorable one whereas the O_B and O_{BC} sites are equally favorable for Li adsorption.

	O_{TC}	O_T	C_T	O_{BC}	O_B	O_{BC}	OC
E_b (eV)	-0.617	0.471	-0.067	-0.285	-0.194	-0.193	-0.640
E_{ad} (eV)	-2.221	-1.186	-1.800	-1.888	-1.797	-1.796	-2.244
q (e)	0.88	0.73	0.82	0.88	0.89	0.88	0.88

reports, where a zigzag antiferroelectric pattern possibly being the most stable structure for the periodic UGO monolayer. By doping O in flat pristine graphene, the C-O-C angle in Fig. 5.1(d) comes out to be 128.2°. In order to understand the localized electrons distribution, we analyze MLWFs of the UGO monolayer. MLWFs are calculated for the valence bandsthe unit cell shown in Fig. 5.1(d) (C_8O_2). Thus as a whole 22 MLWFs are produced, each corresponding to two electrons. Four of these representing the Osp^2 and O2p lone pairs, ten the C-C σ bonds, four the C-O σ bonds, and four the C-C π bonds. The MLWFs for sp^2-like and p-like lone pairs, C-O σ bonds, and C-C σ and π bonds are shown in Fig 5.2. The O lone pairs of the UGO monolayer have shifted away the MLWFs associated with the C-O bonds as can be seen in Fig. 5.2(c). Due to the crystalline structure of UGO monolayer, steric hindrance, and existence of the lone pairs, the C-O-C bond angle is 128.2° not 120°. Arguments like lowest possible energy, dynamical stability, and role of the lone pair electrons are enough to justify the pattern shown in Fig. 5.1(d) as the most stable structure for UGO monolayer.

5.3.2 Li adsorption capacity

After we have found the energetically and dynamically most stable structure for the UGO monolayer we want to show its promise as an anode material for LIBs. In order to search for energetically favorable Li adsorption sites over the UGO monolayer, single Li adsorption over many sites of $C_{16}O_4$ has been investigated. All the favorable Li adsorption sites can be seen in Fig. 5.3 and the corresponding binding (E_b) and adsorption (E_{ad}) energies and Bader charge (q) on Li are all listed in Table 5.1. The E_b and E_{ad} for Li adsorption on the UGO monolayer are defined by the equations

$$E_b = E(\text{UGO} + N\text{Li}) - NE(\text{Li})$$

and

$$E_{ad} = E(\text{UGO} + N\text{Li}) - E(\text{UGO}) - NE(\text{Li}_{iso})$$

, respectively. Here m$E(\text{UGO} + N\text{Li})$ and $E(\text{UGO})$ are the energies of the N Li-adsorbed UGO monolayer and the UGO monolayer without Li, $E(\text{Li})$ and $E(\text{Li}_{iso})$ are the energies of Li in the bulk body-centered cubic structure and isolated Li, respectively. The Li adsorption in the octagonal ring (O_{TC} and OC sites) is favorable while the Li adsorption in the hexagonal ring away from O is unstable and tends to migrate toward O. It employs that the O doping in graphene perturbs its charge distribution and makes it capable of storing Li. Since the charge disorder near to O is higher than away from it, Li adatoms have strong binding with the UGO monolayer at sites near to O than away from O. We found that the site denoted by OC is energetically the most stable site for Li adsorption and the one denoted by O_{TC} is the next most favorable site. The binding energies and Bader charge on Li shows that Li can be stored at the O_{BC} , O_B , and C_B sites as well but most probably the available OC and O_{TC} sites will be occupied first. It is noticed that the O_{TC} site becomes the most favorable site for Li adsorption on $C_{64}O_{16}$ (low capacity), which means that the favorable sites can be changed with changing the concentration of Li ions. The charge density difference

$$\Delta\rho = \rho_{\text{UGO}} + \text{Li} - \rho_{\text{UGO}} - \rho_{\text{Li}}$$

upon Li adsorption at different sites of UGO monolayer is shown in Fig. 5.3. The calculated $\Delta\rho$ shows that Li acquires positive charge upon adsorption on the UGO monolayer. This charge transfer causes strong binding between the adsorbed Li and the hosting UGO monolayer. Fig. 5.3(f) shows that the dipole flips if Li is adsorbed at the top of O (OT-site). The higher E_b in Table 5.1 for this site is thus partially due to the structural phase transitions of the UGO monolayer.

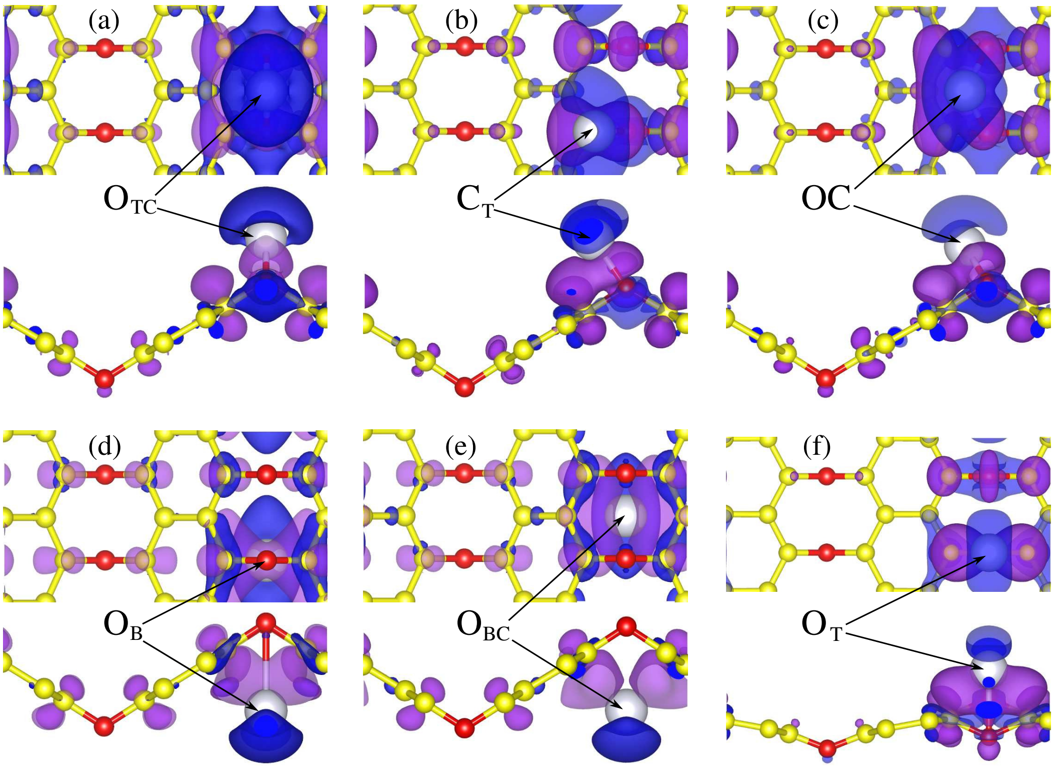

Figure 5.3: Top and side views for Li adsorption sites and charge density difference between the Li adsorbed UGO monolayer and the UGO monolayer and Li atoms at the adsorption sites (a) O_{TC}, (b) C_T, (c) OC, (d) O_B, (e) O_{BC}, and (f) O_T. The electron depletion upon Li adsorption is presented by blue color at the isosurface of -2×10^{-3} e/Å^3 while the electron accumulation is shown by purple color at the isosurface of 2×10^{-3} e/Å^3. The Li atom in the top and side views is indicated by arrows.

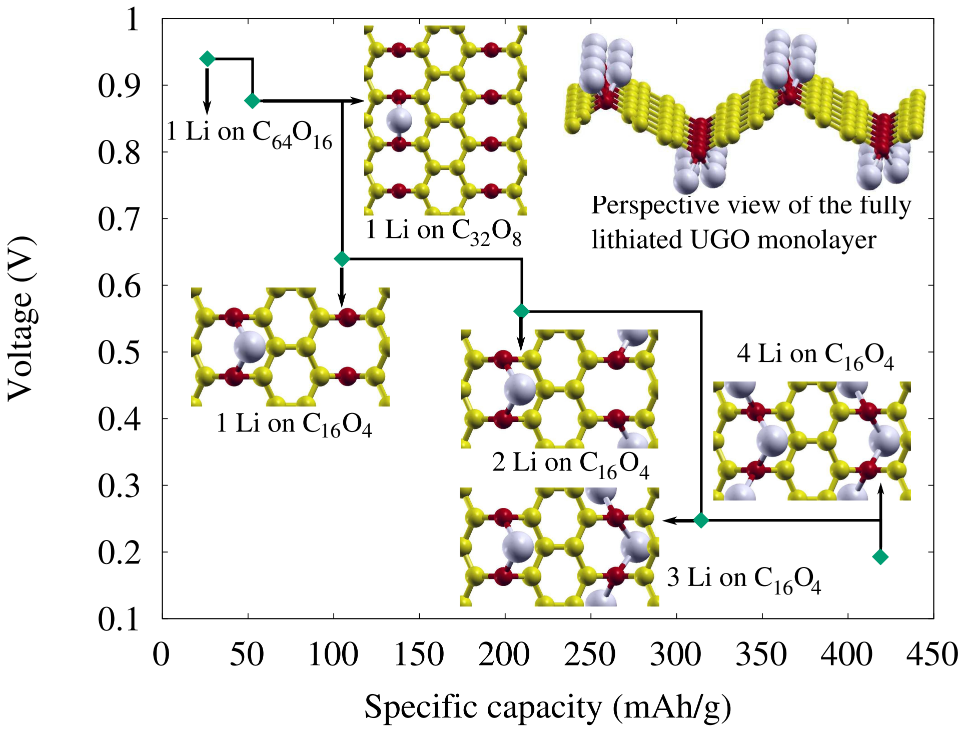

Figure 5.4: Open circuit lithiation voltage of the UGO monolayer. Insets show the top views of Li attachment with the UGO monolayer while one at the right top corner shows the perspective view for a fully lithiated UGO monolayer. The grey colored spheres are for Li adsorbed at the lower and top surfaces of the UGO monolayer.

Specific capacity (C), the amount of charge stored per unit mass of the anode is defined as

$$C = NZF/M_{C_{16}O_4}$$

(mAh/g), where N is the number of Li ions stored on the slab, Z the charge $C_{16}O_4$ on a Li-ion ($1|e|$), F the Faraday's constant (26801 mAh/mol), and $M_{C_{16}O_4}$ is the molar mass of the considered slab of the UGO monolayer. To find the maximum possible N, the most stable configuration for the Li adsorption for the intermediate capacities is searched out by considering all possible combinations and comparing the resulting E_b.

The Li adsorption configurations with lowest E_b are shown in the inset of Fig. 5.4. It shows the most possible mechanism of filling the UGO monolayer with Li. If one of the OC sites is already occupied by a Li adatom, another OC-site, farthest from the filled one becomes favorable for the adsorption of the next Li ion to reduce the Coulombic repulsion between the two positively charged Li adatoms. By this way four Li ions can be adsorbed on the $C_{16}O_4$ UGO monolayer with negative E_b to achieve the $Li_4C_{16}O_4$ composition. Although the OT C is the next favorable adsorption site after the OC-site, it becomes unfavorable when its nearest OC-site is already occupied. The E_b per Li ion increases with the increasing Li concentration due to the decreasing distance between the positively charged Li ions. Lowering the Li concentration over the UGO monolayer so that the repulsive forces between two Li ions can be neglected, saturates the E_b. Adsorption of the fifth Li on $C_{16}O_4$ results in positive E_b which means that the Li binding with the UGO monolayer is now weaker than that of the Li-Li metallic bond. Li storage capacity of the UGO monolayer calculated with the definition given above is 419 mAh/g. On single layer pristine graphene, Li clustering is favorable even for very low concentration of Li (LiC_{72}), which leads to the dendrite formation [162, 163, 182]. Thus the graphene can be made a high capacity anode by the induction of the positive charge regions via the periodic doping of O. Table 5.1: Binding (E_b) and adsorption (E_{ad}) energies and Bader charges (q) of a Li atom on $C_{16}O_4$ monolayer adsorbed at sites as shown in Fig. 5.3. The OC site is found to be energetically the most favorable one whereas the O_B and O_{BC} sites are equally favorable for Li adsorption.

5.3.3 Open circuit voltage

The reversible reaction for lithiation/delithiation of the UGO monolayer can be written as

$$\mathrm{Li}_{x1}\mathrm{UGO} \rightleftharpoons \mathrm{Li}_{x2}\mathrm{UGO} + (x1{-}x2)\,\overset{+}{\mathrm{Li}} + (x1{-}x2)\,\overset{-}{e}$$

Neglecting the pressure, temperature, and entropy effects, the half cell voltage between two stable lithiated ($x1$) and delithiated ($x2$) phases of the UGO monolayer can be approximated as

$$V(x1,x2) = \{E(\mathrm{Li}_{x1}\mathrm{UGO}) - E(\mathrm{Li}_{x2}\mathrm{UGO}) - (x1-x2)E(\mathrm{Li})\}/e(x1-x2)$$

Here $E(Li_{x1}UGO)$ and $E(Li_{x2}UGO)$ are the energies of the lithiated and delithiated stable phases of the UGO monolayer. As aforementioned for calculating E_b we first search for the most stable Li adsorption configuration over the UGO monolayer at intermediate capacities and then calculate the voltage by using the formula given above. The voltage profile of the UGO monolayer as a function of Li storage capacity is plotted in Fig. 5.4. Open circuit voltage of the UGO monolayer drops with increasing Li concentration similar to that of graphite and bco-C_{16} systems [101, 161]. Although the theoretical voltage profile gives information of the intermediate stable phases only but such results have been found in good agreement with the experiments [183–185]. In order to have a high voltage cell, a low half cell voltage from the anode and a high half cell voltage from the cathode of a LIB are required. The open circuit voltage of the UGO monolayer is in the range 0.94 to 0.19 V, which is within the voltage range of a typical anode material for LIBs.

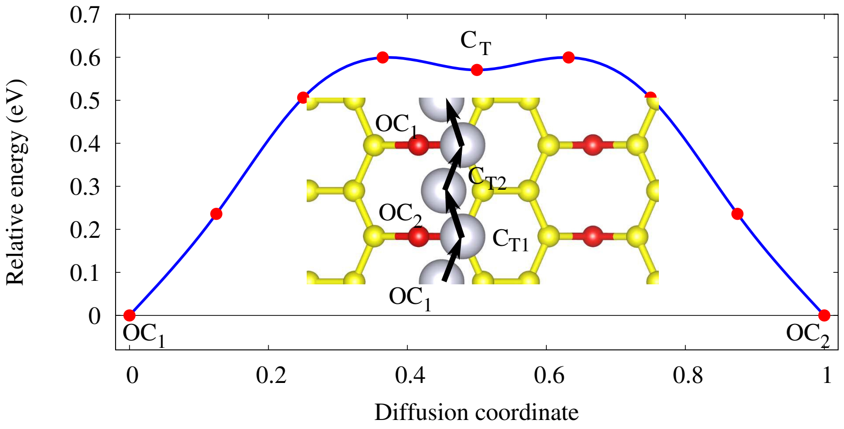

Figure 5.5: Minimum energy path for Li diffusion on the UGO monolayer, from a stable OC-site to a nearby OC-site via a metastable C_T-site. The Li diffusion trajectory along the minimum energy path is shown.

5.3.4 Diffusion

Fast Li diffusion in electrodes and electrolytes is highly desired so that the battery can be charged in short time and can deliver high power. The diffusion coefficient (D) of a Li ion can be estimated with the formula given by Arrhenius:

$$D \propto e^{-E_a/K_B T}$$

where E_a is the activation energy barrier, K_B is the Boltzmann constant, and T is the temperature. In the above relation, if E_a is known then D can be estimated. E_a depends somehow upon the difference in the binding strength of the Li adatom at the stable and intermediate positions. If the difference of the E_b at the intermediate and initial position is large, E_a will result in high value and so a lower D value will be expected. There can be many paths for the diffusion of a Li ion from one stable site to another stable site, but it is obvious that Li will diffuse along the one with lowest E_a. To find E_a along the minimum energy path, the NEB method is valuable at low concentrations of Li. As in the UGO monolayer case the OC-site is energetically the most stable site for Li adsorption, we need to calculate the minimum energy path for the diffusion of a Li ion from a OC site (OC_1) to its nearest neighboring OC site (OC_2) via the intermediate metastable C_T site.

From our previous discussion about the E_b values in Table 5.1 and the charge distribution shown in Fig. 5.3, it is clear that the minimum energy path for Li diffusion from the OC_1-site to the OC_2-site is through the C_T site between the two OC sites. As we already have explained, the Li adsorption away from O is unfavorable and the Li adatom migrates towards the O when it is relaxed. Since Li has high energy at positions away from O, of course a path along the

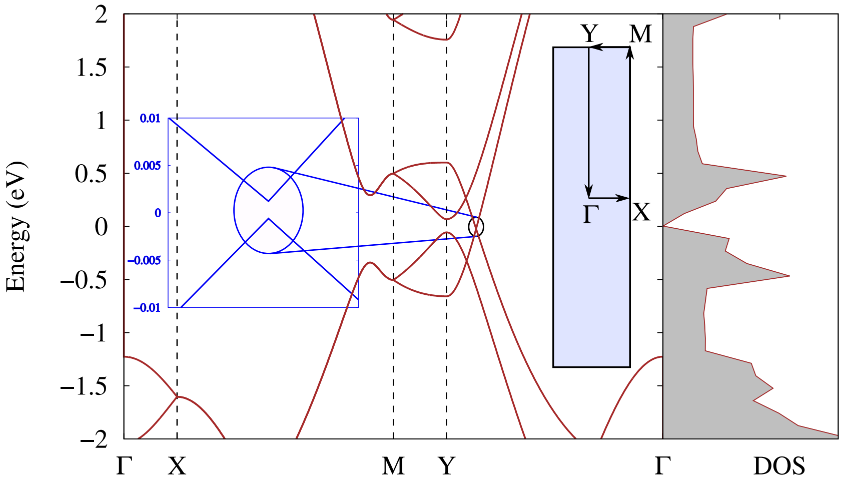

Figure 5.6: Electronic band structure and total density of states of the UGO monolayer calculated with the PBE functional. The Dirac cone between the Y and Γ points shows that this material can have high electron and hole mobilities. The band gap of the UGO monolayer calculated with the HSE06 functional is 0.6 eV. Band structure near the Dirac cone is magnified in the inset at left.

zigzag direction can not be a minimum energy path. Fig. 5.5 plots E_{ad} at the intermediate points relative to that at the most stable OC site, and the intermediate images are obtained from the NEB calculations, starting with the initial images given by the linear interpolation between the OC and C_T sites. The inset of Fig. 5.5 shows a top view of the trajectory of a Li ion along the minimum energy path. The E_a for Li diffusion along this path is about 0.58 eV at a capacity of 100 mAh/g, which is larger than that on pristine graphene. This is because the electron deficient regions produced by O are localized.The Li has a strong binding at those positions while it loses binding when Li goes away from the localized path. Similar results can be seen for graphene, phosphorene, silicene, and monolayer MoS_2 [85, 143, 186–189]. The reported E_a of the Li diffusion on pristine graphene along the minimum energy path is about 0.3 eV which increases to 0.8 eV for monovacancy defect [143]. Similarly, E_a of the Li diffusion on the pristine phosphorene is 0.08 eV, and the activation energy increases up to 0.7 eV in the case of intrinsic defects [186, 187]. The increase in E_a of metal ions with the intrinsic or artificial defects is common which is due to the localization of electron deficient regions. The E_a for Li diffusion on the UGO monolayer is comparable with that reported for other 2D anode materials [168, 170].

5.3.5 Electronic properties

The Li ions in a charged battery flow from the anode to the cathode via electrolyte and the electrons donated by the Li are driven through external circuit to gain power. So, high electronic conductivity as well as fast Li shuttling at the electrodes are required for the fast charge/discharge processes. To investigate the electronic structural properties of the UGO monolayer, its band structure and density of states are calculated as shown in Fig. 5.6. The graphene-like Dirac cone is observed between the Y and Γ-points of the band structure, which shows that the UGO monolayer may have electron and hole transport properties similar to graphene [154]. Doing the same calculations with the HSE06 functional, a band gap of 0.6 eV is noticed. This is because the PBE functional underestimates the band gap. Thus the UGO monolayer, having high electron and hole mobilities with a small band gap can be one of the most required materials for manufacturing nanodevices. As expected, with the adsorption of low capacity Li, the band gap in the UGO monolayer disappears and becomes metallic as highly required in electrodes of LIBs. Some of the well known 2D anode materials have high band gaps, as for example SnS_2, MoS_2, and phosphorene where the full recovery of Li ions will not be possible [110, 117, 158]. Thus the very small band gap of the UGO monolayer makes it a promising 2D anode material.

5.4 Conclusions

We presented a systematic study on the structure and stability of a crystalline UGO monolayer ($C_{16}O_4$) and its feasibility for Li adsorption and diffusion. The O injectedgraphene produces a dipole moment. To know the dipole ordering, four different dipole patterns for the UGO monolayer are considered. The energy calculations show that the antiferroelectric orderings of dipoles are more favorable than the ferroelectric one. The MLWF calculations confirm that the zigzag structure of the UGO monolayer results from the interaction between O lone pairs and C-O bond pairs. The electronic band structurethe UGO monolayer has the Dirac cone similar to graphene but it is semiconductor withsmall band gap of 0.6 eV. Thus this material can have astonishing electron and hole transport properties. Since the lone-pair electrons of O produce bond tilting with an induced out-of- plane dipole moment, electron deficient regions are formed near O atoms which enhances the Li adsorption capacity of the UGO monolayer. The calculated Li adsorption capacity of the UGO monolayer thus reaches to 419 mAh/g. The lithiation open circuit voltagethe UGO monolayer ranges from 0.94 V to 0.19 V, a typical anodic voltage range for LIB anode materials. The low band gap of the UGO monolayer and excess electron donated by adsorbed Li makes it metallic as required for LIBs. The Li diffusion barrier is 0.60 eV, almost double of pristine graphene, is due to the localization of the positively charged regions in the UGO monolayer.

Chapter 6

Polarization in the MX monolayers

6.1 Introduction

Isolation of graphene, a freestanding single-atom-thick allotrope of carbon, and the new physics behind its un- usual electronic properties opened doors to search for other graphene-like two-dimensional materials. Thousands of monolayers have been found in different geometries with the help of computer simulations, and many of them have been recognized and characterized experimentally as well. Besides the exciting physics of topological insulators, spin-valleys, Rashba and Hall effects, these materials have shown potential for the device applications for nanoscale energy conversion, storage, and designing nanoscale electronic devices. Switchable out-of-plane polarization is one of the emerging features of these materials [1–3, 40, 158, 190–194].

From the medical point of view, wireless nanoscale injectable, digestible, and implantable devices are required for the physiological monitoring of the sensitive parts of the human body [195]. Designing electronic circuits for these purposes requires nanoscale sensors. Low-dimensional switchable ferroelectrics and piezoelectrics could be used as sensors, actuators, and non-volatile memory storage devices for nanoscale electronics. Ferroelectricity in low-dimensional materials is, however, hampered by the depolarizing field produced by the uncompensated surface charge [**?**]. Density functional theory calculations have proved that polarization can be induced in the transition metal dichalcogenide (TMD) and group-IV transition metal monochalcogenide monolayers by applying a uniaxial strain to break and reconstruct the inversion symmetry [62, 196, 197]. Experimentally a high piezoelectric in-plane polarization in monolayer MoS_2 has been reported, but for device applications, it may not be as beneficial as out-of-plane polarization can be [198–201]. Computational studies have modeled new two-dimensional materials with high out-of-plane polarization and piezoelectric coefficients [57, 202–204].

Based on energy optimization of the geometry and stable phonon modes Cahangirov *et al* [19]. claimed that silicon and germanium could have two and one dimensional (2D and 1D) analogs (silicene and germanene). As unlike graphite or TMDs the bulk Si and Ge did not possess layered structures, it was tough to believe in the possible existence of silicene and germanene. Three years later, silicene was successfully synthesized by Patrick *et al* [20]. and two years after silicene was synthesized, germanene was also synthesized by Daivila *et al* [205]. Similar is the case with boron (B). Theoretically, it can have a stable monolayer (borophene) which has been confirmed by Andrew *et al* [34]. All these examples show the significance of theoretical predictions about the new 2D structures. Inspired by the theoretical predictions of silicene, germanene, and borophene and later their experimental confirmation, we explore four new binary monolayers, named MoC, WC, WS, and WSe by using density functional theory calculations. The phonon dispersion modes for these monolayers are stable in the buckled hexagonal structure whereas unstable in the flat one. In-plane elastic stiffnesses of these monolayers are comparable with those of monolayer MoS_2. As the two building atoms of these monolayers belong to two different groups of the periodic table, a difference in their electronegativity results in electric dipoles. The parallel alignment of the out-of-plane components of these dipoles results in high spontaneous polarization. The polarization reversal for these monolayers is possible by folding their bonds with switching barriers ranging from 0.55 to 2.70 eV. Change in the out-of-plane polarization of these monolayers is independent of the direction of the applied stress and linear under uniaxial and homogeneous biaxial strains in the low strain range. A uniaxial strain along the armchair direction results in high in-plane piezoelectric coefficients (e_{22}), and the e_{22} values for monolayer MoC and WC are three times larger than that of monolayer MoS_2. Furthermore, the electronic band structures show that these monolayers are semiconducting and can have many device applications in nanoelectronics.

6.2 Computational details

Our results are based on the density functional theory calculations, implemented in the Vienna Ab-initio Simulation Package (VASP) [100]. The generalized gradient approximation (GGA) with the parametrization scheme of Perdew-Burke-Ernzerhof (PBE) [70] is used for the electron-electron exchange-correlation process. The electron-ion interactions are processed by the projector augmented wave (PAW) method. The valence electron configurations used in our calculations are as Mo ($5s^1$, $5d^4$), W ($6s^2$, $5d^4$), S ($3s^2$, $3p^4$), Se ($4s^2$, $4p^4$), and C ($2s^2$, $2p^2$). The cutoff energy of 600 eV is considered for the plane-wave expansion of the electronic eigenfunctions. The Monkhorst-Pack k-mesh of $25\times25\times1$ is used and the

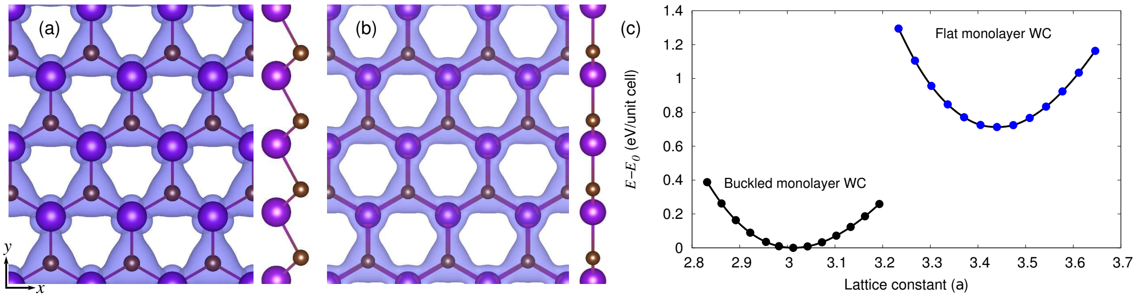

Figure 6.1: The top and side views of (a) buckled and (b) flat geometries of monolayer WC and (c) the top view of the electronic charge distribution (light green color shows electron density at the isosurface of 8×10^{-2} e/Å^{-3}) in the buckled monolayer WC. The dark pink and brown colored spheres are for W and C atoms respectively.

structures are optimized until the largest Hellmann-Feynman force component on each atom is less than 0.001 eV/Å. The electronic band structure and density of states are performed with PBE and HSE06 functionals. The phonon spectra are carried out using the finite displacement method implemented in the Phonopy code [148]. The finite difference method is used to calculate elastic constants [206].

6.3 Results and discussion

6.3.1 Structure stability

Based on structure optimization and lattice vibrations we have modeled four new MX(M = Mo/W, X = C/S,Se) monolayers. Two different geometries (buckled hexagonal and flat hexagonal) for these monolayers are depicted in Fig. 6.1(a, b). In our calculations, we consider a diatomic hexagonal unit cell of the MX monolayers with the zigzag direction along the x-axis and the armchair direction along the y-axis. Energetics of these monolayers show that the buckled trigonal geometries [space group $P3m1$ (156)] are more prominent than the flat hexagonal [$P\bar{6}m2$ (187)] ones. As an example, the energy versus lattice constant curve for buckled and flat structures of monolayer WC is shown in Fig. 6.1.

In these structures, an M atom is three-fold coordinated with X atoms. Similarly, each X atom also has a three-fold coordination with M atoms. The flat geometries of these monolayers resemble the h-BN monolayer. In the buckled geometry the alternating M and X atoms belong to two different parallel planes. These structures can be easily understood from their top and side views as shown in Fig. 6.1(a, b). The electron density for monolayer WC in the buckled structure as depicted in Fig. 6.1(a) is higher at the carbon than at the W, which is due to the difference in their electronegativity. The difference in electronic density at M and X atoms

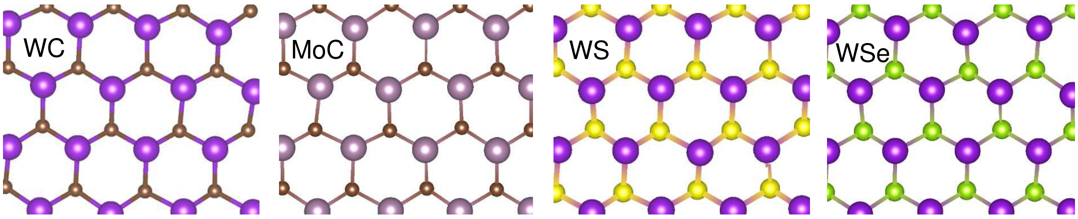

Figure 6.2: Molecular dynamics simulations of the MX monolayers

results in a local electric dipole moment. As shown in Fig. 6.3, we considered other possible paraelectric and antiferroelectric allotropes for these monolayers, but they were dynamically unstable.

Energy difference per unit cell between the buckled and flat structures, lattice parameters, vertical distance between the M and X atoms, energy gap, Bader charges on M and X atoms, spontaneous out-of-plane polarization, and piezoelectric coefficients for all the four monolayers are listed in Table 6.1. The buckled structures are always more stable than their flat allotropes.

Next, using ab-initio molecular dynamics, we have calculated the temperature effects on the structural stability of the buckled phase of MX monolayers. It is found that the atoms of these monolayers oscillate around their lattice sites and reconstruct the initial geometry. As no bond breaking or phase transformation is seen, these monolayers have stable structures at room temperature as well. Top view of a portion of the snapshots of the MX monolayers at room temperature after running 1000 steps (time step 5 ps) are shown in Fig. 6.2. After confirming energetic and thermal stability, phonon spectra of the MX monolayers are calculated (shown in Fig. 6.4) to verify their dynamic stability. The phonon band structures for buckled monolayers MoC and WC, and WS and WSe are looking similar due to the same-group atoms and similar structures. However, the maximum frequency of WSe is lower compared to WS monolayer because of the heavier Se than the S. The absence of soft modes in the first Brillouin zones plotted through high symmetry points for the buckled hexagonal structures is a strong evidence for their dynamic stability while the phonon dispersions for the higher-energy intermediate phase (flat phase) yield negative frequencies. Similar to h-BN and other binary monolayers these structures have six modes [50, 207–210].

First three modes with comparatively lower frequencies are the acoustic modes while the other three with higher frequencies are the optical modes. Each mode is due to a specific vibration of the lattice. The acoustic modes have three branches, the transverse (TA), longitudinal (LA), and out-of-plane (ZA). The quadratic nature of the ZA branch is a characteristic of the suspended monolayers, argued as a consequence of the point group symmetry [25, 211]. The LA and T A branches are linear near to the Γ point. Our results are con-

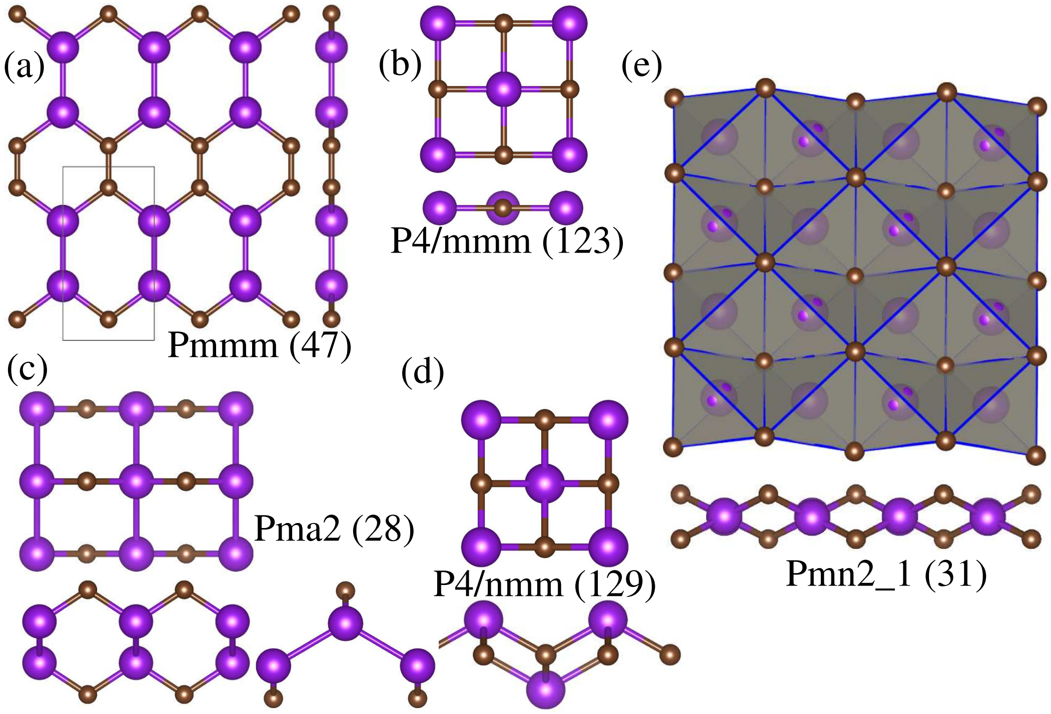

Figure 6.3: Paraelectric and antiferroelectric structures for monolayer WC.

sistent with the previously reported phonon dispersion modes for other stable monolayers [25, 50, 211–213]. In order to examine the mechanical stability of the *MX* monolayers, we first calculated the elastic constants for monolayer MoS_2 and compared our results with references [196, 214]. After confirmation of our method, in-plane elastic constants (C_{11}, C_{12} Young's moduli ($Y_{22} = (C_{11}^2 - C_{12}^2)/C_{11}$), and Poisson's ratios ($\nu = C_{12}/C_{11}$) are calculated and listed in Table 6.2. It shows that stiffness C_{11} of the W-contained monolayers is even higher than monolayer MoS_2 whereas that of monolayer MoC is less than monolayer MoS_2. The trends found in the elastic constants C_{11} and Y are similar to those found in monolayer TMDs [196, 214].

6.3.2 Spontaneous Polarization and Piezoelectricity

While so far it is proved computationally that synthesis of the buckled hexagonal *MX* monolayers is possible, a unique feature of these monolayers, the spontaneous out-of-plane polarization, is to be explained here. As aforementioned, the polarization of polar films decreases if their thickness is reduced below 50 Ådue to the depolarizing field produced by the uncompensated surface charges to make it difficult to synthesize 2D ferroelectric materials. Even though many results are reported on induced in-plane polarization, there are only a few reports on the

Table 6.1: Energy of buckled structures relative to their flat allotropes per unit cell (ΔE in eV), lattice constant (a in Å), bond distances (M-X in Å) and vertical distances (d_z in Å) between M and X atoms in the buckled structures, band gap calculated with the HSE06 functional (E_g in eV), Bader charges on M and X atoms (q in e), spontaneous polarization (P_s in pC/m), polarization switching barrier (E_b in eV), and piezoelectric stress coefficients ($e_{31} = e_{32}$ and $e_{22} = e_{12}$ in 10^{-10} C/m) for MX monolayers

	ΔE	a	M-X	d_z	E_g	q on M,X	P_s	E_b (eV)	e_{31}	e_{22}
MoC	-0.23	3.01	1.97	0.90	1.33	0.83, -0.83	14.97	0.55	0.51	10.00
WC	-0.71	3.01	1.98	0.94	1.81	0.83, -0.83	11.70	0.88	0.39	10.02
WS	-2.02	2.96	2.35	1.62	0.68	0.49, -0.49	3.09	2.56	0.45	4.68
WSe	-2.15	3.04	2.48	1.74	0.67	0.34, -0.37	4.51	2.70	0.55	4.92

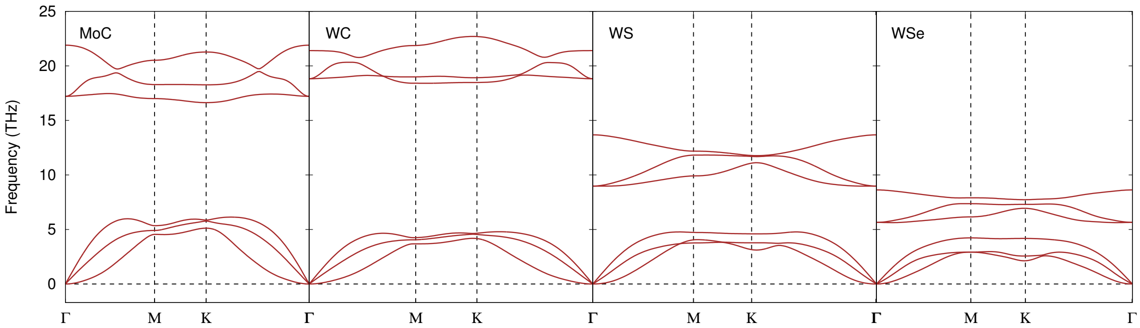

Figure 6.4: Stable phonon dispersion modes for the buckled hexagonal *MX* monolayers

out-of-plane polarization in monolayers [57, 62, 178, 196, 197, 202].

As all the MX monolayers presented here are a combination of two different-kind atoms with different electronegativity, the shared electron pair is attracted toward one kind of atoms more than the other as shown in Fig. 6.4(c). This charge imbalance results in a local electric dipole (p), where the in-plane components p_x and p_y of p cancel out, but the out-of-plane component (p_z) remains due to the broken inversion symmetry. We compute the non-zero dipole moment p_z per unit cell from the summation of the ionic contribution and the integration of electronic charge distributions [215]:

$$p_z = \sum_i Z_i R_{i,z} - e \int_{\Omega} z n_e(x,y,z) dxdydz,$$

where Zi is the ionic charge and $R_{i,z}$ is the z position of the i-th ion in the unit cell Ω and e is the charge on a proton, n_e (x, y, z) is the valence shell electron density. Due to the symmetry, the magnitude of spontaneous polarization is $P_s = p_z/A$, where A is the area of the monolayer in the unit cell. The P_s values for unstrained MX monolayers are listed in Table 6.1, and they are comparable to the previously reported values for some other monolayers [216].

Table 6.2: In-plane elastic constants (C_{11}, C_{12}), Young's modulus (Y), and Poisson's ratio (ν) calculated for MX monolayers.

Composition	C_{11} (N/m)	C_{12} (N/m)	Y (N/m)	ν
MoS_2 [214]	132.7	33.0	124.5	0.25
MoS_2 (this study)	132.5	32.8	124.4	0.24
MoC	129.2	42.9	115.0	0.33
WC	142.8	39.1	132.1	0.27
WS	154.4	35.3	146.3	0.22
WSe	145.3	26.8	140.3	0.18

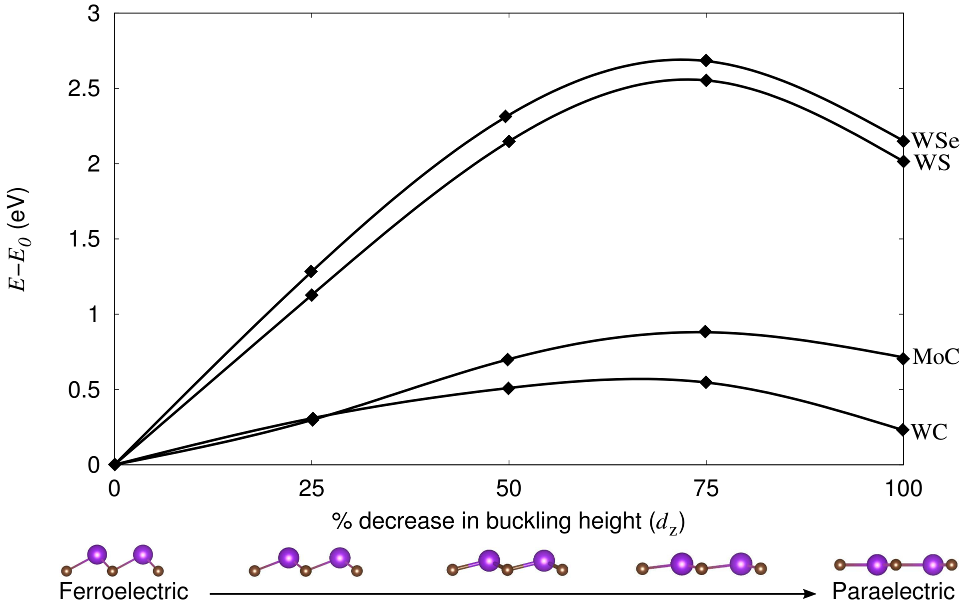

Figure 6.5: Energy barriers for ferroelectric-to-paraelectric phase transition for the MX monolayers. The schematic figures of the atomic configurations at each image are shown with purple circles for Mo and W and brown circles for C, S, and Se.

Polarization reversal of the out-of-plane component of these monolayers is possible by folding the direction of the $M-X$ bonds. Fig. 6.5 shows the variation in energy of the MX monolayers by structural transformations from the buckled hexagonal (ferroelectric) to the flat hexagonal (paraelectric). The vertical distance between the M and X atomic planes is gradually decreased and the z coordinates are fixed and lattice parameters a and b are optimized. Fig. 6.5 depicts that the buckled and flat structures of the MX monolayers are lower in energy than the intermediate states whereas the buckled structures are in the lowest energy. The energy barriers for the polarization reversal (E_b) of these monolayers are listed in Table 6.1.

The variation in P_z as a function of in-plane uniaxial strain is presented in Fig. 6.6. The ΔP_z is almost linear for all these monolayers in the strain range -0.02 to 0.02. The ΔP_z by

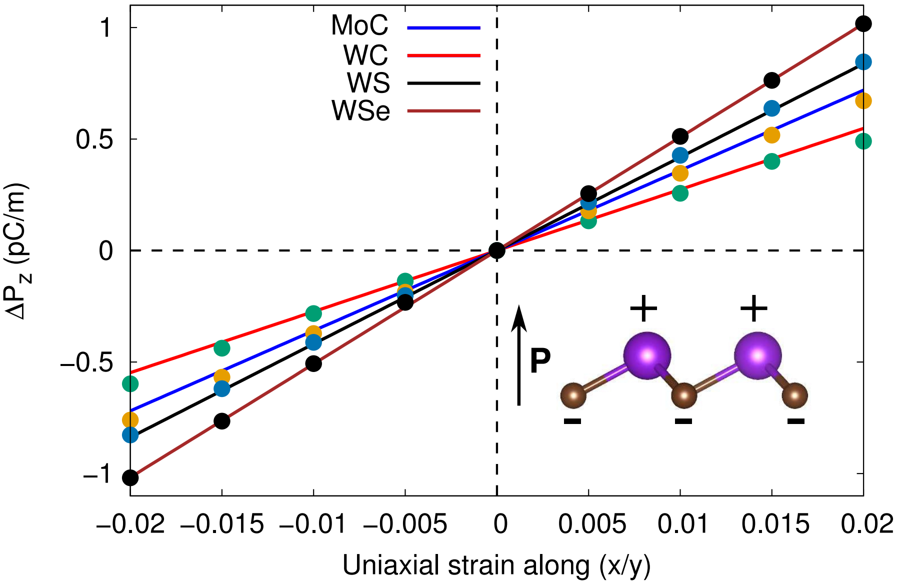

Figure 6.6: The change in polarization (P_z) is linear under uniaxial strain along x or y directions. The inset shows the direction of the polarization for the *MX* monolayers.

a strain along the x-direction is the same as that by a strain along the y-direction due to the symmetry of these structures. The piezoelectric stress constant [217]

$$e_{ij}(=e_{ilm}) = \frac{\partial P_i}{\partial \varepsilon_{j(lm)}} + \delta_{lm}P_i - \delta_{il}P_m,$$

where $i,l,m = 1,2,3$ stands for x, y, and z directions and j is the strain in Voigt notation. From this equation, the out-of-plane piezoelectric stress coefficient e_{31} becomes:

$$e_{31} = \frac{\partial P_3}{\partial \varepsilon_1} + P_3$$

and the in-plane piezoelectric stress coefficient e_{22} becomes:

$$e_{22} = \frac{\partial P_2}{\partial \varepsilon_2}$$

. Slopes of the lines shown in Fig. 6.6 present the piezoelectric stress coefficients $e_{31} = e_{32}$ and the computed e_{31} for all the monolayers are listed in Table 6.1.

An in-plane uniaxial strain can produce symmetry distortion in all the *MX* monolayers to induce in-plane polarization. As all these monolayers have three mirror planes along the armchair directions, a uniaxial strain applied along the zigzag direction cannot break one of the three mirror planes, which makes piezoelectric coefficient $e_{11} = e_{21}$ to zero. Since there is no mirror plane along the zigzag direction, a strain along the armchair direction results in a

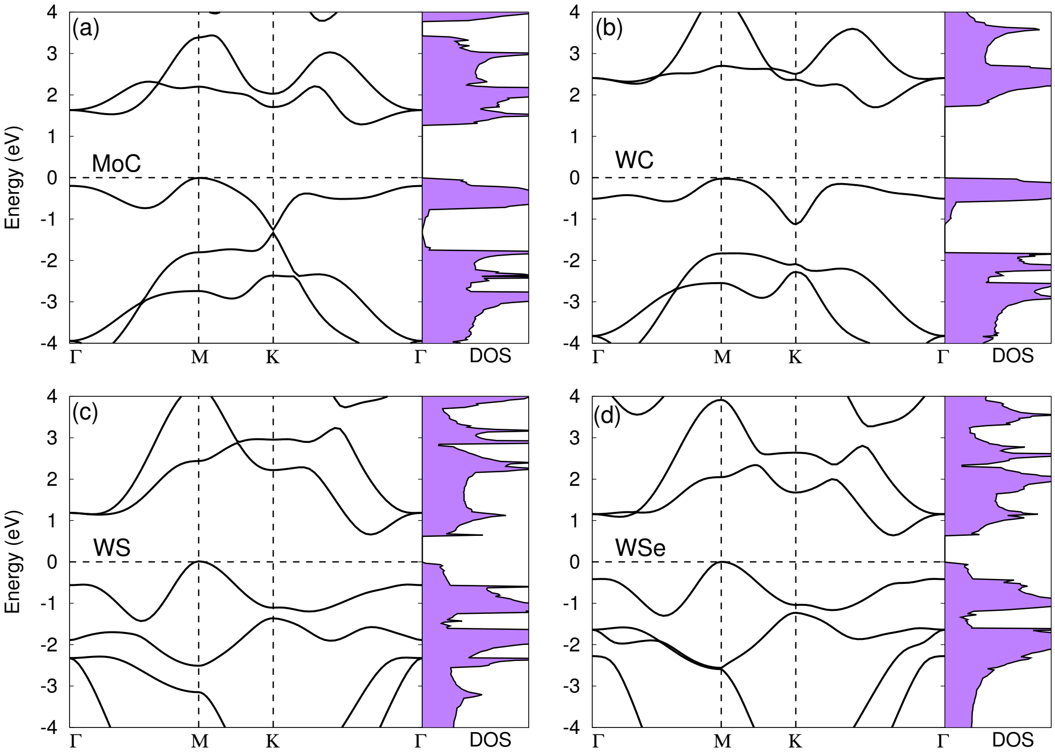

Figure 6.7: Band structures and total density-of-states for monolayer (a) MoC, (b) WC, (c) WS, and (d) WSe. Fermi-level is set to the top of the valence band. The band structures of monolayer MoC and WC resemble Mexican-hat band dispersions at the *K* symmetry point.

high piezoelectric coefficient ($e_{22} = -e_{12} = 0$). For calculations of the in-plane piezoelectric coefficients, we have used density functional perturbation theory (DFPT). The method is first tried on monolayer MoS_2 and our calculated e_{22}(=3.05, 3.06 for clamped and relaxed ions) is found in good agreement with the available theoretical and experimental reports [196, 198]. After the method confirmation, DFPT was employed on the *MX* monolayers. The piezoelectric coefficients of the *MX* monolayers are tabulated in Table 6.1. The in-plane piezoelectric coefficients of the MoC and WC monolayers are about three times larger than those of the 2H-TMDs (MX_2= Mo/W, and X = S/Se/Te) monolayers, five times larger than the group-III monochalcogenides (GaS, GaSe, and InS) while comparable to that of group-IV monochalcogenides (SnS, SnSe, GeS, and GeSe) [62, 63, 196, 198].

To demonstrate the electronic structures of these monolayers, their electronic band structures and total density-of-states are presented in Fig. 6.7. The band structures and total density-of-states obtained with the HSE06 functional are shown in Fig. 6.7. Band structures calculated for the *MX* monolayers with PBE and HSE06 functionals are similar, but as usual, the HSE06 functional results in higher bandgaps compared to those from the PBE functional. The HSE06 bandgaps of all these monolayers are listed in Table 6.1. Band gaps of these monolayers range from 0.67 to 1.81 eV, which makes them useful for manufacturing nanodevices. A Mexican-hat like band dispersion is seen in the valence band nearest to the Fermi level of monolayer MoC and WC at the K symmetry point. Ferroic (Ferromagnetic and Ferroelastic) properties of such materials can be easily tuned by controlling the hole doping [38, 218, 219]. Since all these monolayers include heavy atoms like W and Mo, high spin-orbit coupling is expected. As the valence band maxima of all these monolayers is at the K symmetry point, these monolayers can also be studied for spin-valley properties [216].

6.4 Conclusions

Using density functional theory based calculations four new monolayers WC, MoC, WS, and WSe have been predicted to have buckled hexagonal geometry. The stability of these monolayers is evident from energy optimization and stable lattice vibrations. These monolayers show high in-plane elastic stiffnesses. A high spontaneous out-of-plane polarization is observed due to their noncentrosymmetric buckled geometries and a large difference in electronegativity of the building atoms. The out-of-plane polarization is seen to change isotropically with the applied uniaxial and biaxial strain. Due to the low energy difference between the buckled and flat phases, dipoles of these monolayers may be easily switchable. Although there is no in-plane component of the spontaneous polarization, the symmetry distortion via uniaxial strain induces a high in-plane polarization in these monolayers. The piezoelectric coefficients (e_{22}) for monolayer MoC and WC are found to be three times larger than that of the monolayer MoS_2.

Chapter 7

SnS_2/graphene as anode material

7.1 Introduction

To overcome the challenges faced in energy storage and global warming due to the large-scale use of burning fuels, rechargeable Li-ion batteries (LIBs) have been playing an important role as an efficient electrochemical energy storage system for more than two decades. They have applications in wireless technologies like mobile phones, laptops, cameras, and now in rechargeable vehicles as well. A low cost, non-toxic and stationary rechargeable battery is a viable solution to the fluctuations in the demand and production of sustainable wind and solar energy. The high energy density of LIBs has made them popular in portable devices. However, the high cost, scarcity of Li in the earth's crust and the increasing demand for batteries require some cheap and abundant alternatives to toxic LIBs. Non-toxic, abundant, and cheap sodium(Na), having most of the chemical properties of Li, can partially replace LIBs, but finding efficient electrode materials and electrolytes for Na ion batteries (NIBs) is still a challenging task [76, 77, 83, 84, 220–222].

Graphite, the commonly used commercial anode material for LIBs, fails to intercalate an appreciable amount of Na. This problem is associated with the comparatively high redox potential and unfavorable thermodynamics of Na insertion in graphite [223, 224]. On the other hand, disordered and porous carbon based materials have shown higher capacity for Na storage [84]. One of the most possible reasons for the poor intercalation of Na in graphite is the comparatively large ionic size of Na because expanded graphite with an interlayer distance of 4.3 Å has been reported with a reversible capacity of 284 mAh/g [86].

Pristine graphene is unfavorable for high density storage of Na while defective graphene has varying capacity depending on the concentration and type of defect. For divacancy defects a maximum capacity of 1450 mAh/g has been reported while 1071 mAh/g for Stone–Wales defects [80]. Boron substituted graphene (BC_3) has a capacity of sodiation 2.04 times greater than that of graphite for LIBs, with an average half-cell voltage of 0.44 V. But the defects in graphene decrease its electronic conductivity [95, 98].

Layered materials such as phosphorene, MoS_2, GeS, CrS_2, VS_2, TiS_2, ZrS_2, $CoTe_2$, NbS_2, and $NiTe_2$ [90, 97, 115, 225, 226] have been studied for NIB anodes, using first principles calculations. These studies reveal high charge storage capacity and fast diffusion of the Li/Na ions along the minimum energy path. But the electronic conductivity and mechanical strength of these materials should be upgraded. Several experimental and theoretical reports on graphene and reduced graphene oxide heterostructures with other layered materials for LIB and NIB anodes showed a high charge storage capacity, low activation barrier, high electrical conductivity, high mechanical strength and long cycle life [117, 227–230]. Sn and Sn derivatives are ideal for high density Li and Na storage but large volume variations are always reported during the intercalation and deintercalation of these materials, which negatively affect the performance of the anode in terms of losing contact with the current collector and reduced cycle life of the anode. This volume variation has been reported in intercalated Si as well [87, 137, 138, 140, 231, 232].

Here we study the SnS_2 monolayer as a NIB anode material because Sn based layered materials are very active to Na adsorption; so a high Na storage capacity is expected. We highlight the problem of large area expansion and the lack of conductive paths in SnS_2. Graphene has high electrical conductivity and mechanical strength but pristine graphene is not favorable for Na storage. To suppress the variations in the area and provide conductive paths, we make SnS_2 and graphene heterostructure to utilize the unique properties of the two different materials and model an ideal anode.

7.2 Computational methods

All calculations were carried out by using the Vienna Ab initio Simulation Package (VASP) with the projector augmented wave (PAW) and the Perdew–Burke–Ernzerhof (PBE) form of the generalized gradient approximation (GGA) for the electron–electron exchange-correlation [69, 70, 100, 101]. Cutoff energies of 350 and 600 eV were chosen, for the plane-wave expansion of the electronic eigenfunctions, for the SnS_2 monolayer and the SnS_2/graphene heterostructure, respectively. The force criterion for the structural relaxation was chosen as 0.01 eV/Å. To avoid the self-interaction in the monolayer case, a vacuum of 25 Å was used between the periodic layers. Γ-point sampling was used with $7\times7\times1$ and $5\times5\times1$ meshes of k-points for the integration of the Brillouin zone for the SnS_2 monolayer and the SnS_2/graphene heterostructure, respectively. A $3\times3\times1$ supercell (with nine Sn and eighteen S atoms) was considered for the pristine SnS_2 monolayer case. In order to minimize the lattice mismatch for the SnS_2/graphene heterostructure, a 2×2×1 supercell of SnS_2 was combined with a 3×3×1 supercell of graphene, which contained 4 atoms of Sn, 8 atoms of S, and 18 atoms of C. Thus a mismatch of 0.215% occurred. In the heterostructure case, weak van der Waals interactions were considered. To find out the minimum energy path and the migration energy barrier for the diffusion of Na ions, the nudged elastic band (NEB) [233, 234] method was employed. The NEB method is one of the reliable tools to find out the minimum energy path (MEP) and the activation energy barrier between two stable states. We performed it by the linear interpolation of five images between the initial and final positions.

7.3 Results and discussion

7.3.1 1T SnS_2 monolayer

Among the two possible phases (1T and 2H) of the monolayer SnS_2, we select the 1T structure for our calculations because it is energetically more stable than the 2H structure [235]. The top and the side views of a portion of the 1T SnS_2 monolayer are shown in Fig. 7.1. The 1T structured SnS_2 monolayer has three trigonal subplanes of atoms. A Sn subplane is sandwiched by two S subplanes. The monolayer 1T structured SnS_2 has the space group $P\bar{3}m1$ with ABC stacking of subplanes. The calculated Sn–S bond length (2.596 Å) and the lattice constants (a=b=3.69 Å) for SnS_2 agree well with the reported values (Sn-S=2.59 Å and a=b=3.68 Å) [235]. Here two positions for the adsorption of Na are extremely interesting. One is the hollow position exactly above the S from the bottom layer. We will call this site the H-site throughout this discussion. The S atom from the bottom layer, the center of the equilateral triangle made by the Sn atoms, the center of the equilateral triangle made by the S atoms from the top layer, and the H-site are collinear, as shown in the left panel of Fig. 7.1. The second favorable position is exactly above the Sn atom, occupying the space above the center of the equilateral triangle made by the top layer S atoms. We call this site the T-site. The center of the equilateral triangle made by the S atoms from the bottom layer, the Sn atom, the center of the equilateral triangle made by the S atoms from the top layer, and the T-site are collinear, as shown in the middle panel of Fig. 7.1.

7.3.2 Na adsorption at the SnS_2 surface

Three different positions are considered for the adsorption of Na on the SnS_2 monolayer, the H-site, the T-site, and the position above the S atom from the top layer. However, it is found that the binding energy of the Na adatom above the top S atom is about 0.60 eV higher than that of the H- and T-sites, that is why the adsorption of Na above the top S atom is ignored.

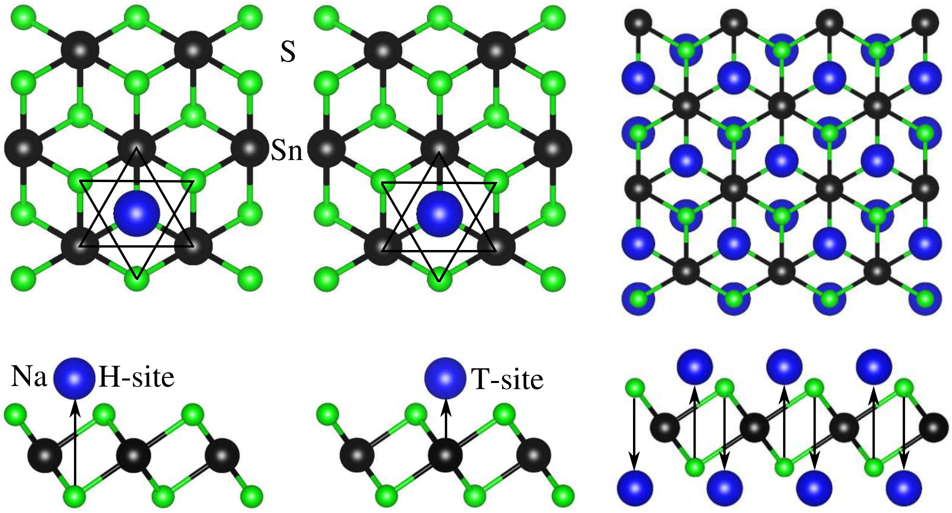

Figure 7.1: Top and the side views of a portion of monolayer SnS$_2$ with (left panel) Na at an H-site, (middle panel) Na at a T-site, and (right panel) monolayer SnS$_2$ with all top and bottom H-sites occupied by Na. The black, green, and blue solid spheres represent Sn, S, and Na atoms respectively.

Table 7.1: Geometric parameters, charge, and energetics of a single Na adsorption on a 3×3×1 SnS$_2$ supercell.

	H-site	T-site
d_{Na-S} Å	2.75	2.76
d_{Na-Sn} (Å)	3.90	3.39
E_b (eV)	1.36	1.34
q ($\lvert e\rvert$)	0.85	0.85

Interestingly, the distance of the Na adatom from all the nearest three S atoms is nearly the same when it is relaxed at H- and T-sites. In other words, the Na adatom has a similar S environment at the H- and T-sites. Therefore, the difference in the binding energy (E_b) of Na adsorption on these sites is only 20 meV (E_b at the H-site=1.36 eV, E_b at the T-site=1.34 eV). The binding energy for the adsorption of Na on a 3×3×1 SnS$_2$ supercell is defined by the formula

$$E_b = (E_{\mathrm{Sn}S_2} + nE_{\mathrm{Na(BCC)}} - E_{\mathrm{SnS2+Na}})/n$$

where E_{SnS2} and $E_{\mathrm{SnS2+Na}}$ represent the total relaxation energy of the pristine and Na adsorbed SnS$_2$ monolayers, n is the number of Na adatoms, and $E_{\mathrm{Na(BCC)}}$ is the total energy of bulk Na in its metallic body-centered cubic structure. According to this definition, of E_b, a more positive value of E_b means a stronger Na bond with the monolayer and vice versa. Table 1 shows the geometric parameters, charge, and binding energy of a single Na adsorbed on the H- and T-sites of the SnS_2 monolayer. The E_b and the averaged net charge on the Na for all possible distributions of Na over the monolayer SnS_2 are calculated as a function of Na content at H-sites. The data plotted in Fig. 7.2(a,b) are for E_b and averaged net charge on Na, respectively. Table 1 shows that the Na–Sn relaxation distance is larger than that of the Na–S. Since S is more electronegative than Sn, most of the Na charge transfers to the neighboring S atoms, which results in high E_b. Similarly, the other coming Na atoms are positively charged. Fig. 7.2(b) shows that the averaged net charge on the Na atoms decreases with increasing Na content. The Na^+–Na^+ distance also decreases with increasing Na content, which increases the repulsive forces. Decrease in the averaged net charge on the Na and the distance between Na ions are the two main factors affecting the binding energy of Na adsorption. E_b can be related to the total formation energy (E_f) by the relation $E_f = nE_b$ which has an upper limit on the Na storage capacity of the monolayer SnS_2. When the E_f drops to zero, the adsorption of further Na will allow Na to form a metallic cluster.

The percent change in the area of the monolayer with varying Na content is noticed, which is reported as a challenging problem in most of the Na and Li ion battery electrodes, particularly in the case of Sn and its derivative based anodes [118, 137, 138, 231, 232, 236]. The percent change in the area (ΔA) of the monolayer with increasing Na content is defined as:

$$\Delta A = [(A_{\mathrm{SnS_2}} - A_{\mathrm{Sn}S_2\mathrm{+nNa}}) \times 100\%]/A_{\mathrm{SnS_2}}$$

where $A_{\mathrm{Sn}S_2}$ is the area of a 3×3×1 SnS_2 supercell and $A_{\mathrm{Sn}S_2\mathrm{+nNa}}$ is the area of a 3×3×1 SnS_2 supercell with the n number of Na atoms adsorbed at the H-sites. As already mentioned, Na gets a positive charge upon adsorption over the monolayer SnS_2 and the H- and T-sites of SnS_2 are very active to Na adsorption. The repulsive forces between Na ions tend to keep them at the largest possible distance but the strong binding force of Na ions with the S prevents them from moving. So increasing Na content over the monolayer is likely to increase the strain on the monolayer, which results in an increased Sn–S bond distance. The Sn–S bond distance is 2.60 Å for the pristine SnS_2, which gradually increases with increasing Na content and reaches to 2.92 Å when all the top H-sites are occupied. Thus 19.7% increase in the area of the monolayer SnS_2 resulted when all the top H-sites are filled by Na, for a Na_1SnS_2 composition, as shown in Fig. 7.2(c). All the top and bottom H-sites of the monolayer have been filled without the decomposition of SnS_2 up to the level Na_2SnS_2. Increasing the Na concentration beyond this level decomposes the SnS_2 monolayer into Sn and Na_2S in an irreversible way. Bulk SnS_2 can have safe storage up to $LiSnS_2$ for Li insertion a after which the SnS_2 decomposes [118]. This shows that monolayer SnS_2 can have higher metal ion storage than the bulk.

Additionally, the maximum charge storage capacity and the average half-cell voltage (V_{avg})

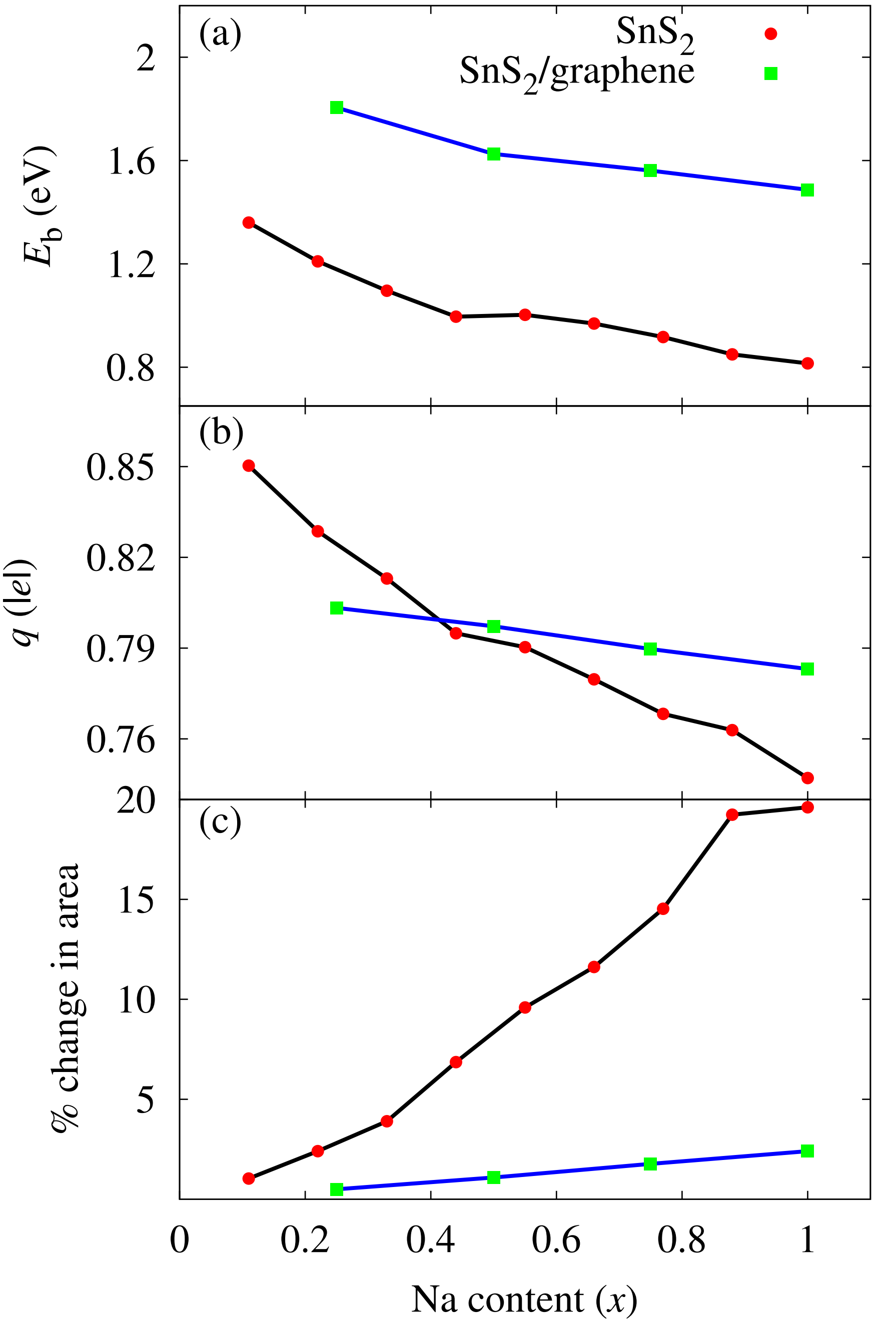

Figure 7.2: (a) E_b of the Na adatom, on the H-sites of monolayer SnS_2 and interface H-sites of the SnS_2/graphene heterostructure, (b) averaged net charge on Na, and (c) percent change in the area as a function of increasing Na content (x).

of the monolayer SnS_2 are calculated. The reversible reaction for the monolayer at the anode, when x number of H- and T-sites are occupied by Na, can be written as

$$x\mathrm{Na}^+ + x\bar{e} + \mathrm{SnS}_2 \rightleftharpoons \mathrm{Na}_x\mathrm{SnS}_2$$

The difference in E_b at the H- and T-sites is only 20 meV, which is negligible compared to the Na binding energy at these sites. There are two H- and two T-sites per unit formula (Na_xSnS_2), considering both the top and bottom sites. So as a whole there are four favorable sites for the Na adsorption per formula unit (Na_4SnS_2). Thus the maximum possible capacity of the monolayer is 586 mAh/g. This capacity is much higher than that of the commercially available graphite (Li_xC_6 ; $x \leq 1$) for LIBs and comparable with that of other 2D TMDs for NIBs [237]. The averaged half-cell voltage is defined as

$$V_{\mathrm{avg}} = -[E_{\mathrm{SnS_2+Na}} - E_{\mathrm{SnS_2}} - nE_{\mathrm{Na(BCC)}}]/ne$$

, where $\bar{e}$ is the charge on an electron. According to this definition the averaged half-cell voltage for the SnS_2 monolayer is 1.0 V, which is suitable for the anode material in NIBs.

7.3.3 Na diffusion on the SnS_2 surface

Fast diffusion kinetics of the adsorbed Na is desirable as it is directly related to the rate capability of a battery [113]. The diffusion pathways for the migration of Na from an energetically favored H-site to a similar adjacent H-site via a T-site (H–T–H) or a top S-site (H–S–H) are optimized with the application of NEB calculations. Five images are linearly interpolated between the H- and T-sites or H- and S-sites. The relative energy along these two paths is plotted in Fig. 7.3(a,b), respectively. Each red point on the plots indicates the relative energy with respect to the H-site along the reaction path. Our calculations suggest the MEP for the Na diffusion from one H-site to the adjacent H-site via a T-site by following a curved zigzag path, as shown in the inset of Fig. 7.3(a). The activation energy barrier is the energy difference between the highest energy point on the MEP and the reference point (H-site). This barrier of 0.13 eV is much lower than that of Li diffusion on silicene and defective graphene [85, 143] and is comparable to that of Na diffusion on MoS_2 and other 2D TMDs [97, 225]. The activation energy barrier along the H–S–H path is 0.60 eV and its trajectory is shown in the inset of Fig. 7.3(b). NIBs have higher charge/discharge rates than LIBs [238].

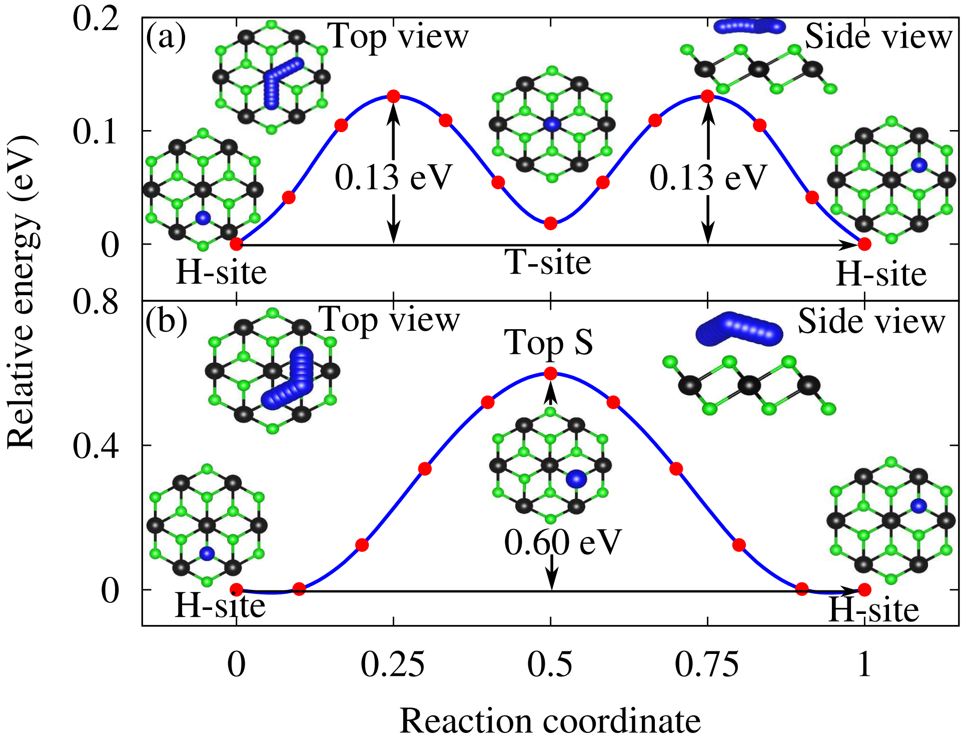

Figure 7.3: (a) MEP for the Na diffusion from one H-site to the adjacent H-site via a T-site with an energy barrier of 0.13 eV. Trajectory of Na along the H–T–H path is shown in the inset. (b) MEP for the Na diffusion from one H-site to the adjacent H-site via a top S-site with an energy barrier of 0.60 eV. The trajectory of Na diffusion along the H–S–H path is shown in the inset.

Table 7.2: Net charge (q), binding energy (E_b), and nearest Na-to-S distance ($d_{\mathrm{Na-S}}$) of a single Na adsorbed at the H-sites of the interface (H1-, H2-, H3-, and H4-), T-sites of the interface (T1-, T2-, T3-, and T4-), an H-site of the SnS_2 surface (H_S -site), a T-site of the SnS_2 surface (T_S-site), and above the center of a graphene ring (G_{cen}) of the SnS_2/graphene heterostructure

	H1	H2	H3	H4	T1	T2	T3	T4	H_S	T_S	G_{cen}
q ($\|e\|$)	0.80	0.81	0.81	0.80	0.80	0.81	0.80	0.80	0.82	0.83	0.65
E_b (eV)	1.76	1.81	1.81	1.77	1.78	1.80	1.73	1.73	1.41	1.37	0.10
$d_{\mathrm{Na-S}}$	2.73	2.72	2.74	2.73	2.74	2.75	2.76	2.73	2.69	2.71	2.71

7.3.4 Na insertion in the SnS_2/graphene heterostructure

The formation energy per atom (E_f) for the stacking stability of a graphene layer with the monolayer SnS_2 to make a SnS_2/graphene composite is defined as

$$E_f = (E_S + E_G - E_{S/G})/n$$

where E_S and E_S are the total relaxation energies of a 2×2×1 SnS_2 supercell and a 3×3×1 graphene supercell, respectively. $E_{S/G}$ is the total relaxation energy of a 2×2×1 SnS_2 and a 3×3×1 graphene composite and n is the total number of atoms in the supercell. According to this definition, the formation energy per atom for making the SnS_2/graphene heterostructure is 0.12 eV per atom. The evolution of energy in the formation of the composite confirms that the heterostructure is stable enough to be used as an anode material in NIBs. The equilibrium interlayer distance to the graphene is 3.4 Å from the top S and 4.85 Å from the Sn layer, which provides sufficient vacant space for the Na insertion (see Fig. 7.4).

Na insertion at the interface and both surfaces of the heterostructure is studied. The adsorption at the interface and both surfaces of the heterostructure is energetically stable, where the H- and T-sites at the interface are the most favorable sites. The E_b, Na-to-S averaged distance (d_{Na-S}), and charge (q) on Na at all adsorption sites of the heterostructure are tabulated in Table 7.2. Adsorption of the Na on the graphene surface, SnS_2 surface, and interface of the heterostructure is discussed one by one.

The position above the center of the graphene ring is the most favorable site for the Na adsorption on the pristine graphene. The E_b at this site is 0.553 eV and the charge transferred from Na to the graphene layer is 0.03 |e|. Thus our calculations confirm that the pristine graphene is not useful as an anode for NIBs which is in good agreement with the previous report. In the heterostructure case, Na can be stored above the center of the graphene ring (E_b = 0.10 eV) without the formation of a metallic cluster. The increase in E_b comes from the Na and S (nearest to the Na) interaction. Na adsorption above the C–C bridge and C atom of the

SnS_2/graphene is energetically unfavorable.

Na adsorption on the SnS_2 surface of the heterostructure prefers the H_s- and T_S-sites similar to the adsorption on the monolayer SnS_2. Here the E_b of the Na adatom is comparable with the E_b at the monolayer SnS_2. The Na adatom can be considered to interact with the SnS_2 monolayer only, because the graphene layer is far away from adsorbed Na at the SnS_2 surface of the heterostructure.

Na adsorption at the interface of the heterostructure prefers the H- and T-sites but the E_b at H-sites as well as at T-sites is different from the E_b at the other H-sites or T-sites. This difference in E_b occurs due to the different C environments at H- and T-sites at the interface of the heterostructure. As already discussed, Na interacts weakly with the graphene layer. So the H- and T-sites are still the compromised sites for the Na adsorption at the interface. The E_b of the Na adatom at the interface is higher than the E_b at the SnS_2 surface of the heterostructure, since Na at the interface interacts with both the SnS_2 and graphene surfaces of the heterostructure. These results of E_b for the Na adsorption at the surfaces and interface of the heterostructure have good agreement with the reports for Li insertion in phosphorene and graphene heterostructures.

Again we plot the binding energy, the averaged net charge on Na and the percent change in the area as a function of Na content by filling all the interface H-sites with Na atoms (Fig. 7.2(a)–(c)). This time the binding energy, the averaged net charge on Na, and the area of the monolayer are stable compared to those in the pristine SnS_2 case. The graphene fixes the Sn–S bond distance during the sodiation and provides a cushion to the SnS_2 monolayer. The change in the area upon Na insertion in the heterostructure case is 8.2 times less than that in the pristine SnS_2 case. It means that the area of the monolayer SnS_2 has been highly affected by the strong binding energy and the average net charge of Na. In the pristine SnS_2 case, the repeated sodiation and de-sodiation can break the Sn–S bond. This irreversible reaction negatively affects the performance of the anode in terms of reduced Na storage capacity and cycle life. However, this is not the case with the SnS_2/graphene heterostructure. The presence of mechanically strong graphene controls the change in the Sn–S bond length which is consistent with the experimental report.

High reversible capacity and fast electronic and ionic mobility are the requirements of an efficient electrode material. We have already discussed that the SnS_2 monolayer has high capacity for Na storage and a low activation energy barrier for Na ion migration. But the 1T SnS_2 monolayer is a semiconductor even at high Na concentration. On the other hand, graphene has high electronic conductivity and mechanical strength as well, but it does not show a good response for Na adsorption. We make the SnS_2/graphene heterostructure (the side view of the SnS_2/graphene with all H-sites occupied by the Na is shown in the inset of

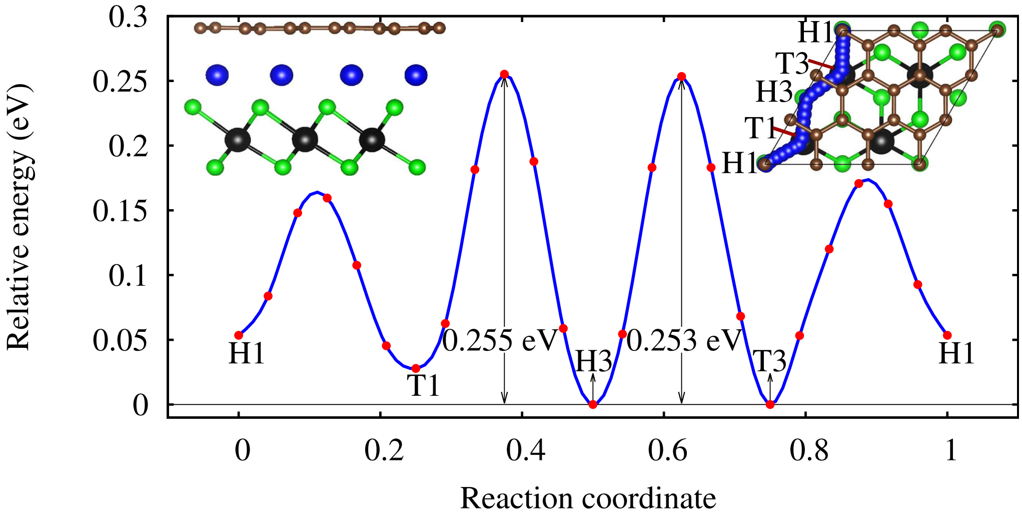

Figure 7.4: MEP for Na diffusion in the SnS_2/graphene heterostructure. The structure at the top left corner is the side view of the heterostructure with all the interface H-sites filled with Na. The structure at the top right corner is the top view of the SnS_2/graphene heterostructure, and the zigzag trajectory of Na along H1–T1–H3–T3–H1 is shown by the blue colored solid spheres.

Fig. 7.4.) so as to utilize these properties in an ideal anode material for NIBs.

7.3.5 Na diffusion in the SnS_2/graphene heterostructure

The MEP for the diffusion of Na ions, at the interface, through the nearest H- and T-sites is investigated, using the NEB method. The trajectory of Na along the MEP is shown by a series of blue colored spheres in the inset of Fig. 7.4, where we have taken the H3-site as the reference since the H3-site is the most favorable site. The activation energy barrier this time increases to 0.255 eV, but it is still lower than the Li migration barrier in pure and defective graphite and graphene, bulk Sn, and SnS_2 [239]. The diffusion barriers of Na and Li ions in bilayer and bulk materials are always higher than those of monolayers [97, 118, 143, 239, 240]. In this regard, our result is consistent with the literature. Comparing the trajectory of Na ions in the heterostructure (shown in the right top corner of Fig. 7.4) with the relative energy profile in Fig. 7.4, we deduce that the transition point for the Na atom is below the C–C bridge.

The activation energy barrier along the MEP can be reduced if the interaction of Na ions with the graphene layer is weakened by increasing the interlayer distance of graphene and SnS_2. In bulk MoS_2, the interlayer distance is reported as 6.18 Å which increases to 6.37 Å for the bilayer case. This increase in the interlayer distance has reduced the activation energy barrier for Li ions, from 0.49 eV to 0.32 eV [241]. The activation energy barrier for Li ions in bulk SnS_2 was reduced from 0.38 eV to 0.30 eV by the Ce substitution and to 0.23 eV by the

Table 7.3: In-plane Young's modulus (Y), Poisson's ratio (ν), and elastic moduli (C_{11} and C_{12}) for monolayers of graphene, MoS$_2$, SnS$_2$, and SnS$_2$ with all top H-sites filled with Na and heterostructures of SnS$_2$/graphene and SnS$_2$/graphene with all interface H-sites filled with Na

	Y (N/m)	C_{11} (N/m)	C_{12} (N/m)	ν
Graphene (reported)	340.8	352.0	62.6	0.178
MoS$_2$ monolayer	120.1	128.4	32.6	0.254
Graphene present	340.7	353.4	66.9	0.189
SnS$_2$ monolayer	66.4	82.5	29.1	0.245
SnS$_2$ monolayer + Na	41.5	53.0	24.7	0.423
SnS$_2$/graphene	425.5	445.5	94.3	0.212
SnS$_2$/graphene + Na	383.2	408.2	101.0	0.247

volume expansion [118].

The MEP for the diffusion of Na ions over the SnS$_2$ surface of the heterostructure is found from a H$_S$-site to the nearest H$_S$-site via the T$_S$-site. The trajectory of the Na diffusion from one H$_S$-site to the nearest H$_S$-site via the T$_S$-site is the same as the trajectory of Na diffusion on the monolayer SnS$_2$ along the MEP (Fig. 7.3). The only difference occurs in the activation energy barrier. The activation energy barrier of Na diffusion along the MEP on the SnS$_2$ surface of the heterostructure is higher by 0.06 eV than the energy barrier for diffusion on the monolayer SnS$_2$. This is because of the larger difference of E_b between the H$_S$- and T$_S$-sites compared to the E_b difference between the H- and T-sites of the monolayer SnS$_2$. The MEP for the Na diffusion on the graphene surface of the heterostructure is from one center of the graphene ring to the next one via the top of any C atom in between, following a zigzag path. The activation energy barrier along this path is 0.14 eV.

7.3.6 Electronic structure

In Li and Na ion batteries, fast charge and discharge rates are highly desirable, which are directly related to the charge carrier mobility [113]. The diffusion of the positive charge carriers (Na ions) has already been discussed. Now, to explain the electronic conductivity, we have shown the total density of states (DOS) profile for a 3×3×1 pristine SnS$_2$ supercell, 3×3×1 SnS$_2$ supercell with all the top and bottom H-sites occupied by Na, and 2×2×1 SnS$_2$ combined with a 3×3×1 graphene supercell in Fig. 7.5. The SnS$_2$ monolayer has shown a band gap of 1.54 eV, which agrees well with the literature [235, 242]. It decreases with increasing Na content but does not drop to zero, as required for efficient electrodes. Even for the Na$_2$SnS$_2$ composition the band gap is 1.19 eV. Contrary to SnS$_2$, the concentration of Na adsorption on the phosphorene has shown a very high sensitivity to the band gap. We successfully solve the problem of poor electronic conductivity, by the addition of a graphene

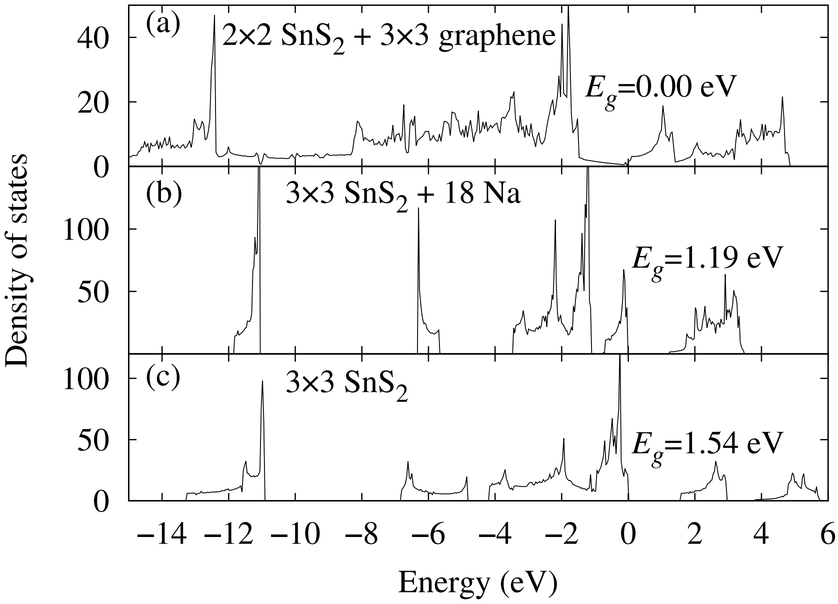

Figure 7.5: Total DOS (a) for the 2×2×1 SnS_2 and 3×3×1 graphene heterostructure, (b) 3×3×1 SnS_2 with all the top and bottom H-sites occupied by Na, and (c) 3×3×1 pristine SnS_2 shows different band gaps ranging from 0 to 1.54 eV.

sheet to the SnS_2 monolayer. The total DOS shows that the SnS_2/graphene has no band gap thus completing the requirement of high electronic conductivity.

7.3.7 Mechanical stability

The large area expansion found in the monolayer SnS_2 during the sodiation may cause structural instability. In the absence of a graphene layer the SnS_2 monolayer expands by 19.77% of its initial area by filling all the available top H-sites with Na. With the addition of a graphene layer, this expansion reduces to 2.4% for the same Na concentration. The cushion provided by the graphene layer successfully protects the anode from extra-large expansion and fixes the Sn and S atoms during the insertion and extraction process. The in-plane Young's modulus (Y) and the Poisson's ratio (ν) are defined as $Y = (C_{11}^2 - C_{12}^2)/C_{11}$ and $\nu = C_{12}/C_{11}$, respectively. The elastic moduli of the monolayer graphene, MoS_2, SnS_2, SnS_2 with all the top H-site filled with Na, SnS_2/graphene, and SnS_2/graphene with all the interface H-sites filled by Na are compared in Table 7.3. In our calculations the planar elastic stiffness coefficients $C_{11} = C_{22}$ and $C12 = C_{21}$ due to the structural symmetry. Although the coefficients of planar elastic stiffness for all our structures completes the Born stability criteria (C_{11} >0 and $C_{11} - |C_{12}| > 0$) [111], the in-plane Young's modulus of SnS_2 is too much lower than that of the other well-known two-dimensional materials such as graphene and MoS_2. The in-plane stiffness of the heterostructure is higher by 18.4 N/m than the sum of the individual stiffnesses of the graphene and SnS_2 monolayers. However, when all the H- sites are filled with Na, the interlayer distance of the graphene and SnS_2 increases by 0.88 Å. The difference in the stiffness in the combined and individual layer cases remains as small as 1 N/m. The reduced van der Waals interaction, because of the increased interlayer distance, might be the main reason for the decreased stiffness. energy barrier for Na diffusion, it is still much lower than that of the commercially available graphite in LIBs. The SnS_2/graphene heterostructure shows two advantages over the SnS_2 monolayer. It successfully tunes the electronic band gap and enhances mechanical stability. The low cost, high Na storage capacity, high electronic and ionic conductivity, nontoxic nature, and enhanced mechanical stability of the SnS_2/graphene show the high potential of this material as a commercial anode material for NIBs.

7.4 Summary

In summary, the adsorption and diffusion of Na on a 1T structured SnS_2 monolayer and in a SnS_2/graphene heterostructure are studied systematically. Na prefers the H- and T-sites with binding energies of 1.36 and 1.34 eV per adatom, respectively. The SnS_2 monolayer has an appreciable Na storage capacity of 586 mAh/g and an average half-cell voltage of 1.0 V. The activation energy barrier along the MEP is 0.13 eV when Na ions diffuse from one H-site to the nearest H-site via the T-site on the surface of the monolayer. But a large area expansion of the monolayer is observed during the sodiation and the total density of states shows that monolayer SnS_2 is semiconducting with a band gap of 1.54 eV, which reduces to 1.19 eV when all the top and bottom H-sites are occupied by Na atoms. Both these problems can be successfully solved by making a SnS_2/graphene heterostructure. Although the SnS_2 monolayer itself can be used as an anode for NIBs with low Na storage capacity, the SnS_2/graphene heterostructure improves its performance. The combination of graphene with SnS_2 highly modifies the stiffness of the anode material and reduces the percent area expansion 8.2 times that of the SnS_2 monolayer. The insertion of Na in the SnS_2/graphene heterostructure shows that Na prefers the H- and T-sites for adsorption but this time the binding energy at each H- and T-site can be different. This difference in the binding energy is due to the different C environments at each H- and T-site. The energy barrier for the Na diffusion in the heterostructure case increases to 0.25 eV, which shows that the diffusion of Na in bilayers and bulk is slower compared to that on the monolayer. The transition saddle point for the Na diffusion is at the center of the C–C bridge. Although the addition of graphene to the SnS_2 monolayer increases the energy barrier for Na diffusion, it is still much lower than that of the commercially available graphite in LIBs. The SnS_2/graphene heterostructure shows two advantages over the SnS_2 monolayer.

It successfully tunes the electronic band gap and enhances mechanical stability. The low cost, high Na storage capacity, high electronic and ionic conductivity, nontoxic nature, and enhanced mechanical stability of the SnS_2/graphene show the high potential of this material as a commercial anode material for NIBs.

Chapter 8

MoS_2@VS_2 as a superior anode

8.1 Introduction

Clean, safe, and efficient storage of electrical energy both at large and at small scales is one of the worldwide most important issues. Rechargeable Li ion batteries (LIBs) have been effectively serving in small portable electronic devices for the last two decades. Its use in electric vehicles is however less efficient because of its competition with gasoline/diesel-powered vehicles. Although an electric vehicle does not pollute and is more economical, it is costly, requires longer time for recharge, and enables only short-distance movement. In a hybrid vehicle some of these problems have been partially controlled. Neverending research on safety improvements, increasing rate capability, storage capacity, cycle life, and voltage of the cell of a rechargeable metal ion battery is still in progress. On the other hand, to take hold of the commercial market, searching for cheap, abundant, and environmentally friendly ingredients is also important [48, 243–245] .

MoS_2 has shown a leading role in manufacturing the electronic devices and emerging physics [40, 246–250]. Weak van der Waals interlayer interactions and strong in-plane covalent bonding in MoS_2 allow enough room between the layers to host the small Li/Na ions without large volume variations. Layered crystalline structures with large interlayer openings such as transition metal dichalcogenides have remained a focus with researchers who are focusing on finding intercalation compounds to store Li/Na ions [90, 139, 251, 252]. The prevailing graphite anode needs to be replaced by high-capacity anode materials in the next generations of rechargeable metal ion batteries. The Li storage capacity of bulk MoS_2 (340 mAh/g) is even less than that of graphite (372 mAh/g). However, the Na storage capacity of MoS_2 (146 mAh/g) is much higher than graphite because of its larger interlayer space. The Li storage capacity of bilayer MoS_2 (300 mAh/g) is lower than that of bulk MoS_2 [241].

The adsorption energy of Li/Na ions on monolayer MoS_2 is so low that for reasonable density of ions, metallic clusters are formed when the ions come close to the metallic distance during diffusion. The Li/Na ions involved in the clusters do not take part in the reversible reactions at the anode and cathode. Vacancies in monolayer MoS_2 have shown a significant increase in the binding strength of Li/Na ions. Similar tactics have worked well in graphene and silicene as well. The high Li storage capacity of MoS_2 nanoribbons can be ascribed to the edge effects. However, the diffusion energy barrier of a Li ion on the surface of defect-mediated monolayer MoS_2 (0.42 eV) goes higher than that on pristine monolayer MoS_2 (0.1 eV), which results in reduced rate capability and increased charging time of the cell [80, 143, 188, 241, 253]. Another important issue in MoS_2 as anode is its high electronic band gap which blocks the recovery of Li/ Na ions. Desired properties from a layered material can be easily achieved by contacting it with another layered material with a careful selection. Chowdhury *et al* [254]. reported that capping of black phosphorene with *h*-BN enhanced the Li/Na binding energy from 1.8 to 2.8 eV.

In our previous study, we showed that large-area expansion and insulating nature of monolayer SnS_2 during the sodiation process can be solved by the addition of a graphene sheet [110]. Similar strategies have been used for phosphorene [117], MoS_2 [255] silicene [147], and some other insulating materials. The common feature of graphene addition was reported as the enhancement of electronic conductivity, while some authors claimed increased Li/Na storage capacity of the electrode as well [116, 229, 256–258]. However, it is well known that pristine graphene in flat structure is almost inert to the adsorption of metal ions. Here, instead of graphene, we proclaim the significance of monolayer VS_2 as metallic additive for monolayer MoS_2.

In this article, the insulating monolayer MoS_2 is presented as a poor adsorber of Li/Na ions and the metallic monolayer VS_2 is shown to be capable of high-density Li/Na storage. However, the monolayer VS_2 has not been synthesized to date. We show that monolayer VS_2 can be grown on monolayer MoS_2 to make MoS_2@VS_2 nanocomposite. The combining process of monolayer MoS_2 and monolayer VS_2 is exothermic enough to stabilize monolayer VS_2. The charge density difference of the combined and individual monolayers MoS_2 and VS_2 predicts the accumulation of a low-density interfacial charge cloud, donated by the V atom of monolayer VS_2. The charge redistribution during the growth of metallic monolayer VS_2 on monolayer MoS_2 boosts the electrical conductivity and Li/Na storage capacity of the nanocomposite. It also has the lithiation/sodiation voltage range feasible for anodes.

8.2 Computational details

All our calculations are performed by using the spin density functional theory, implemented in the Vienna Ab initio Simulation Package [100]. Generalized gradient approximation with the parametrization scheme of Perdew–Burke–Ernzerhof [100] is applied for the electron-electron exchange correlation processes, whereas the electron–ion interactions are processed by the projector augmented wave method. A cutoff energy of 500 eV is considered for the plane-wave expansion of the electronic eigenfunctions for the MoS_2@VS_2 nanocomposite. The force criterion used for structure relaxation is 0.001 eV/Å. The interlayer interactions have been weakened by producing a minimum vacuum of 30 Å. The van der Waals energy correction has been considered in the nanocomposite using the semiempirical correction scheme of Grimme (DFT-D2) [259]. The Γ-point sampling with $6\times6\times1$ k points of the nanocomposite is used for integration of the Brillouin zone. Phonon modes are calculated using the finite displacement method implemented in the Phonopy program [148]. A $5\times5\times1$ supercell of the MoS_2@VS_2 nanocomposite with atomic displacements of 0.01 Å is considered for the phonon calculations. A $3\times3\times1$ supercell of the MoS_2@VS_2 nanocomposite is examined for the adsorption and diffusion of Li/Na ions. The nudged elastic band method [103] is used for optimization of minimum energy paths for the diffusion of Li/Na ions on both surfaces and the interface of the MoS_2@VS_2 nanocomposite. Bader charge analysis [149] is used to scale the charge transferred by the Li/Na atoms.

8.3 Results and discussion

8.3.1 Adsorption and diffusion of Li/Na ions on MoS_2, VS_2

Monolayer MoS_2 has been confirmed theoretically and synthesized and characterized experimentally [40, 247, 260]. Monolayer VS_2 is a strongly correlated material, and most of its properties depend upon the effective Hubbard parameter (U_{eff}). Stable phonon modes of vibrations can be achieved by selecting $U_{eff} \leq 2.5$ eV. Although the freestanding monolayer VS_2 was studied theoretically, there are some experimental reports about a few-layered VS_2. There is no report on the successful synthesis of monolayer VS_2 [261–264]. Similar to the literature, our calculations show that 2H is the lowest energy phase both for monolayer MoS_2 and for monolayer VS_2 [255, 261]. The lattice parameters are $a = b = 3.183$ Å for monolayer MoS_2 and $a = b = 3.174$ Å for monolayer VS_2.

Monolayer MoS_2 has a direct band gap of about 1.67 eV, while monolayer VS_2 is metallic and has a magnetic moment of $1\mu_B$ per unit cell. All these results are in good agreement with the previous reports [188, 263, 265].

Table 8.1: Formation energy, charge, and M-S bond distance of a single metal ion, when adsorbed at the H- and T-sites.

	Li			Na		
Adsorption site	E_b (eV)	q |e|	$d_{\mathrm{Li-S}}$ (Å)	E_b (eV)	q |e|	$d_{\mathrm{Na-S}}$ (Å)
Mo_{sur}	0.07	0.87	2.36	0.05	0.85	2.71
Mo_H	0.08	0.88	2.36	0.08	0.84	2.71
V_{sur}	1.97	0.87	2.36	1.85	0.85	2.71
V_H	1.88	0.88	2.36	1.85	0.85	2.70

Here, for the sake of convenience, we present a brief summary of adsorption and diffusion of Li/Na ions on the individual monolayers of MoS_2 and VS_2, whereas our theme is to report the superior electrochemical performance of MoS_2@VS_2 nanocomposite. A 3×3×1 supercell of the 2H phase of monolayer MoS_2 and monolayer VS_2 is considered to search out the energetically stable adsorption sites for Li/Na ions. Binding energies (E_b) of Li/Na ions with the monolayer MoS_2 or monolayer VS_2 are defined as

$$E_b = E_{\mathrm{MoS_2/VS_2}} + nE_{bulk(\mathrm{Li/Na})} - E_{\mathrm{MoS_2/VS_2}} + n(\mathrm{Li/Na})$$

where $E_{\mathrm{MoS_2/VS_2}}$ is the energy of a 3×3×1 supercell of pristine monolayer MoS_2 or monolayer VS_2, $E_{bulk(\mathrm{Li/Na})}$ is the energy for Li/Na ions in its body-centered cubic structure, and $E_{\mathrm{MoS_2/VS_2}} + n(\mathrm{Li/Na})$ is the energy of a 3×3×1 supercell of monolayer MoS_2 or monolayer VS_2 plus n Li/Na adatoms. Positions right above the Mo atom of MoS_2 (the so called Mo_{sur} site) and V atom of VS_2 (V_{sur} site) are found as energetically the most favorable sites for the adsorption of Li/ Na ions. The next favorable site after the Mo_{sur}/V_{sur} is the position above the center of Mo-S hexagon (Mo_H site) or V-S hexagon (V_H site). The adsorption information of a single Li/Na ion on these sites is summarized in Table 8.1, which shows that Li/Na binding with the monolayer MoS_2 is so weak that if the concentration of the adsorbed ions is slightly increased Li/ Na ions starts metallic clustering and these ions will not be able to take part in the reversible electrochemical reactions at the anode or cathode. Thus, the pristine monolayer MoS_2 is not a good choice as anode for Li/Na ion batteries. The problem for monolayer VS_2 is that it is still not confirmed experimentally.

The nudged elastic band method is used to optimize the minimum energy path for the diffusion of Li/Na ions by the linear interpolation of three images between the neighboring Mo_{sur}/V_{sur} and Mo_H/V_H sites. Relative energy profiles for the diffusion of Li/Na ions over the surface of monolayer MoS_2 and monolayer VS_2 are plotted in Fig. 8.1. The diffusion energy barriers are in good agreement with the previously reported results [226, 266, 267]. The diffusion energy barrier for Na is lower than that of Li, which is due to the comparatively

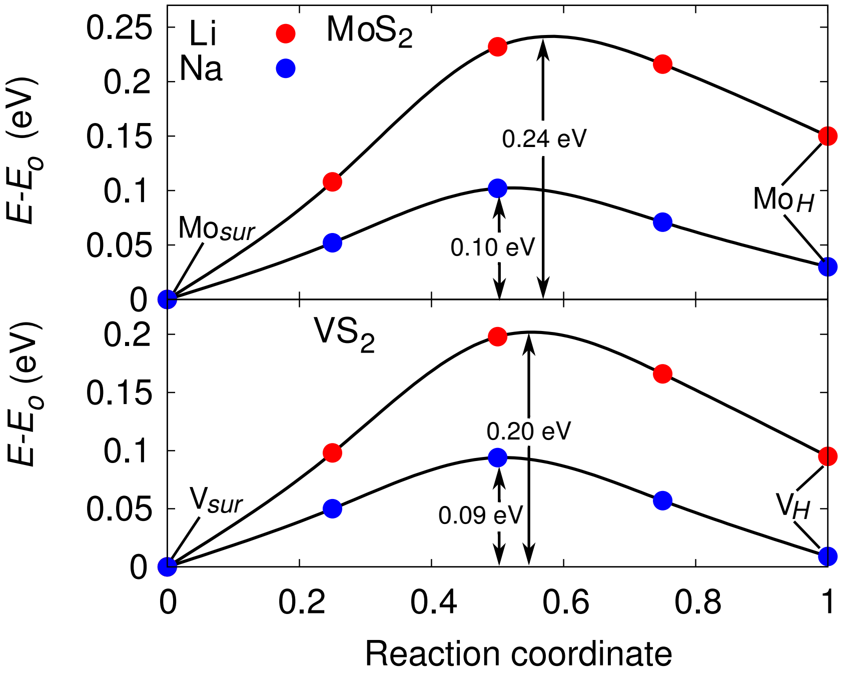

Figure 8.1: Relative energy profiles through the minimum energy paths for the diffusion of Li/Na ions on the surface of (a) monolayer MoS_2 from Mo_{sur} site to Mo_H site and (b) monolayer VS_2 from the V_{sur} site to the V_H site.

weak Coulombic interaction of Na ions with the monolayer because of its larger ionic radius. Similar trends have been found in other studies as well [50, 114, 167, 268]. More explanations about the adsorption and diffusion of Li/Na ions on monolayer MoS_2 and VS_2 can be found in references .[188, 226, 241, 266, 267].

8.3.2 Stacking stability

As monolayer MoS_2 and VS_2 have almost the same lattice parameters and both are stable in the hexagonal geometry (2H phase), the calculated lattice mismatch between them is so small (~0.28%) that monolayer VS_2 completely covers monolayer MoS_2 as shown in Fig. 8.2(a). The equation

$$E_{stack} = (E_{\mathrm{MoS_2}} + E_{\mathrm{VS_2}} - E_{\mathrm{MoS_2@VS_2}})/N$$

defines the stacking energy (E_{stack}) (unit is eV/atom) of the nanocomposite, where $E_{\mathrm{MoS_2@VS_2}}$ is the energy of the MoS_2@VS_2 unit cell, $E_{\mathrm{MoS_2}}$ is the energy of the unit cell of monolayer MoS_2, $E_{\mathrm{VS_2}}$ is the energy of the unit cell of monolayer VS_2, and N is the number of atoms. Stacking energies and interlayer distances for the four different stacking orders of MoS_2@VS_2 nanocomposite are shown in Fig. 8.2. E_{stack} of the MoS_2@VS_2 is much higher than that of the

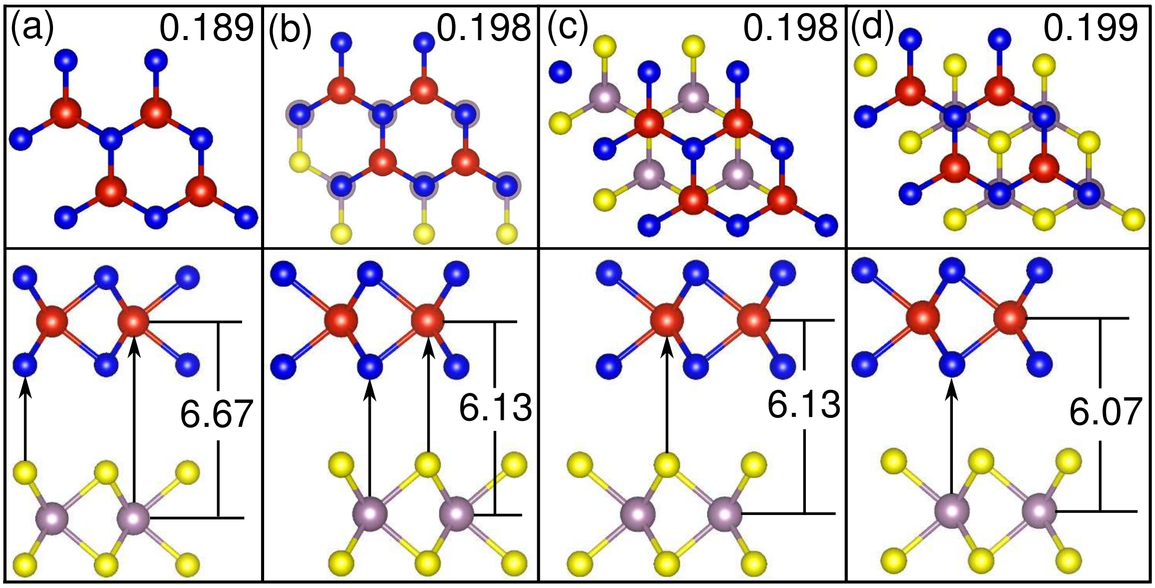

Figure 8.2: Top and side views of (a) AA stacking, (b) AB stacking, (c) S atom of MoS_2 above the V atom of VS_2, and (d) S atom of VS_2 above the Mo atom of MoS_2 of monolayer MoS_2 and VS_2. Values given with the top views show the stacking energy in eV/atom; values given with the side views show the vertical distance between Mo and V in Angstroms. Dark blue and yellow spheres represent the S atoms of monolayer VS_2 and monolayer MoS_2, while red and gray spheres are for V and Mo, respectively. Stacking order shown in d is energetically the most stable stacking.

graphene/SnS_2 (0.12 eV/atom) [110] and graphene@MoS_2 (0.03 eV per C atom) nanocomposite [255], which is due to the fact that free-standing monolayer VS_2 is chemically very active, while graphene and monolayer MoS_2 both are stable.

Therefore, the interaction of monolayer MoS_2 with the monolayer VS_2 is much stronger than that with the graphene. To explain the release of a high amount of energy in the formation of $MoS_2@VS_2$ nanocomposite, the charge density difference

$$(\Delta\rho = \rho_{\mathrm{MoS_2@VS_2}} - \rho_{\mathrm{MoS_2}} - \rho_{\mathrm{VS_2}})$$

of the nanocomposite and monolayer MoS_2 and monolayer VS_2 for the stacking order of Fig. 8.2(d) is shown in Fig. 8.3. In this stacking, the interfacial S atoms of the two layers are at a distance of 3.55 Å and electrons are accumulated at the interface between MoS_2 and VS_2, which induces strong interlayer coupling. If E_{stack} is attributed to the electron cloud at the interface S atoms only, then the energy released per unit bond is 1.194 eV. However, the density of the interfacial charge is too low, and the distance between the nearest S atoms of the two layers is also larger compared to V-S or Mo-S bond lengths; therefore, it is not

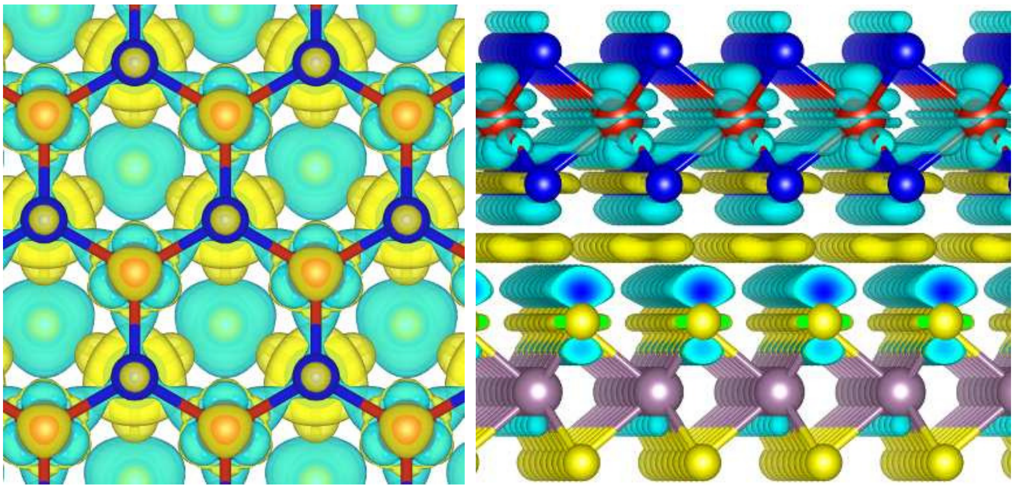

Figure 8.3: Top and side views of the charge density difference ($\Delta\rho$) of the $MoS_2@VS_2$ nanocomposite and monolayer MoS_2 and monolayer VS_2. Electron gain is indicated by yellow at the isosurface of 2.5×10^{-4} $|e|/\text{Å}^3$ and loss by light blue at the isosurface of 2.5×10^{-4} $|e|/\text{Å}^3$.

a chemical bond but a van der Waals interaction. The side view of Fig. 8.3 depicts that V are charged more highly than any other atom of the $MoS_2@VS_2$ nanocomposite, which means that the interfacial charge is due to the out-of-plane spreading of the V orbitals. The interfacial electron cloud induces a dipole moment in monolayer MoS_2. This redistribution of charge in the $MoS_2@VS_2$ nanocomposite contributes to stabilize the monolayer VS_2.

Further we show the phonon dispersion modes in Fig. 8.4 for the most stable stacking order (see Fig. 8.2(d)) to confirm the dynamic stability of the nanocomposite. As mentioned earlier, the experimental synthesis of freestanding monolayer VS_2 has not been realized until today, but the computational investigations revealed that it could have stable phonon modes for $U_{eff} \leq 2.5$ eV [261–263]. In Fig. 8.4, however, the stable phonon modes for the $MoS_2@VS_2$ nanocomposite show that monolayer VS_2 can be stabilized dynamically by using monolayer MoS_2 as a substrate. Furthermore, the in-plane elastic stiffnesses of the monolayer MoS_2, monolayer VS_2, and $MoS_2@VS_2$ nanocomposite are studied. The in-plane elastic stiffness is 124.04 N/m for monolayer MoS_2, 93.18 N/m for monolayer VS_2, and 219.50 N/m for $MoS_2@VS_2$ composite. It shows that the elastic stiffness of the nanocomposite has been enhanced by 2.28 N/m due to the synergic effects. To investigate the temperature effects on the stability of the nanocomposite, a snapshot of the $MoS_2@VS_2$ nanocomposite after running 1500 steps of *ab initio* molecular dynamics simulations with a time step of 3 ps at 300 K is are brought. The small deviations of atoms from their lattice sites at equilibrium show that the nanocomposite is stable at room temperature.

One of the most desired properties of the electrode materials is their high electronic con-

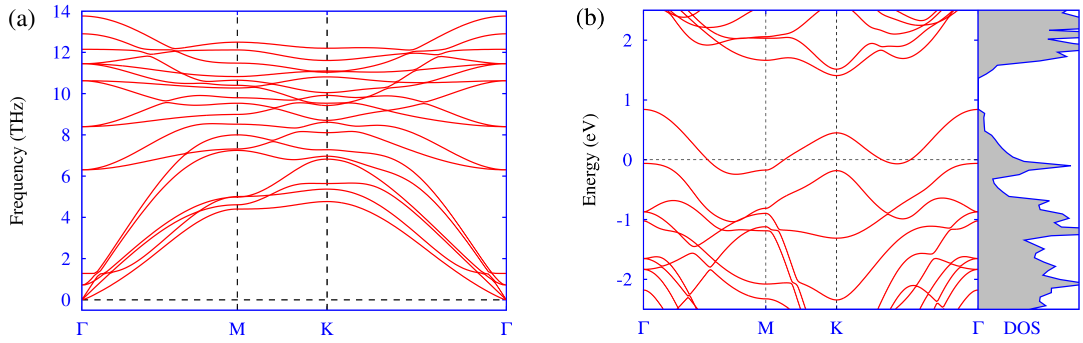

Figure 8.4: (a) Phonon dispersion modes for the $MoS_2@VS_2$ nanocomposite. (b) Electronic band structure and total density of states for the $MoS_2@VS_2$ nanocomposite.

Table 8.2: Binding energy (E_b) and charge (q) transferred from Li/Na atoms intercalated in a 3×3×1 supercell of the $MoS_2@VS_2$ nanocomposite at the interface site below V (V_i), interface site below Mo (Mo_i), surface site above V (V_{sur}), surface site above Mo (Mo_{sur}), surface site above the center of V−S Hexagon (V_H), surface site above the center of Mo−S hexagon (Mo_H), and interface site below the V−S hexagon (V_{Hi})

	V_i	Mo_i	V_{sur}	Mo_{sur}	V_H	Mo_H	V_{Hi}
E_b (eV)							
Li	2.52	1.79	2.28	1.10	2.17	0.94	2.04
Na	1.90	1.29	2.19	1.00	2.19	0.96	1.53
q ($\lvert e \rvert$)							
Li	0.84	0.83	0.87	0.88	0.88	0.88	0.83
Na	0.78	0.81	0.85	0.85	0.85	0.85	0.80

ductivity without which full recovery of Li/Na ions is not possible. The strategy of graphene insertion in the electrode materials has been broadly applied for the enhancement of electronic conductivity [110, 117, 147, 255] . Reports over Li/Na adsorption on pristine graphene reveal that graphene itself is not a good choice for anode because of its poor Li/Na adsorption capability. Fig. 8.5 shows the electronic band dipoles (0.907 μ_B per unit cell) which can be studied in detail in a separate article.

8.3.3 Adsorption and diffusion in $MoS_2@VS_2$

The total binding energy (E_b) of Li/Na adsorption on surfaces and the interface of the $MoS_2@VS_2$ nanocomposite is systematically studied. Here E_b is defined as $E_b = E_{MoS_2@VS_2} + nE_{Li/Na} - E_{MoS_2@VS_2} + n(Li/Na)$, where $E_{MoS_2@VS_2} + n(Li/Na)$ is the total energy of the $MoS_2@VS_2$ nanocomposite with n being the number of Li/Na atoms adsorbed on the surface or interface sites of the nanocomposite, $E_{MoS_2@VS_2}$ is the energy of the nanocomposite without Li/Na adatom, and $E_{Li/Na}$ is the energy per atom of bulk Li/Na (in body-centered cubic phase). E_b

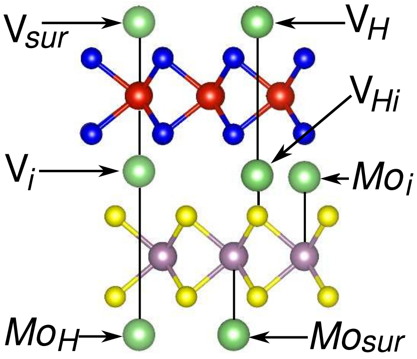

Figure 8.5: Schematic view of the Li/Na adsorption sites on the surfaces and interface of the MoS_2@VS_2 nanocomposite

of a single Li/Na ion is calculated on a 3×3×1 supercell of the MoS_2@VS_2 nanocomposite to find out energetically the most favorable adsorption sites. E_b and charge transferred by a Li/Na adatom at different adsorption sites of a 3×3×1 supercell of MoS_2@VS_2 nanocomposite are shown in Table 8.2. These sites are shown schematically in Fig. 8.5.

Comparing E_b of a Li/Na ion at the MoS_2 surface or interface of MoS_2@VS_2 (given in Table 2) with that on the monolayer MoS_2 (given in Table 1) shows that monolayer MoS_2 is made capable for higher density storage of Li/Na by making the MoS_2@VS_2 nanocomposite. The enhanced E_b of Li/Na ions in the nanocomposite is due to the charge redistribution in the formation of the nanocomposite. To calculate the Li/Na adsorption capacity of the MoS_2@VS_2 nanocomposite, the number of Li/Na adatoms is increased by filling the adsorption sites in descending E_b sequence. For the same capacity, filling different adsorption sites results in different E_b as shown in Fig. 8.6(a), but we consider the configurations with the highest E_b for each case. The filling sequence of the adsorption sites in descending E_b order is V_i, V_{sur}, Mo_{sur}, V_H, Mo_i, Mo_H.

Li intercalation in the MoS_2@VS_2 nanocomposite for the highest capacity can be seen in Fig. 8.7. Intercalation of Li/Na ions has a very small effect on the Mo-S and V-S bond lengths but incredibly increases the MoS_2-VS_2 interlayer distance. An increase in the interlayer distance for Na intercalation is larger than Li intercalation for the same capacity, which is due to the larger ionic size of Na.

For example, the interlayer distance for Li intercalation shown in Fig. 8.7 is 9.055 Å while for the same concentration of Na intercalation it is about 9.488 Å. Fig. 8.6 shows that the nanocomposite is energetically stable even after high-density Li/Na intercalation, while Fig. 8.7 shows that neither the MoS_2 layer nor the VS_2 layer of the nanocomposite decompose to Li_2S and Mo or V; therefore, this anode is expected to have high recyclability and long life. The highest possible specific capacity of the MoS_2@VS_2 nanocomposite without considering

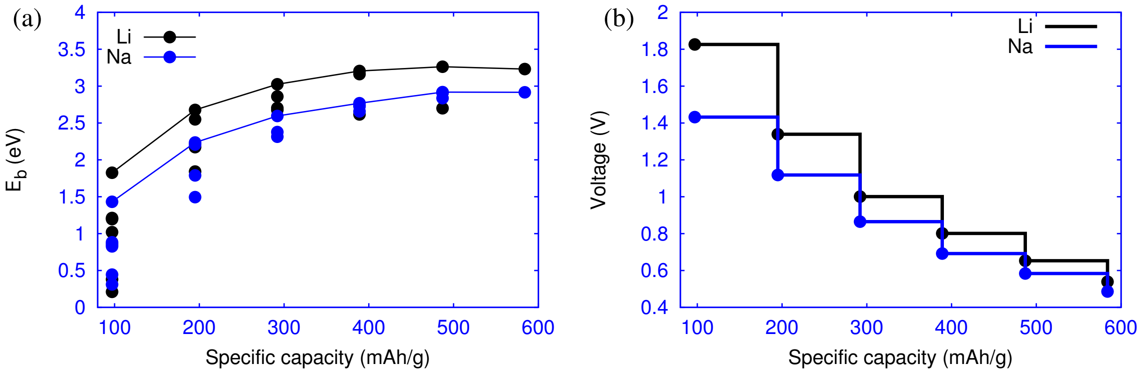

Figure 8.6: Total binding energy of Li/Na adsorption as a function of increasing specific capacity

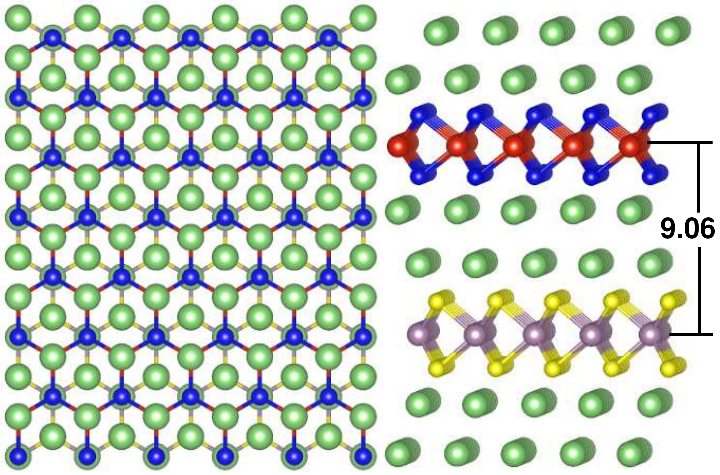

Figure 8.7: Top and side views of maximum possible Li storage (584 mAh/g) in $MoS_2@VS_2$ nanocomposite. Both layers of the heterostructure maintain their structure shape, but the interlayer distance is increased by 2.99 Å.

the mass of Li/Na ions is 584 mAh/g, which is much higher than that of monolayer MoS_2. By this way the two materials of the nanocomposite cover weakness of each other, that is, the MoS_2 layer stabilizes the VS_2 layer and the VS_2 layer upgrades the Li/Na adsorption capacity of the MoS_2 layer. The open-circuit voltage of the nanocomposite with increasing Li/Na adsorption concentration is shown in Fig. 8.6(b). The voltage ($V = E_b/n|e|$) profile of the $MoS_2@VS_2$ nanocomposite with increasing Li/Na concentration is similar to graphite, bulk MoS_2, and other anode materials [90, 112]. The charging voltage range (1.8–0.5 V for lithiation and V for sodiation) of the nanocomposite is suitable to be used as anode material.

The diffusion of a Li/Na ion from a stable adsorption site to the next stable adsorption site on the VS_2 surface, MoS_2 surface, and interface of $MoS_2@VS_2$ nanocomposite is studied one by one using the nudged elastic band method. As shown in Table 8.2, V_{sur} is energetically the most favorable adsorption site both for Li and for Na ions on the VS_2 surface of $MoS_2@VS_2$, while V_H is the second favorable adsorption site on the same surface. Therefore, energy paths for the diffusion of a Li/Na ion from a V_{sur} site to a nearby V_H site on the VS_2 surface of $MoS_2@VS_2$ nanocomposite is analyzed on a 3×3×1 supercell, and the relative energy is plotted in Fig. 8.8(a). Here the diffusion energy barriers for Li (0.24 eV) and Na (0.10 eV) are only slightly higher than their diffusion barriers on monolayer VS_2 shown in Fig. 8.1(b). The energy barrier of a Na ion diffusion is lower than that of a Li ion, which is similar to the trend of Li/ Na diffusion energy barriers on monolayer MoS_2 and monolayer VS_2.

The relative energy profile for the diffusion of a Li/Na ion on the MoS_2 surface of the $MoS_2@VS_2$ nanocomposite from a Mo_{sur} site to a nearby Mo_H site is shown in Fig. 8.8(b). Here again the diffusion energy barriers of Li/Na ions are slightly larger than those on pristine monolayer MoS_2 (shown in Fig. 8.1). The diffusion energy barriers for Li/Na migration over both surfaces are less than their diffusion energy barriers on pristine and defected graphene and silicene [166, 253].

Diffusion of Li/Na ions at the interface of $MoS_2@VS_2$ nanocomposite is also studied. Table 8.2 shows that the most favorable adsorption site for Li/Na ion on a 3×3×1 supercell of $MoS_2@VS_2$ nanocomposite is the V_i site and V_H is the second most favorable one. We therefore study the diffusion of a Li/Na ion from a V_i site to a V_H site as shown in Fig. 8.9. Since the V_i-to-V_H path is periodic because of the structural symmetry of the nanocomposite, the V_i-to-V_H diffusion of the ions is sufficient to provide complete insight in the diffusion of the ions at the interface. The energy barrier of the diffusion for Li at the interface is 0.45 eV, while for Na it is 0.44 eV. The diffusion energy barrier at the interface is thus higher than that at the surfaces, which is the case with other well-known electrode materials as well [110, 241, 269]. Some authors recently reported that considering the zero-point energy and quantum tunneling effects, diffusion of the light Li ions at 300 K can be faster by 15.4% than that calculated at 0 K. However, these effects are not expected dominantly for the heavier Na ions [254, 270].

8.4 Conclusions

Calculations based on spin density functional theory showed that the monolayer VS_2 can be stabilized in energy and phonon vibrations on monolayer MoS_2. Growth of the unstable monolayer VS_2 over monolayer MoS_2 results in high energy release. The charge density difference shows that there is electron accumulation at the interface between the MoS_2 layer and the VS_2 layer of the $MoS_2@VS_2$ nanocomposite. Phonon dispersion modes confirm the dynamic stability of the $MoS_2@VS_2$ nanocomposite. The electronic band structure and density

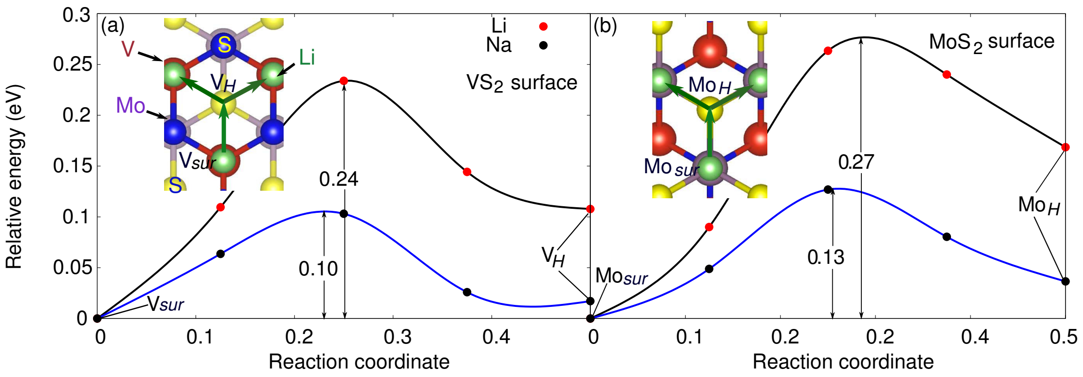

Figure 8.8: Minimum energy paths and saddle points for the diffusion of a Li/Na ion (a) from a V_{sur} site to a nearby V_H site on the VS_2 surface of MoS_2@VS_2 nanocomposite and (b) from a Mo_{sur} site to a nearby Mo_H site. Insets of (a) and (b) show the pathways. Energies of the saddle points are given in eV.

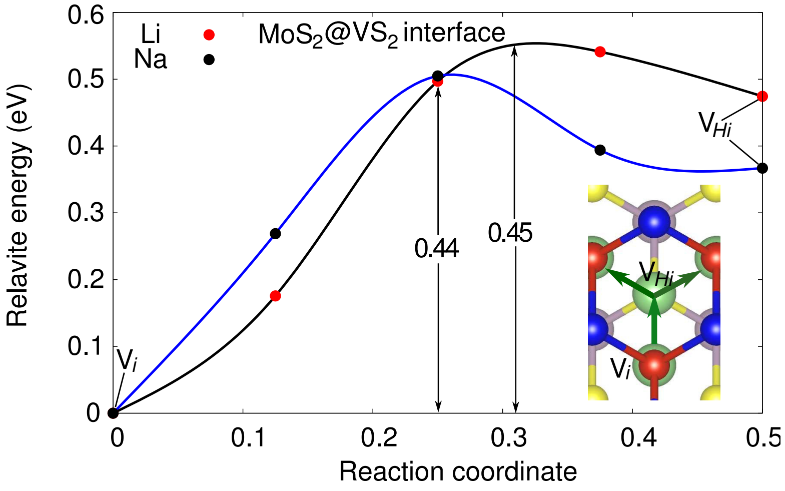

Figure 8.9: Minimum energy path for the diffusion of a Li/Na ion at the interface from a V_i site to a nearby V_{Hi} site. Inset shows the diffusion path schematically.

of states show that the MoS_2@VS_2 nanocomposite is metallic. Formation of the MoS_2@VS_2 nanocomposite enables the MoS_2 surface to adsorb a high density of Li/Na ions. The maximum Li/Na storage capacity of the MoS_2@VS_2 nanocomposite is as high as 584 mAh/g. The energy barriers for the diffusion of Li/ Na ions over the surfaces of the heterostructure are comparable with those on the surface of monolayer MoS_2 and monolayer VS_2, while at the interface it is comparable with the diffusion energy barrier in bulk MoS_2. The nanocomposite utilizes different properties of the two monolayers in a single hybrid anode with enhanced electrochemical performance.

Chapter 9

Summary

In summary, we have brought a computational study on the stability, metal ion adsorption and diffusion properties, electronic structural properties, and spontaneous and induced polarization of the novel single layer materials. For device applications, a single material may not have all the required features, a verticle heterostructure is constructed of two different materials to fulfill the requirements. We have proved that such techniques can be used to boost the performance of a device.

The environmental concern due to the massive usage of the combustion fuel and increasing demand for energy has accelerated the research on solar and wind like sustainable energy reservoirs. However, the fluctuation in the production of energy from such sources and its demand needs short and long time storage of energy. On the other hand, wireless electronic technology is growing day by day where the use of Li ion batteries is crucial. The limiting resources and the high cost of Li has compelled the researchers to think about alternatives to Li and improve the efficiency of the existing Li ion batteries.

In chapter 3 we have studied the stable 1T phase of single layer TiS_2 for adsorption and diffusion of Li, Na, K, Mg, and Ca ions. We found high storage capacity and low diffusion barriers of the TiS_2 for these ions. The electronic properties of TiS_2 ensure the high reversibility of the metal ions. In chapter 4 we studied a new metal carbide monolayer W_2C. Monolayer W_2C was stable in both 1T and 2H phases, but we preferred to the study the 2H phase because of its lower energy. This material is metallic, have reasonable Li/Na storage capacity, and superionic conductivity of the Li/Na ions. In chapter 5 we studied the unzipped graphene oxide (UGO) monolayer. Different studies have reported the UGO monolayer in different structures. We considered all its geometries based on the dipole alignment and calculated its energy and phonon stability. The zigzag antiferroelectric structure was found as the most stable structure for the UGO monolayer. We further studied the role of the oxygen lone pair electrons in the UGO via Wannier90. The pristine graphene is inert to Li adsorption. However, the oxygen injection creates the electron deficient and excess region where Li ions are trapped in the electron deficient regions. Furthermore, the UGO monolayer band structure has a Dirac cone similar to graphene, ensuring high electron and hole mobilities. In chapter 6 we exposed four new stable monolayers, MoC, WC, WS, and WSe. The buckled hexagonal structures and different building atoms produced a spontaneous out-ofplane polarization. High in-plane and out-of-plane piezoelectric coefficients were noticed by applying a uniaxial strain.

In chapter 7 monolayer SnS_2 and graphene were studied as an anode for Na ion batteries, individually and combinedly. The SnS_2 monolayer proved to have a high Na storage capacity and low diffusion barrier for Na diffusion. However, it showed a large expansion on sodiation. It also has poor electrical conductivity. On the other hand, graphene was metallic with high elastic stiffness, but its Na storage capacity is too low to be used as an anode. The SnS_2/graphene heterostructure stands an ideal anode material, having high Na storage capacity, high electrical conductivity, and low diffusion barrier. Similary in chapter 8, we considered the monolayer MoS_2 and VS_2 for Li/Na anode purposes. Besides the poor electrical conductivity of MoS_2, it has a low storage capacity of Li/Na ions. The monolayer VS_2 is metallic, and has a high Li/Na storage capacity, but due to its high chemical activity, it has not been prepared yet in expirement. The growth of VS_2 on MoS_2 stabilized the VS_2 layer and increased the Li/Na storage capacity of MoS_2. All this occures due to the charge redistribution in the formation of the nanocomposite.

References

[1] K. S. Novoselov, A. K. Geim, S. V. Morozov, D. Jiang, Y. Zhang, S. V. Dubonos, I. V. Grigorieva, and A. A. Firsov. Electric Field Effect in Atomically Thin Carbon Films. *Science*, 306:666–669, 2004.

[2] A. K. Geim and K. S. Novoselov. The rise of graphene. *Nat. Mater.*, 6:183–191, 2007.

[3] A. H. Castro Neto, F. Guinea, N. M. R. Peres, K. S. Novoselov, and A. K. Geim. The electronic properties of graphene. *Rev. Mod. Phys.*, 81:109–162, 2009.

[4] Frank Schwierz. Graphene transistors. *Nat. Mater.*, 5:487–496, 2010.

[5] Konstantin S Novoselov, VI Fal, L Colombo, PR Gellert, MG Schwab, K Kim, et al. A roadmap for graphene. *Nature*, 490:192, 2012.

[6] A. Bhattacharya, S. Bhattacharya, and G. P. Das. Band gap engineering by functionalization of BN sheet. *Phys. Rev. B*, 85:035415, 2012.

[7] Michael Naguib, Vadym N. Mochalin, Michel W. Barsoum, and Yury Gogotsi. 25th Anniversary Article: MXenes: A New Family of Two-Dimensional Materials. *Adv. Mater.*, 26:992–1005, 2014.

[8] Cheng Gong, Hengji Zhang, Weihua Wang, Luigi Colombo, Robert M. Wallace, and Kyeongjae Cho. Band alignment of two-dimensional transition metal dichalcogenides: Application in tunnel field effect transistors. *Appl. Phys. Lett.*, 103:053513, 2013.

[9] Sivacarendran Balendhran, Sumeet Walia, Hussein Nili, Sharath Sriram, and Madhu Bhaskaran. Elemental Analogues of Graphene: Silicene, Germanene, Stanene, and Phosphorene. *Small*, 11:640–652, 2015.

[10] Sajedeh Manzeli, Dmitry Ovchinnikov, Diego Pasquier, Oleg V. Yazyev, and Andras Kis. 2d transition metal dichalcogenides. *Nat. Rev. Mater.*, 2:17033, 2017.

[11] Michael A. McGuire. Crystal and Magnetic Structures in Layered, Transition Metal Dihalides and Trihalides. *Crystals*, 7:121, 2017.

[12] Babak Anasori, Maria R. Lukatskaya, and Yury Gogotsi. 2d metal carbides and nitrides (MXenes) for energy storage. *Nat. Rev. Mater.*, 2:16098, 2017.

[13] M. Neek-Amal, J. Beheshtian, A. Sadeghi, K. H. Michel, and F. M. Peeters. Boron Nitride Monolayer: A Strain-Tunable Nanosensor. *J. Phys. Chem. C*, 117:13261–13267, 2013.

[14] Y. C. Cheng, Z. Y. Zhu, W. B. Mi, Z. B. Guo, and U. Schwingenschlogl. Prediction of two-dimensional diluted magnetic semiconductors: Doped monolayer MoS_2 systems. *Phys. Rev. B*, 87:100401, 2013.

[15] K. S. Novoselov, A. K. Geim, S. V. Morozov, D. Jiang, M. I. Katsnelson, I. V. Grigorieva, S. V. Dubonos, and A. A. Firsov. Two-dimensional gas of massless Dirac fermions in graphene. *Nature*, 438:197–200, 2005.

[16] Liangzhi Kou, Yandong Ma, Ziqi Sun, Thomas Heine, and Changfeng Chen. Two-Dimensional Topological Insulators: Progress and Prospects. *J. Phys. Chem. Lett.*, 8:1905–1919, 2017.

[17] Z. S. Popovic, Jamshid Moradi Kurdestany, and S. Satpathy. Electronic structure and anisotropic Rashba spin-orbit coupling in monolayer black phosphorus. *Phys. Rev. B*, 92:035135, 2015.

[18] Moh. Adhib Ulil Absor, Iman Santoso, Harsojo, Kamsul Abraha, Hiroki Kotaka, Fumiyuki Ishii, and Mineo Saito. Strong Rashba effect in the localized impurity states of halogen-doped monolayer $ptse_2$. *Phys. Rev. B*, 97:205138, 2018.

[19] S. Cahangirov, M. Topsakal, E. Akturk, H. Sahin, and S. Ciraci. Two- and One-Dimensional Honeycomb Structures of Silicon and Germanium. *Phys. Rev. Lett.*, 102:236804, 2009.

[20] Patrick Vogt, Paola De Padova, Claudio Quaresima, Jose Avila, Emmanouil Frantzeskakis, Maria Carmen Asensio, Andrea Resta, Benedicte Ealet, and Guy Le Lay. Silicene: Compelling Experimental Evidence for Graphenelike Two-Dimensional Silicon. *Phys. Rev. Lett.*, 108:155501, 2012.

[21] Shunhong Zhang, Jian Zhou, Qian Wang, Xiaoshuang Chen, Yoshiyuki Kawazoe, and Puru Jena. Penta-graphene: A new carbon allotrope. *Proc. Natl. Acad. Sci. USA*, 112:2372–2377, 2015.

[22] Christopher P. Ewels, Xavier Rocquefelte, Harold W. Kroto, Mark J. Rayson, Patrick R. Briddon, and Malcolm I. Heggie. Predicting experimentally stable allotropes: Instability of penta-graphene. *Proc. Natl. Acad. Sci. USA*, 112:15609–15612, 2015.

[23] Akinola D. Oyedele, Shize Yang, Liangbo Liang, Alexander A. Puretzky, Kai Wang, Jingjie Zhang, Peng Yu, Pushpa R. Pudasaini, Avik W. Ghosh, Zheng Liu, Christopher M. Rouleau, Bobby G. Sumpter, Matthew F. Chisholm, Wu Zhou, Philip D. Rack, David B. Geohegan, and Kai Xiao. $PdSe_2$: Pentagonal Two-Dimensional Layers with High Air Stability for Electronics. *J. Am. Chem. Soc.*, 139:14090–14097, 2017.

[24] Keith T. Butler, Jarvist M. Frost, Jonathan M. Skelton, Katrine L. Svane, and Aron Walsh. Computational materials design of crystalline solids. *Chem. Soc. Rev.*, 45:6138–6146, 2016.

[25] Jesus Carrete, Wu Li, Lucas Lindsay, David A. Broido, Luis J. Gallego, and Natalio Mingo. Physically founded phonon dispersions of few-layer materials and the case of borophene. *Materials Research Letters*, 4:204–211, 2016.

[26] Bahadur Singh, Chuang-Han Hsu, Wei-Feng Tsai, Vitor M. Pereira, and Hsin Lin. Stable charge density wave phase in a 1T-$TiSe_2$ monolayer. *Phys. Rev. B*, 95:245136, 2017.

[27] Duane C Wallace. *Thermodynamics of crystals*. Courier Corporation, 1998.

[28] Felix Mouhat and Francois-Xavier Coudert. Necessary and sufficient elastic stability conditions in various crystal systems. *Phys. Rev. B*, 90:224104, 2014.

[29] Michael N. Blonsky, Houlong L. Zhuang, Arunima K. Singh, and Richard G. Hennig. Ab Initio Prediction of Piezoelectricity in Two-Dimensional Materials. *ACS Nano*, 9:9885–9891, 2015.

[30] Han Liu, Adam T. Neal, Zhen Zhu, Zhe Luo, Xianfan Xu, David Tomanek, and Peide D. Ye. Phosphorene: An Unexplored 2d Semiconductor with a High Hole Mobility. *ACS Nano*, 8:4033–4041, 2014.

[31] Gaoxue Wang, William J. Slough, Ravindra Pandey, and Shashi P. Karna. Degradation of phosphorene in air: understanding at atomic level. *2D Mater.*, 3:025011, 2016.

[32] Elisabeth Bianco, Sheneve Butler, Shishi Jiang, Oscar D. Restrepo, Wolfgang Windl, and Joshua E. Goldberger. Stability and Exfoliation of Germanane: A Germanium Graphane Analogue. *ACS Nano*, 7:4414–4421, 2013.

[33] Feng-feng Zhu, Wei-jiong Chen, Yong Xu, Chun-lei Gao, Dan-dan Guan, Can-hua Liu, Dong Qian, Shou-Cheng Zhang, and Jin-feng Jia. Epitaxial growth of two-dimensional stanene. *Nat. Mater.*, 14:1020–1025, 2015.

[34] Andrew J. Mannix, Xiang-Feng Zhou, Brian Kiraly, Joshua D. Wood, Diego Alducin, Benjamin D. Myers, Xiaolong Liu, Brandon L. Fisher, Ulises Santiago, Jeffrey R. Guest, Miguel Jose Yacaman, Arturo Ponce, Artem R. Oganov, Mark C. Hersam, and Nathan P. Guisinger. Synthesis of borophenes: Anisotropic, two-dimensional boron polymorphs. *Science*, 350:1513–1516, 2015.

[35] Lun Li, Zhong Chen, Ying Hu, Xuewen Wang, Ting Zhang, Wei Chen, and Qiang-bin Wang. Single-Layer Single-Crystalline SnSe Nanosheets. *J. Am. Chem. Soc.*, 135:1213–1216, 2013.

[36] Jiadong Zhou, Jia Shi, Qingsheng Zeng, Yu Chen, Lin Niu, Fucai Liu, Ting Yu, Kazu Suenaga, Xinfeng Liu, Junhao Lin, and Zheng Liu. InSe monolayer: synthesis, structure and ultra-high second-harmonic generation. *2D Mater.*, 5:025019, 2018.

[37] Ming-Wei Chen, HoKwon Kim, Dmitry Ovchinnikov, Agnieszka Kuc, Thomas Heine, Olivier Renault, and Andras Kis. Large-grain MBE-grown GaSe on GaAs with a Mexican hat-like valence band dispersion. *npj 2D Materials and Applications*, 2:2, 2018.

[38] L Seixas, AS Rodin, A Carvalho, and AH Castro Neto. Multiferroic two-dimensional materials. *Phys. Rev. Lett.*, 116:206803, 2016.

[39] Ernesto O. Wrasse and Tome M. Schmidt. Prediction of Two-Dimensional Topological Crystalline Insulator in PbSe Monolayer. *Nano Lett.*, 14:5717–5720, 2014.

[40] B. Radisavljevic, A. Radenovic, J. Brivio, V. Giacometti, and A. Kis. Single-layer MoS_2 transistors. *Nat. Nanotechnology*, 6:147–150, 2011.

[41] Noah F. Q. Yuan, Kin Fai Mak, and K.IT. Law. Possible topological superconducting phases of mos_2. *Phys. Rev. Lett.*, 113:097001, 2014.

[42] Xiaofeng Qian, Junwei Liu, Liang Fu, and Ju Li. Quantum spin Hall effect in two-dimensional transition metal dichalcogenides. *Science*, 346:1344–1347, 2014.

[43] Ashish Arora, Robert Schmidt, Robert Schneider, Maciej R. Molas, Ivan Breslavetz, Marek Potemski, and Rudolf Bratschitsch. Valley Zeeman Splitting and Valley Polarization of Neutral and Charged Excitons in Monolayer $MoTe_2$ at High Magnetic Fields. *Nano Lett.*, 16:3624–3629, 2016.

[44] Gerd Plechinger, Philipp Nagler, Ashish Arora, Robert Schmidt, Alexey Chernikov, Andres Granados del Aguila, Peter C. M. Christianen, Rudolf Bratschitsch, Christian Schhuller, and Tobias Korn. Trion fine structure and coupled spin-valley dynamics in monolayer tungsten disulfide. *Nat. Commun.*, 7:12715, 2016.

[45] Bin Ouyang, Shiyun Xiong, and Yuhang Jing. Tunable phase stability and contact resistance of monolayer transition metal dichalcogenides contacts with metal. *npj 2D Materials and Applications*, 2:13, 2018.

[46] Maria R. Lukatskaya, Olha Mashtalir, Chang E. Ren, Yohan DallYAgnese, Patrick Rozier, Pierre Louis Taberna, Michael Naguib, Patrice Simon, Michel W. Barsoum, and Yury Gogotsi. Cation Intercalation and High Volumetric Capacitance of Two-Dimensional Titanium Carbide. *Science*, 341:1502–1505, 2013.

[47] Jifeng Sun, Hongliang Shi, Theo Siegrist, and David J. Singh. Electronic, transport, and optical properties of bulk and mono-layer $PdSe_2$. *Appl. Phys. Lett.*, 107:153902, 2015.

[48] Qing Tang, Zhen Zhou, and Panwen Shen. *J. Am. Chem. Soc.*, 134:16909–16916, 2012.

[49] Olha Mashtalir, Michael Naguib, Vadym N. Mochalin, Yohan DallYAgnese, Min Heon, Michel W. Barsoum, and Yury Gogotsi. Intercalation and delamination of layered carbides and carbonitrides. *Nat. Commun.*, 4:1716, 2013.

[50] Abdus Samad, Aamir Shafique, Hye Jung Kim, and Young-Han Shin. Superionic and electronic conductivity in monolayer W_2C: Ab initio predictions. *J. Mater. Chem. A*, 5:11094–11099, 2017.

[51] Qilong Sun, Ying Dai, Yandong Ma, Tao Jing, Wei Wei, and Baibiao Huang. Ab Initio Prediction and Characterization of Mo_2C Monolayer as Anodes for Lithium-Ion and Sodium-Ion Batteries. *J. Phys. Chem. Lett.*, 7:937–943, 2016.

[52] Chuan Xu, Libin Wang, Zhibo Liu, Long Chen, Jingkun Guo, Ning Kang, Xiu-Liang Ma, Hui-Ming Cheng, and Wencai Ren. Large-area high-quality 2d ultrathin Mo_2c superconducting crystals. *Nat. Mater.*, 14:1135–1141, 2015.

[53] Xiaoming Zhang, Zhiming Yu, Shan-Shan Wang, Shan Guan, Hui Ying Yang, Yugui Yao, and Shengyuan A. Yang. Theoretical prediction of MoN_2 monolayer as a high capacity electrode material for metal ion batteries. *J. Mater. Chem. A*, 4:15224–15231, 2016.

[54] Ayeong Byeon, Meng-Qiang Zhao, Chang E. Ren, Joseph Halim, Sankalp Kota, Patrick Urbankowski, Babak Anasori, Michel W. Barsoum, and Yury Gogotsi. Two-Dimensional Titanium Carbide MXene As a Cathode Material for Hybrid Magnesium/Lithium-Ion Batteries. *ACS Appl. Mater. Interfaces*, 9:4296–4300, 2017.

[55] Xingshuai Lv, Wei Wei, Qilong Sun, Lin Yu, Baibiao Huang, and Ying Dai. Si_2C as a promising anode material with high mobility and capacity: A first principles study. *ChemPhysChem*, 18:1627–1634, 2017.

[56] Youngbin Lee, Yubin Hwang, and Yong-Chae Chung. Achieving Type I, II, and III Heterojunctions Using Functionalized MXene. *ACS Appl. Mater. Interfaces*, 7:7163–7169, 2015.

[57] Anand Chandrasekaran, Avanish Mishra, and Abhishek Kumar Singh. Ferroelectricity, Antiferroelectricity, and Ultrathin 2d Electron/Hole Gas in Multifunctional Monolayer MXene. *Nano Lett.*, 17:3290–3296, 2017.

[58] Mohammad Noor-A-Alam, Hamid Ullah, and Young-Han Shin. Switchable Polarization in Mn Embedded Graphene. *Sci. Rep.*, 8:4538, 2018.

[59] Liang Dong, Jun Lou, and Vivek B. Shenoy. Large In-Plane and Vertical Piezoelectricity in Janus Transition Metal Dichalchogenides. *ACS Nano*, 11:8242–8248, 2017.

[60] M. Menderes Alyoruk, Yierpan Aierken, Deniz Cakir, Francois M. Peeters, and Cem Sevik. Promising Piezoelectric Performance of Single Layer Transition-Metal Dichalcogenides and Dioxides. *J. Phys. Chem. C*, 119:23231–23237, 2015.

[61] Wenbin Li and Ju Li. Ferroelasticity and domain physics in two-dimensional transition metal dichalcogenide monolayers. *Nat. Commun.*, 7:10843, 2016.

[62] Ruixiang Fei, Wenbin Li, Ju Li, and Li Yang. Giant piezoelectricity of monolayer group IV monochalcogenides: SnSe, SnS, GeSe, and GeS. *Appl. Phys. Lett.*, 107:173104, 2015.

[63] Wenbin Li and Ju Li. Piezoelectricity in Two-dimensional Group-III Monochalcogenides. *Nano Res.*, 8:3796–3802, 2015.

[64] A. K. Geim and I. V. Grigorieva. Van der waals heterostructures. *Nature*, 499:419–425, 2013.

[65] Britton W. H. Baugher, Hugh O. H. Churchill, Yafang Yang, and Pablo Jarillo-Herrero. Optoelectronic devices based on electrically tunable sn diodes in a monolayer dichalcogenide. *Nat. Nanotechnol.*, 9:262–267, 2014.

[66] M. Born and R. Oppenheimer. Zur Quantentheorie der Molekeln. *Annalen der Physik*, 389:457–484, 1927.

[67] P. Hohenberg and W. Kohn. Inhomogeneous Electron Gas. *Phys. Rev.*, 136:B864–B871, 1964.

[68] W. Kohn and L. J. Sham. Self-Consistent Equations Including Exchange and Correlation Effects. *Phys. Rev.*, 140:A1133–A1138, 1965.

[69] P. E. Blochl. Projector augmented-wave method. *Phys. Rev. B*, 50:17953–17979, 1994.

[70] John P. Perdew, Kieron Burke, and Matthias Ernzerhof. Generalized Gradient Approximation Made Simple. *Phys. Rev. Lett.*, 77:3865–3868, 1996.

[71] K. Kim and K. D. Jordan. Comparison of Density Functional and MP2 Calculations on the Water Monomer and Dimer. *J. Phys. Chem.*, 98:10089–10094, 1994.

[72] M. Armand and J.-M. Tarascon. Building better batteries. *Nature*, 451:652–657, 2008.

[73] Jean-Marie Tarascon. Is lithium the new gold? *Nat Chem*, 2:510–510, 2010.

[74] M. Saiful Islam and Craig A. J. Fisher. Lithium and sodium battery cathode materials: computational insights into voltage, diffusion and nanostructural properties. *Chem. Soc. Rev.*, 43:185–204, 2014.

[75] Zhi Li, Jia Ding, and David Mitlin. Tin and tin compounds for sodium ion battery anodes: Phase transformations and performance. *Acc. Chem. Res.*, 48, 2015.

[76] Bruce Dunn, Haresh Kamath, and Jean-Marie Tarascon. Electrical Energy Storage for the Grid: A Battery of Choices. *Science*, 334:928–935, 2011.

[77] Veronica Palomares, Paula Serras, Irune Villaluenga, Karina B. Hueso, Javier Carretero-Gonzalez, and Teofilo Rojo. Na-ion batteries, recent advances and present challenges to become low cost energy storage systems. *Energy Environ. Sci.*, 5:5884–5901, 2012.

[78] Oleksandr I. Malyi, Teck L. Tan, and Sergei Manzhos. In search of high performance anode materials for Mg batteries: Computational studies of Mg in Ge, Si, and Sn. *J. Power Sources*, 233:341–345, 2013.

[79] Hyun Deog Yoo, Ivgeni Shterenberg, Yosef Gofer, Gregory Gershinsky, Nir Pour, and Doron Aurbach. Mg rechargeable batteries: an on-going challenge. *Energy Environ. Sci.*, 6:2265–2279, 2013.

[80] Dibakar Datta, Junwen Li, and Vivek B. Shenoy. Defective Graphene as a High-Capacity Anode Material for Na- and Ca-Ion Batteries. *ACS Appl. Mater. Interfaces*, 6:1788–1795, 2014.

[81] Meng-Chang Lin, Ming Gong, Bingan Lu, Yingpeng Wu, Di-Yan Wang, Mingyun Guan, Michael Angell, Changxin Chen, Jiang Yang, Bing-Joe Hwang, and Hongjie Dai. An ultrafast rechargeable aluminium-ion battery. *Nature*, 520:324–328, 2015.

[82] A. Ponrouch, C. Frontera, F. Barde, and M. R. Palacin. Towards a calcium-based rechargeable battery. *Nat. Mater.*, 15:169–172, 2016.

[83] Huilin Pan, Yong-Sheng Hu, and Liquan Chen. Room-temperature stationary sodium-ion batteries for large-scale electric energy storage. *Energy Environ. Sci.*, 6:2338–2360, 2013.

[84] Michael D. Slater, Donghan Kim, Eungje Lee, and Christopher S. Johnson. Sodium-Ion Batteries. *Adv. Funct. Mater.*, 23:947–958, 2013.

[85] Georgios A. Tritsaris, Efthimios Kaxiras, Sheng Meng, and Enge Wang. Adsorption and Diffusion of Lithium on Layered Silicon for Li-Ion Storage. *Nano Lett.*, 13:2258–2263, 2013.

[86] Yang Wen, Kai He, Yujie Zhu, Fudong Han, Yunhua Xu, Isamu Matsuda, Yoshitaka Ishii, John Cumings, and Chunsheng Wang. Expanded graphite as superior anode for sodium-ion batteries. *Nat. Commun.*, 5:4033, 2014.

[87] Sung Chul Jung, Dae Soo Jung, Jang Wook Choi, and Young-Kyu Han. Atom-Level Understanding of the Sodiation Process in Silicon Anode Material. *J. Phys. Chem. Lett.*, 5:1283–1288, 2014.

[88] Hualin Ye, Yeyun Wang, Feipeng Zhao, Wenjing Huang, Na Han, Junhua Zhou, Min Zeng, and Yanguang Li. Iron-based sodium-ion full batteries. *J. Mater. Chem. A*, 4:1754–1761, 2016.

[89] Hongyan Kang, Yongchang Liu, Kangzhe Cao, Yan Zhao, Lifang Jiao, Yijing Wang, and Huatang Yuan. Update on anode materials for Na-ion batteries. *J. Mater. Chem. A*, 3:17899–17913, 2015.

[90] Majid Mortazavi, Chao Wang, Junkai Deng, Vivek B. Shenoy, and Nikhil V. Medhekar. Ab initio characterization of layered MoS_2 as anode for sodium-ion batteries. *J. Power Sources*, 268:279–286, 2014.

[91] Ghulam Ali, Si Hyoung Oh, Se Young Kim, Ji Young Kim, Byung Won Cho, and Kyung Yoon Chung. An open-framework iron fluoride and reduced graphene oxide nanocomposite as a high-capacity cathode material for Na-ion batteries. *J. Mater. Chem. A*, 3:10258–10266, 2015.

[92] D. Duveau, S. Sananes Israel, J. Fullenwarth, F. Cunin, and L. Monconduit. Pioneer study of SiP_2 as negative electrode for Li- and Na-ion batteries. *J. Mater. Chem. A*, 4:3228–3232, 2016.

[93] Vadym V. Kulish, Oleksandr I. Malyi, Clas Persson, and Ping Wu. Phosphorene as an anode material for Na-ion batteries: a first-principles study. *Phys. Chem. Chem. Phys.*, 17:13921–13928, 2015.

[94] Yungang Zhou. MX (M = Ge, Sn; X = S, Se) sheets: theoretical prediction of new promising electrode materials for Li ion batteries. *J. Mater. Chem. A*, 4:10906–10913, 2016.

[95] Chen Ling and Fuminori Mizuno. Boron-doped graphene as a promising anode for Na-ion batteries. *Phys. Chem. Chem. Phys.*, 16:10419–10424, 2014.

[96] Manish Chhowalla, Hyeon Suk Shin, Goki Eda, Lain-Jong Li, Kian Ping Loh, and Hua Zhang. The chemistry of two-dimensional layered transition metal dichalcogenide nanosheets. *Nat. Chem.*, 5:263–275, 2013.

[97] Jingcang Su, Yong Pei, Zhenhua Yang, and Xianyou Wang. Ab initio study of graphene-like monolayer molybdenum disulfide as a promising anode material for rechargeable sodium ion batteries. *RSC Adv.*, 4:43183–43188, 2014.

[98] Pooja Rani and V. K. Jindal. Designing band gap of graphene by B and N dopant atoms. *RSC Adv.*, 3:802–812, 2012.

[99] Zhiyuan Zeng, Chaoliang Tan, Xiao Huang, Shuyu Bao, and Hua Zhang. Growth of noble metal nanoparticles on single-layer TiS_2 and TaS_2 nanosheets for hydrogen evolution reaction. *Energy Environ. Sci.*, 7:797–803, 2014.

[100] G. Kresse and J. Furthmuller. Efficient iterative schemes for ab initio total-energy calculations using a plane-wave basis set. *Phys. Rev. B*, 54:11169–11186, 1996.

[101] G. Kresse and D. Joubert. From ultrasoft pseudopotentials to the projector augmented-wave method. *Phys. Rev. B*, 59:1758, 1999.

[102] Aliaksandr V. Krukau, Oleg A. Vydrov, Artur F. Izmaylov, and Gustavo E. Scuseria. Influence of the exchange screening parameter on the performance of screened hybrid functionals. *J. Chem. Phys.*, 125:224106, 2006.

[103] Daniel Sheppard, Rye Terrell, and Graeme Henkelman. Optimization methods for finding minimum energy paths. *J. Chem. Phys.*, 128:134106, 2008.

[104] Min Yu and Dallas R. Trinkle. Accurate and efficient algorithm for Bader charge integration. *J. Chem. Phys.*, 134:064111, 2011.

[105] P. Chen, Y.-H. Chan, X.-Y. Fang, Y. Zhang, M. Y. Chou, S.-K. Mo, Z. Hussain, A.-V. Fedorov, and T.-C. Chiang. Charge density wave transition in single-layer titanium diselenide. *Nat. Commun.*, 6:8943, 2015.

[106] Chengyong Xu, Paul A. Brown, and Kevin L. Shuford. Strain-induced semimetal-to-semiconductor transition and indirect-to-direct band gap transition in monolayer 1T-TiS_2. *RSC Adv.*, 5:83876–83879, 2015.

[107] Kapildeb Dolui and Stefano Sanvito. Dimensionality-driven phonon softening and incipient charge density wave instability in TiS_2. *EPL*, 115(4):47001, 2016.

[108] Dinh Loc Duong, Gihun Ryu, Alexander Hoyer, Chengtian Lin, Marko Burghard, and Klaus Kern. Raman Characterization of the Charge Density Wave Phase of 1T-$TiSe_2$: From Bulk to Atomically Thin Layers. *ACS Nano*, 11:1034–1040, 2017.

[109] Clotilde S. Cucinotta, Kapildeb Dolui, Henrik Pettersson, Quentin M. Ramasse, Edmund Long, Sean E. O Brian, Valeria Nicolosi, and Stefano Sanvito. Electronic Properties and Chemical Reactivity of TiS_2 Nanoflakes. *J. Phys. Chem. C*, 119:15707–15715, 2015.

[110] Abdus Samad, Mohammad Noor-A-Alam, and Young-Han Shin. First principles study of a SnS_2/graphene heterostructure: a promising anode material for rechargeable Na ion batteries. *J. Mater. Chem. A*, 4:14316–14323, 2016.

[111] K. Born, M. Huang. *Dynamical Theory of Crystal Lattices*. Oxford.

[112] Kristin Persson, Yoyo Hinuma, Ying Shirley Meng, Anton Van der Ven, and Gerbrand Ceder. Thermodynamic and kinetic properties of the Li-graphite system from first-principles calculations. *Phys. Rev. B*, 82:125416, 2010.

[113] G. Ceder, G. Hautier, A. Jain, and S.p. Ong. Recharging lithium battery research with first-principles methods. *MRS Bulletin*, 36:185–191, 2011.

[114] Feng Li, Yuanyuan Qu, and Mingwen Zhao. Germanium sulfide nanosheet: a universal anode material for alkali metal ion batteries. *J. Mater. Chem. A*, 4:8905–8912, 2016.

[115] Xiao Liu, Yanwei Wen, Zhengzheng Chen, Bin Shan, and Rong Chen. A first-principles study of sodium adsorption and diffusion on phosphorene. *Phys. Chem. Chem. Phys.*, 17:16398–16404, 2015.

[116] Xiuqiang Xie, Zhimin Ao, Dawei Su, Jinqiang Zhang, and Guoxiu Wang. MoS_2/Graphene Composite Anodes with Enhanced Performance for Sodium-Ion Batteries: The Role of the Two-Dimensional Heterointerface. *Adv. Funct. Mater.*, 25:1393–1403, 2015.

[117] Gen-Cai Guo, Da Wang, Xiao-Lin Wei, Qi Zhang, Hao Liu, Woon-Ming Lau, and Li-Min Liu. First-Principles Study of Phosphorene and Graphene Heterostructure as Anode Materials for Rechargeable Li Batteries. *J. Phys. Chem. Lett.*, 6:5002–5008, 2015.

[118] Zhixiao Liu, Huiqiu Deng, and Partha P. Mukherjee. Evaluating Pristine and Modified SnS_2 as a Lithium-Ion Battery Anode: A First-Principles Study. *ACS Appl. Mater. Interfaces*, 7:4000–4009, 2015.

[119] A. V. Pogrebnyakov, J. M. Redwing, J. E. Jones, X. X. Xi, S. Y. Xu, Qi Li, V. Vaithyanathan, and D. G. Schlom. Thickness dependence of the properties of epitaxial MgB_2 thin films grown by hybrid physical-chemical vapor deposition. *Appl. Phys. Lett.*, 82:4319–4321, 2003.

[120] Yi-Hsien Lee, Xin-Quan Zhang, Wenjing Zhang, Mu-Tung Chang, Cheng-Te Lin, Kai-Di Chang, Ya-Chu Yu, Jacob Tse-Wei Wang, Chia-Seng Chang, Lain-Jong Li, and Tsung-Wu Lin. Synthesis of Large-Area MoS_2 Atomic Layers with Chemical Vapor Deposition. *Adv. Mater.*, 24:2320–2325, 2012.

[121] Gints Kucinskis, Gunars Bajars, and Janis Kleperis. Graphene in lithium ion battery cathode materials: A review. *J. Power Sources*, 240:66–79, 2013.

[122] A. Sengupta, R. K. Ghosh, and S. Mahapatra. Performance Analysis of Strained Monolayer MOSFET. *IEEE Transactions on Electron Devices*, 60:2782–2787, 2013.

[123] Yongji Gong, Junhao Lin, Xingli Wang, Gang Shi, Sidong Lei, Zhong Lin, Xiaolong Zou, Gonglan Ye, Robert Vajtai, Boris I. Yakobson, Humberto Terrones, Mauricio Terrones, Beng Kang Tay, Jun Lou, Sokrates T. Pantelides, Zheng Liu, Wu Zhou, and Pulickel M. Ajayan. Vertical and in-plane heterostructures from WS_2/MoS_2 monolayers. *Nat. Mater.*, 13:1135–1142, 2014.

[124] Chunming Huang, Sanfeng Wu, Ana M. Sanchez, Jonathan J. P. Peters, Richard Beanland, Jason S. Ross, Pasqual Rivera, Wang Yao, David H. Cobden, and Xiaodong Xu. Lateral heterojunctions within monolayer $MoSe_2$@WSe_2 semiconductors. *Nat. Mater.*, 13:1096–1101, 2014.

[125] Ming-Hui Chiu, Chendong Zhang, Hung-Wei Shiu, Chih-Piao Chuu, Chang-Hsiao Chen, Chih-Yuan S. Chang, Chia-Hao Chen, Mei-Yin Chou, Chih-Kang Shih, and Lain-Jong Li. Determination of band alignment in the single-layer MoS_2/WSe_2 heterojunction. *Nat. Commun.*, 6:7666, 2015.

[126] Rinaldo Raccichini, Alberto Varzi, Stefano Passerini, and Bruno Scrosati. The role of graphene for electrochemical energy storage. *Nat. Mater.*, 14:271–279, 2015.

[127] Xiao-Xiao Zhang, Yumeng You, Shu Yang Frank Zhao, and Tony F. Heinz. Experimental evidence for dark excitons in monolayer WSe_2. *Phys. Rev. Lett.*, 115:257403, 2015.

[128] Peter G. Bruce, Bruno Scrosati, and Jean-Marie Tarascon. Nanomaterials for Rechargeable Lithium Batteries. *Angew. Chem. Int. Ed.*, 47:2930–2946, 2008.

[129] Ying Shirley Meng and M. Elena Arroyo-de Dompablo. First principles computational materials design for energy storage materials in lithium ion batteries. *Energy Environ. Sci.*, 2:589–609, 2009.

[130] M. Saiful Islam and Craig A. J. Fisher. Lithium and sodium battery cathode materials: computational insights into voltage, diffusion and nanostructural properties. *Chem. Soc. Rev.*, 43:185–204, 2013.

[131] Sung You Hong, Youngjin Kim, Yuwon Park, Aram Choi, Nam-Soon Choi, and Kyu Tae Lee. Charge carriers in rechargeable batteries: Na ions vs. Li ions. *Energy Environ. Sci.*, 6:2067–2081, 2013.

[132] Deniz Cakir, Cem Sevik, Oguz Gulseren, and Francois M. Peeters. Mo_2C as a high capacity anode material: a first-principles study. *J. Mater. Chem. A*, 4:6029–6035, 2016.

[133] Naoki Nitta, Feixiang Wu, Jung Tae Lee, and Gleb Yushin. Li-ion battery materials: present and future. *Materials Today*, 18:252–264, 2015.

[134] Yi Zhang, Yusheng Zhao, and Changfeng Chen. Ab initio study of the stabilities of and mechanism of superionic transport in lithium-rich antiperovskites. *Phys. Rev. B*, 87:134303, 2013.

[135] Yan Wang, William Davidson Richards, Shyue Ping Ong, Lincoln J. Miara, Jae Chul Kim, Yifei Mo, and Gerbrand Ceder. Design principles for solid-state lithium superionic conductors. *Nat. Mater.*, 14:1026–1031, 2015.

[136] Xujie Lu, John W. Howard, Aiping Chen, Jinlong Zhu, Shuai Li, Gang Wu, Paul Dowden, Hongwu Xu, Yusheng Zhao, and Quanxi Jia. Antiperovskite Li_3ocl Superionic Conductor Films for Solid-State Li-Ion Batteries. *Adv. Sci.*, 3:1500359, 2016.

[137] Sung Chul Jung, Jang Wook Choi, and Young-Kyu Han. Anisotropic Volume Expansion of Crystalline Silicon during Electrochemical Lithium Insertion: An Atomic Level Rationale. *Nano Lett.*, 12:5342–5347, 2012.

[138] Jian Lin, Zhiwei Peng, Changsheng Xiang, Gedeng Ruan, Zheng Yan, Douglas Natelson, and James M. Tour. Graphene Nanoribbon and Nanostructured SnO_2 Composite Anodes for Lithium Ion Batteries. *ACS Nano*, 7:6001–6006, 2013.

[139] Tyler Stephenson, Zhi Li, Brian Olsen, and David Mitlin. Lithium ion battery applications of molybdenum disulfide (MoS_2) nanocomposites. *Energy Environ. Sci.*, 7:209–231, 2013.

[140] Jingjing Wang, Chao Luo, Jianfeng Mao, Yujie Zhu, Xiulin Fan, Tao Gao, Alice C. Mignerey, and Chunsheng Wang. Solid-State Fabrication of SnS_2/C Nanospheres for High-Performance Sodium Ion Battery Anode. *ACS Appl. Mater. Interfaces*, 7:11476–11481, 2015.

[141] Xiaoli Sun, Zhiguo Wang, Zhijie Li, and Y. Q. Fu. Origin of Structural Transformation in Mono- and Bi-Layered Molybdenum Disulfide. *Sci. Rep.*, 6:26666, 2016.

[142] Zhong-Shuai Wu, Wencai Ren, Li Xu, Feng Li, and Hui-Ming Cheng. Doped Graphene Sheets As Anode Materials with Superhigh Rate and Large Capacity for Lithium Ion Batteries. *ACS Nano*, 5:5463–5471, 2011.

[143] Xiaofeng Fan, W.T. Zheng, and Jer-Lai Kuo. Adsorption and Diffusion of Li on Pristine and Defective Graphene. *ACS App. Mater. Interfaces*, 4:2432–2438, 2012.

[144] Yuanyue Liu, Vasilii I. Artyukhov, Mingjie Liu, Avetik R. Harutyunyan, and Boris I. Yakobson. Feasibility of Lithium Storage on Graphene and Its Derivatives. *J. Phys. Chem. Lett.*, 4:1737–1742, 2013.

[145] Yuanyue Liu, Y. Morris Wang, Boris I. Yakobson, and Brandon C. Wood. Assessing Carbon-Based Anodes for Lithium-Ion Batteries: A Universal Description of Charge-Transfer Binding. *Phys. Rev. Lett.*, 113:028304, 2014.

[146] Wenyu Yuan, Yani Zhang, Laifei Cheng, Heng Wu, Lianxi Zheng, and Donglin Zhao. The applications of carbon nanotubes and graphene in advanced rechargeable lithium batteries. *J. Mater. Chem. A*, 4:8932–8951, 2016.

[147] Jiajie Zhu and Udo Schwingenschlogl. Silicene for Na-ion battery applications. *2D Mater.*, 3:035012, 2016.

[148] Atsushi Togo, Fumiyasu Oba, and Isao Tanaka. First-principles calculations of the ferroelastic transition between rutile-type and $CaCl_2$-type SiO_2 at high pressures. *Phys. Rev. B*, 78:134106, 2008.

[149] W. Tang, E. Sanville, and G. Henkelman. A grid-based Bader analysis algorithm without lattice bias. *J. Phys.: Condens. Matter*, 21:084204, 2009.

[150] Changgu Lee, Xiaoding Wei, Jeffrey W. Kysar, and James Hone. Measurement of the Elastic Properties and Intrinsic Strength of Monolayer Graphene. *Science*, 321:385–388, 2008.

[151] Ryan C. Cooper, Changgu Lee, Chris A. Marianetti, Xiaoding Wei, James Hone, and Jeffrey W. Kysar. Nonlinear elastic behavior of two-dimensional molybdenum disulfide. *Phys. Rev. B*, 87:035423, 2013.

[152] Houlong L. Zhuang and Richard G. Hennig. Theoretical perspective of photocatalytic properties of single-layer SnS_2. *Phys. Rev. B*, 88:115314, 2013.

[153] Naoki Nitta and Gleb Yushin. High-Capacity Anode Materials for Lithium-Ion Batteries: Choice of Elements and Structures for Active Particles. *Part. Part. Syst. Charact.*, 31:317–336, 2014.

[154] N. M. R. Peres. Colloquium: The transport properties of graphene: An introduction. *Rev. Mod. Phys.*, 82:2673–2700, 2010.

[155] M. F. Craciun, I. Khrapach, M. D. Barnes, and S. Russo. Properties and applications of chemically functionalized graphene. *J. Phys.: Condens. Matter*, 25:423201–423222, 2013.

[156] Wei Feng, Peng Long, Yiyu Feng, and Yu Li. Two-Dimensional Fluorinated Graphene: Synthesis, Structures, Properties and Applications. *Adv. Sci.*, 3:1500413–1500435, 2016.

[157] Sid Megahed and Bruno Scrosati. Lithium-ion rechargeable batteries. *J. Power Sources*, 51:79–104, 1994.

[158] Abdus Samad and Young-Han Shin. MoS_2@VS_2 Nanocomposite as a Superior Hybrid Anode Material. *ACS Appl. Mater. Interfaces*, 9:29942–29949, 2017.

[159] F. Bonino, S. Brutti, P. Reale, B. Scrosati, L. Gherghel, J. Wu, and K. Mullen. A Disordered Carbon as a Novel Anode Material in Lithium-Ion Cells. *Adv. Mater.*, 17:743–746, 2005.

[160] Jian-Tao Wang, Hongming Weng, Simin Nie, Zhong Fang, Yoshiyuki Kawazoe, and Changfeng Chen. Body-Centered Orthorhombic C_{16}: A Novel Topological Node-Line Semimetal. *Phys. Rev. Lett.*, 116:195501–195506, 2016.

[161] Junyi Liu, Shuo Wang, and Qiang Sun. All-carbon-based porous topological semimetal for Li-ion battery anode material. *PNAS*, 114:651–656, 2017.

[162] Eunseok Lee and Kristin A. Persson. Li Absorption and Intercalation in Single Layer Graphene and Few Layer Graphene by First Principles. *Nano Lett.*, 12:4624–4628, 2012.

[163] Xiaofeng Fan, W. T. Zheng, Jer-Lai Kuo, and David J. Singh. Adsorption of Single Li and the Formation of Small Li Clusters on Graphene for the Anode of Lithium-Ion Batteries. *ACS Appl. Mater. Interfaces*, 5:7793–7797, 2013.

[164] Handan Yildirim, Alper Kinaci, Zhi-Jian Zhao, Maria K. Y. Chan, and Jeffrey P. Greeley. First-Principles Analysis of Defect-Mediated Li Adsorption on Graphene. *ACS Appl. Mater. Interfaces*, 6:21141–21150, 2014.

[165] Rahul P. Hardikar, Deya Das, Sang Soo Han, Kwang-Ryeol Lee, and Abhishek K. Singh. Boron doped defective graphene as a potential anode material for Li-ion batteries. *Phys. Chem. Chem. Phys.*, 16:16502–16508, 2014.

[166] Liujiang Zhou, Z. F. Hou, Bo Gao, and Thomas Frauenheim. Doped graphenes as anodes with large capacity for lithium-ion batteries. *J. Mater. Chem. A*, 4:13407–13413, 2016.

[167] Bo Xiao, Yan-chun Li, Xue-fang Yu, and Jian-bo Cheng. Penta-graphene: A Promising Anode Material as the Li/Na-Ion Battery with Both Extremely High Theoretical Capacity and Fast Charge/Discharge Rate. *ACS Appl. Mater. Interfaces*, 8:35342–35352, 2016.

[168] Meysam Makaremi, Bohayra Mortazavi, and Chandra Veer Singh. Carbon ene-yne graphyne monolayer as an outstanding anode material for Li/Na ion batteries. *App. Mater. Today*, 10:115–121, 2018.

[169] Bohayra Mortazavi, Masoud Shahrokhi, Xiaoying Zhuang, and Timon Rabczuk. Boron-graphdiyne: a superstretchable semiconductor with low thermal conductivity and ultrahigh capacity for Li, Na and Ca ion storage. *J. Mater. Chem. A*, 6:11022–11036, 2018.

[170] Vivekanand Shukla, Rafael B. Araujo, Naresh K. Jena, and Rajeev Ahuja. The curious case of two dimensional Si_2BN: A high-capacity battery anode material. *Nano Energy*, 41:251–260, 2017.

[171] Stefan Grimme, Jens Antony, Stephan Ehrlich, and Helge Krieg. A consistent and accurate ab initio parametrization of density functional dispersion correction (DFT-D) for the 94 elements H-Pu. *J. Chem. Phys.*, 132:154104–154123, 2010.

[172] Arash A. Mostofi, Jonathan R. Yates, Young-Su Lee, Ivo Souza, David Vanderbilt, and Nicola Marzari. Wannier90: A tool for obtaining maximally-localised Wannier functions. *Computer Physics Communications*, 178:685–699, 2008.

[173] Nicola Marzari, Arash A. Mostofi, Jonathan R. Yates, Ivo Souza, and David Vanderbilt. Maximally localized Wannier functions: Theory and applications. *Rev. Mod. Phys.*, 84:1419–1475, 2012.

[174] Arash A. Mostofi, Jonathan R. Yates, Giovanni Pizzi, Young-Su Lee, Ivo Souza, David Vanderbilt, and Nicola Marzari. An updated version of wannier90: A fool for obtaining maximally-localised Wannier functions. *Computer Physics Communications*, 185:2309–2310, 2014.

[175] V. Krukau, A. Vydrov Aliaksandr, F. Izmaylov Oleg, E. Scuseria Artur, and Gustavo. Influence of the exchange screening parameter on the performance of screened hybrid functionals. *J. Chem. Phys.*, 125:224106–224111, 2006.

[176] Geoffrey W. Rogers and Jefferson Z. Liu. High-Performance Graphene Oxide Electromechanical Actuators. *J. Am. Chem. Soc.*, 134:1250–1255, 2012.

[177] Mohammad Noor-A-Alam and Young-Han Shin. Switchable polarization in an unzipped graphene oxide monolayer. *Phys. Chem. Chem. Phys.*, 18:20443–20449, 2016.

[178] Zhenyue Chang, Wenyi Yan, Jin Shang, and Jefferson Zhe Liu. Piezoelectric properties of graphene oxide: A first-principles computational study. *Appl. Phys. Lett.*, 105:023103–023105, 2014.

[179] Geoffrey W. Rogers and Jefferson Z. Liu. Monolayer Graphene Oxide as a Building Block for Artificial Muscles. *Appl. Phys. Lett.*, 102:021903–021907, 2013.

[180] Zhenyue Chang, Junkai Deng, Ganaka G. Chandrakumara, Wenyi Yan, and Jefferson Zhe Liu. Two-dimensional shape memory graphene oxide. *Nat. Commun.*, 7:11972–11981, 2016.

[181] Zhenyue Chang, Junkai Deng, Ganaka G. Chandrakumara, Wenyi Yan, and Jefferson Zhe Liu. Two-way actuation of graphene oxide arising from quantum mechanical effects. *Appl. Phys. Lett.*, 109:143902–243907, 2016.

[182] Mingjie Liu, Alex Kutana, Yuanyue Liu, and Boris I. Yakobson. First-Principles Studies of Li Nucleation on Graphene. *J. Phys. Chem. Lett.*, 5:1225–1229, 2014.

[183] I. A. Courtney, J. S. Tse, Ou Mao, J. Hafner, and J. R. Dahn. Ab initio calculation of the lithium-tin voltage profile. *Phys. Rev. B*, 58:15583–15588, 1998.

[184] D. Carlier, A. Van der Ven, C. Delmas, and G. Ceder. First-Principles Investigation of Phase Stability in the O_2-$LiCoO_2$ System. *Chem. Mater.*, 15:2651–2660, 2003.

[185] Heejin Kim, Dong Jun Kim, Dong-Hwa Seo, Min Sun Yeom, Kisuk Kang, Do Kyung Kim, and Yousung Jung. Ab Initio Study of the Sodium Intercalation and Intermediate Phases in $Na_{0.44}MnO_2$ for Sodium-Ion Battery. *Chem. Mater.*, 24:1205–1211, 2012.

[186] Xiaoli Sun and Zhiguo Wang. Sodium adsorption and diffusion on monolayer black phosphorus with intrinsic defects. *App. Sur. Sci.*, 427:189–197, 2018.

[187] Weifeng Li, Yanmei Yang, Gang Zhang, and Yong-Wei Zhang. Ultrafast and Directional Diffusion of Lithium in Phosphorene for High-Performance Lithium-Ion Battery. *Nano Lett.*, 15:1691–1697, 2015.

[188] Xiaoli Sun, Zhiguo Wang, and Y. Q. Fu. Defect-Mediated Lithium Adsorption and Diffusion on Monolayer Molybdenum Disulfide. *Sci. Rep.*, 5:18712, 2015.

[189] Xin Tan, Carlos R. Cabrera, and Zhongfang Chen. Metallic BSi_3 Silicene: A Promising High Capacity Anode Material for Lithium-Ion Batteries. *J. Phys. Chem. C*, 118:25836–25843, 2014.

[190] Di Xiao, Wang Yao, and Qian Niu. Valley-Contrasting Physics in Graphene: Magnetic Moment and Topological Transport. *Phys. Rev. Lett.*, 99:236809, 2007.

[191] Chuanhong Jin, Fang Lin, Kazu Suenaga, and Sumio Iijima. Fabrication of a Freestanding Boron Nitride Single Layer and Its Defect Assignments. *Phys. Rev. Lett.*, 102:195505, 2009.

[192] K. F. Mak, K. L. McGill, J. Park, and P. L. McEuen. Valleytronics. The valley Hall effect in MoS_2 transistors. *Science (New York, N.Y.)*, 344:1489–1492, 2014.

[193] Cong Mai, Andrew Barrette, Yifei Yu, Yuriy G. Semenov, Ki Wook Kim, Linyou Cao, and Kenan Gundogdu. Many-Body Effects in Valleytronics: Direct Measurement of Valley Lifetimes in Single-Layer MoS_2. *Nano Lett.*, 14:202–206, 2014.

[194] D. Lee, H. Lu, Y. Gu, S.-Y. Choi, S.-D. Li, S. Ryu, T. R. Paudel, K. Song, E. Mikheev, S. Lee, S. Stemmer, D. A. Tenne, S. H. Oh, E. Y. Tsymbal, X. Wu, L.-Q. Chen, A. Gruverman, and C. B. Eom. Emergence of room-temperature ferroelectricity at reduced dimensions. *Science*, 349:1314–1317, 2015.

[195] G. Zheng, R. Shankaran, M. A. Orgun, L. Qiao, and K. Saleem. Ideas and Challenges for Securing Wireless Implantable Medical Devices: A Review. *IEEE Sensors Journal*, 17:562–576, 2017.

[196] Karel-Alexander N. Duerloo, Mitchell T. Ong, and Evan J. Reed. Intrinsic Piezoelectricity in Two-Dimensional Materials. *J. Phys. Chem. Lett.*, 3:2871–2876, 2012.

[197] Wenhui Wan, Chang Liu, Wende Xiao, and Yugui Yao. Promising ferroelectricity in 2d group IV tellurides: a first-principles study. *Appl. Phys. Lett.*, 111:132904, 2017.

[198] Hanyu Zhu, Yuan Wang, Jun Xiao, Ming Liu, Shaomin Xiong, Zi Jing Wong, Ziliang Ye, Yu Ye, Xiaobo Yin, and Xiang Zhang. Observation of piezoelectricity in free-standing monolayer MoS_2. *Nat. Nanotechnol.*, 10:151–155, 2015.

[199] Sharmila N. Shirodkar and Umesh V. Waghmare. Emergence of ferroelectricity at a metal-semiconductor transition in a 1T monolayer of MoS_2. *Phys. Rev. Lett.*, 112:157601–157606, 2014.

[200] Ruixiang Fei, Wei Kang, and Li Yang. Detection of b-Mode Polarization at Degree Angular Scales by BICEP2. *Phys. Rev. Lett.*, 112:241101, 2014.

[201] Menghao Wu and Xiao Cheng Zeng. Intrinsic Ferroelasticity and/or Multiferroicity in Two-Dimensional Phosphorene and Phosphorene Analogues. *Nano Lett.*, 16:3236–3241, 2016.

[202] Mitchell T. Ong and Evan J. Reed. Engineered Piezoelectricity in Graphene. *ACS Nano*, 6:1387, 2012.

[203] Bo Xu, Hui Xiang, Yidong Xia, Kun Jiang, Xiangang Wan, Jun He, Jiang Yin, and Zhiguo Liu. Monolayer $AgBiP_2Se_6$: an atomically thin ferroelectric semiconductor with out-plane polarization. *Nanoscale*, 9:8427–8434, 2017.

[204] Yu Guo, Si Zhou, Yizhen Bai, and Jijun Zhao. Enhanced piezoelectric effect in Janus group-III chalcogenide monolayers. *Appl. Phys. Lett.*, 110:163102, 2017.

[205] M. E. Davila, L. Xian, S. Cahangirov, A. Rubio, and G. Le Lay. Germanene: a novel two-dimensional germanium allotrope akin to graphene and silicene. *New J. Phys.*, 16:095002, 2014.

[206] Yvon Le Page and Paul Saxe. Symmetry-general least-squares extraction of elastic data for strained materials from ab initio calculations of stress. *Phys. Rev. B*, 65:104104, 2002.

[207] Jia-An Yan, W. Y. Ruan, and M. Y. Chou. Phonon dispersions and vibrational properties of monolayer, bilayer, and trilayer graphene: Density-functional perturbation theory. *Phys. Rev. B*, 77:125401, 2008.

[208] K. H. Michel and B. Verberck. Theory of elastic and piezoelectric effects in two-dimensional hexagonal boron nitride. *Phys. Rev. B*, 80:224301, 2009.

[209] H. Sahin, S. Cahangirov, M. Topsakal, E. Bekaroglu, E. Akturk, R. T. Senger, and S. Ciraci. Monolayer honeycomb structures of group-IV elements and III-V binary compounds: First-principles calculations. *Phys. Rev. B*, 80:155453–155465, 2009.

[210] Bo Peng, Hao Zhang, Hezhu Shao, Yuanfeng Xu, Gang Ni, Rongjun Zhang, and Heyuan Zhu. Phonon transport properties of two-dimensional group-IV materials from ab initio calculations. *Phys. Rev. B*, 94:245420, 2016.

[211] Alejandro Molina-Sanchez and Ludger Wirtz. Phonons in single-layer and few-layer MoS_2 and WS_2. *Phys. Rev. B*, 84:155413, 2011.

[212] Céline Lichtensteiger, Jean-Marc Triscone, Javier Junquera, and Philippe Ghosez. Ferroelectricity and tetragonality in ultrathin $PbTiO_3$ films. *Phys. Rev. Lett.*, 94:047603, 2005.

[213] A. Kandemir and H. Sahin. Janus single layers of In_2SSe: A first-principles study. *Phys. Rev. B*, 97:155410, 2018.

[214] Deniz Cakir, Francois M Peeters, and Cem Sevik. Mechanical and thermal properties of h-MX_2 (M= Cr, Mo, W; X= O, S, Se, Te) monolayers: A comparative study. *Appl. Phys. Lett.*, 104:203110, 2014.

[215] Hye Jung Kim, Mohammad Noor-A-Alam, and Young-Han Shin. Piezoelectric enhancement by surface effect in hydrofluorinated graphene bilayer. *J. App. Phys.*, 117:145304, 2015.

[216] Domenico Di Sante, Alessandro Stroppa, Paolo Barone, Myung-Hwan Whangbo, and Silvia Picozzi. Emergence of Ferroelectricity and Spin-Valley Properties in Two-Dimensional Honeycomb Binary Compounds. *Phys. Rev. B*, 91:161401, 2015.

[217] D Vanderbilt. Berry-phase theory of proper piezoelectric response. *J. Phys. Chem. Solids*, 61:147–151, 2000.

[218] Ting Cao, Zhenglu Li, and Steven G Louie. Tunable magnetism and half-metallicity in hole-doped monolayer gase. *Phys. Rev. Lett.*, 114:236602, 2015.

[219] Ming-Wei Chen, HoKwon Kim, Dmitry Ovchinnikov, Agnieszka Kuc, Thomas Heine, Olivier Renault, and Andras Kis. Large-grain mbe-grown gase on gaas with a mexican hat-like valence band dispersion. *npj 2D Materials and Applications*, 2:2, 2018.

[220] Naoaki Yabuuchi, Kei Kubota, Mouad Dahbi, and Shinichi Komaba. Research Development on Sodium-Ion Batteries. *Chem. Rev.*, 114:11636–11682, 2014.

[221] Mouad Dahbi, Naoaki Yabuuchi, Kei Kubota, Kazuyasu Tokiwa, and Shinichi Komaba. Negative electrodes for Na-ion batteries. *Phys. Chem. Chem. Phys.*, 16:15007, 2014.

[222] B. L. Ellis, W. R. M. Makahnouk, Y. Makimura, K. Toghill, and L. F. Nazar. A multifunctional 3.5 V iron-based phosphate cathode for rechargeable batteries. *Nat. Mater.*, 6:749–753, 2007.

[223] Yasuharu Okamoto. Density Functional Theory Calculations of Alkali Metal (Li, Na, and K) Graphite Intercalation Compounds. *J. Phys. Chem. C*, 118:16–19, 2014.

[224] D. P. DiVincenzo and E. J. Mele. Cohesion and structure in stage-1 graphite intercalation compounds. *Phys. Rev. B*, 32:2538–2553, 1985.

[225] Eunjeong Yang, Hyunjun Ji, and Yousung Jung. Two-Dimensional Transition Metal Dichalcogenide Monolayers as Promising Sodium Ion Battery Anodes. *J. Phys. Chem. C*, 119:26374–26380, 2015.

[226] Yu Jing, Zhen Zhou, Carlos R. Cabrera, and Zhongfang Chen. Metallic VS_2 Monolayer: A Promising 2d Anode Material for Lithium Ion Batteries. *J. Phys. Chem. C*, 117:25409–25413, 2013.

[227] Ruimin Sun, Qiulong Wei, Qidong Li, Wen Luo, Qinyou An, Jinzhi Sheng, Di Wang, Wei Chen, and Liqiang Mai. Vanadium Sulfide on Reduced Graphene Oxide Layer as a Promising Anode for Sodium Ion Battery. *ACS Appl. Mater. Interfaces*, 7:20902–20908, 2015.

[228] Yandong Zhang, Peiyi Zhu, Liliang Huang, Jian Xie, Shichao Zhang, Gaoshao Cao, and Xinbing Zhao. Few-Layered SnS_2 on Few-Layered Reduced Graphene Oxide as Na-Ion Battery Anode with Ultralong Cycle Life and Superior Rate Capability. *Adv. Funct. Mater.*, 25:481–489, 2015.

[229] Lamuel David, Romil Bhandavat, and Gurpreet Singh. MoS_2/Graphene Composite Paper for Sodium-Ion Battery Electrodes. *ACS Nano*, 8:1759–1770, 2014.

[230] Chaoji Chen, Yanwei Wen, Xianluo Hu, Xiulei Ji, Mengyu Yan, Liqiang Mai, Pei Hu, Bin Shan, and Yunhui Huang. Na^+ intercalation pseudocapacitance in graphene-coupled titanium oxide enabling ultra-fast sodium storage and long-term cycling. *Nat. Commun.*, 6:6929, 2015.

[231] Baihua Qu, Chuze Ma, Ge Ji, Chaohe Xu, Jing Xu, Ying Shirley Meng, Taihong Wang, and Jim Yang Lee. Layered SnS_2-Reduced Graphene Oxide Composite: A High-Capacity, High-Rate, and Long-Cycle Life Sodium-Ion Battery Anode Material. *Adv. Mater.*, 26:3854–3859, 2014.

[232] Yongchang Liu, Hongyan Kang, Lifang Jiao, Chengcheng Chen, Kangzhe Cao, Yijing Wang, and Huatang Yuan. Exfoliated-SnSb restacked on graphene as a high-capacity, high-rate, and long-cycle life anode for sodium ion batteries. *Nanoscale*, 7:1325–1332, 2015.

[233] Graeme Henkelman and Hannes Jonsson. Improved tangent estimate in the nudged elastic band method for finding minimum energy paths and saddle points. *J. Chem. Phys.*, 113:9978–9985, 2000.

[234] R. A. Olsen, G. J. Kroes, G. Henkelman, A. Arnaldsson, and H. Jonsson. Comparison of methods for finding saddle points without knowledge of the final states. *J. Chem. Phys.*, 121:9776–9792, 2004.

[235] C. Bacaksiz, S. Cahangirov, A. Rubio, R. T. Senger, F. M. Peeters, and H. Sahin. Bilayer SnS_2: Tunable stacking sequence by charging and loading pressure. *Phys. Rev. B*, 93:125403, 2016.

[236] Yongchang Liu, Ning Zhang, Lifang Jiao, Zhanliang Tao, and Jun Chen. Ultrasmall Sn Nanoparticles Embedded in Carbon as High-Performance Anode for Sodium-Ion Batteries. *Adv. Funct. Mater.*, 25:214–220, 2015.

[237] Martin Winter, Jurgen O. Besenhard, Michael E. Spahr, and Petr Novak. Insertion Electrode Materials for Rechargeable Lithium Batteries. *Adv. Mater.*, 10:725–763, 1998.

[238] Deniz Cakir, Cem Sevik, Oguz Gulseren, and Francois M. Peeters. Mo_2c as a high capacity anode material: a first-principles study. *J. Mater. Chem. A*, 4:6029–6035, 2016.

[239] Sascha Thinius, Mazharul M. Islam, Paul Heitjans, and Thomas Bredow. Theoretical Study of Li Migration in Lithium-Graphite Intercalation Compounds with Dispersion-Corrected DFT Methods. *J. Phys. Chem. C*, 118:2273–2280, 2014.

[240] Yucheng Huang, Chongyi Ling, Xi Chen, Danmei Zhou, and Sufan Wang. SnS_2 nanotubes: a promising candidate for the anode material for lithium ion batteries. *RSC Adv.*, 5:32505–32510, 2015.

[241] Yafei Li, Dihua Wu, Zhen Zhou, Carlos R. Cabrera, and Zhongfang Chen. Enhanced Li Adsorption and Diffusion on MoS_2 Zigzag Nanoribbons by Edge Effects: A Computational Study. *J. Phys. Chem. Lett.*, 3:2221–2227, 2012.

[242] David M. Guzman and Alejandro Strachan. Role of strain on electronic and mechanical response of semiconducting transition-metal dichalcogenide monolayers: An ab-initio study. *J. Appl. Phys.*, 115:243701, 2014.

[243] Doron Aurbach, Bryan D. McCloskey, Linda F. Nazar, and Peter G. Bruce. Advances in understanding mechanisms underpinning lithium-air batteries. *Nat. Energy*, 1:16128, 2016.

[244] Juliette Billaud, Florian Bouville, Tommaso Magrini, Claire Villevieille, and Andre R. Studart. Magnetically aligned graphite electrodes for high-rate performance Li-ion batteries. *Nat. Energy*, 1:16097, 2016.

[245] C. P. Grey and J. M. Tarascon. Sustainability and in situ monitoring in battery development. *Nat. Mater.*, 16(1):45–56, 2017.

[246] Qing Hua Wang, Kourosh Kalantar-Zadeh, Andras Kis, Jonathan N. Coleman, and Michael S. Strano. Electronics and optoelectronics of two-dimensional transition metal dichalcogenides. *Nat. Nanotechnology*, 7, 2012.

[247] Andrea Splendiani, Liang Sun, Yuanbo Zhang, Tianshu Li, Jonghwan Kim, Chi-Yung Chim, Giulia Galli, and Feng Wang. Emerging Photoluminescence in Monolayer MoS_2. *Nano Lett.*, 10:1271–1275, 2010.

[248] Kin Fai Mak, Keliang He, Jie Shan, and Tony F. Heinz. Control of valley polarization in monolayer MoS_2 by optical helicity. *Nat. Nanotechnology*, 7:494–498, 2012.

[249] H. Ochoa and R. Roldan. Spin-orbit-mediated spin relaxation in monolayer MoS_2. *Phys. Rev. B*, 87:245421, 2013.

[250] Di Xiao, Gui-Bin Liu, Wanxiang Feng, Xiaodong Xu, and Wang Yao. Coupled Spin and Valley Physics in Monolayers of MoS_2 and Other Group-VI Dichalcogenides. *Phys. Rev. Lett.*, 108:196802, 2012.

[251] Kai Leng, Zhongxin Chen, Xiaoxu Zhao, Wei Tang, Bingbing Tian, Chang Tai Nai, Wu Zhou, and Kian Ping Loh. Phase Restructuring in Transition Metal Dichalcogenides for Highly Stable Energy Storage. *ACS Nano*, 10:9208–9215, 2016.

[252] Wenpei Kang, Yuyu Wang, and Jun Xu. Recent progress in layered metal dichalcogenide nanostructures as electrodes for high-performance sodium-ion batteries. *J. Mater. Chem. A*, 5:7667–7690, 2017.

[253] Jeffry Setiadi, Matthew D. Arnold, and Michael J. Ford. Li-Ion Adsorption and Diffusion on Two-Dimensional Silicon with Defects: A First Principles Study. *ACS App. Mater. Interfaces*, 5:10690–10695, 2013.

[254] Chandra Chowdhury, Sharmistha Karmakar, and Ayan Datta. Capping Black Phosphorene by h-BN Enhances Performances in Anodes for Li and Na Ion Batteries. *ACS Energy Lett.*, 1:253–259, 2016.

[255] Xiji Shao, Kedong Wang, Rui Pang, and Xingqiang Shi. Lithium Intercalation in Graphene/MoS_2 Composites: First-Principles Insights. *J. Phys. Chem. C*, 119:25860–25867, 2015.

[256] Kun Chang and Weixiang Chen. In situ synthesis of MoS_2/graphene nanosheet composites with extraordinarily high electrochemical performance for lithium ion batteries. *Chem. Commun.*, 47:4252–4254, 2011.

[257] Kun Chang and Weixiang Chen. L-cysteine-assisted synthesis of layered MoS_2/graphene composites with excellent electrochemical performances for lithium ion batteries. *ACS Nano*, 5:4720–4728, 2011.

[258] Yu Jing, Zhen Zhou, Carlos R. Cabrera, and Zhongfang Chen. Graphene, inorganic graphene analogs and their composites for lithium ion batteries. *J. Mater. Chem. A*, 2:12104–12122, 2014.

[259] Stefan Grimme. Semiempirical GGA-type density functional constructed with a long-range dispersion correction. *J. Comput. Chem.*, 27:1787, 2006.

[260] H. S. S. Ramakrishna Matte, A. Gomathi, Arun K. Manna, Dattatray J. Late, Ranjan Datta, Swapan K. Pati, and C. N. R. Rao. MoS_2 and WS_2 analogues of Graphene. *Angew. Chem. Int. Ed.*, 49:4059–4062, 2010.

[261] Houlong L. Zhuang and Richard G. Hennig. Stability and magnetism of strongly correlated single-layer VS_2. *Phys. Rev. B*, 93:054429, 2016.

[262] Eric B. Isaacs and Chris A. Marianetti. Electronic correlations in monolayer VS_2. *Phys. Rev. B*, 94:035120, 2016.

[263] Jun Feng, Xu Sun, Changzheng Wu, Lele Peng, Chenwen Lin, Shuanglin Hu, Jinlong Yang, and Yi Xie. Metallic Few-Layered VS_2 Ultrathin Nanosheets: High Two-Dimensional Conductivity for In-Plane Supercapacitors. *J. Am. Chem. Soc.*, 133:17832–17838, 2011.

[264] Jun Feng, Lele Peng, Changzheng Wu, Xu Sun, Shuanglin Hu, Chenwen Lin, Jun Dai, Jinlong Yang, and Yi Xie. Giant Moisture Responsiveness of VS_2 Ultrathin Nanosheets for Novel Touchless Positioning Interface. *Adv. Mater.*, 24:1969–1974, 2012.

[265] Kin Fai Mak, Changgu Lee, James Hone, Jie Shan, and Tony F. Heinz. Atomically Thin MoS_2: A New Direct-Gap Semiconductor. *Phys. Rev. Lett.*, 105:136805, 2010.

[266] Darwin Barayang Putungan, Shi-Hsin Lin, and Jer-Lai Kuo. Metallic VS_2 Monolayer Polytypes as Potential Sodium-Ion Battery Anode via ab Initio Random Structure Searching. *ACS App. Mater. Interfaces*, 8:18754–18762, 2016.

[267] Fatih Ersan, Gokhan Gokolu, and Ethem Akturk. Adsorption and Diffusion of Lithium on Monolayer Transition Metal Dichalcogenides $MoS_{2(1-x)}Se_{2x}$ Alloys. *J. Phys. Chem. C*, 119:28648–28653, 2015.

[268] Abdus Samad, Aamir Shafique, and Young-Han Shin. Adsorption and diffusion of mono, di, and trivalent ions on two-dimensional TiS_2. *Nanotechnology*, 28:175401, 2017.

[269] Xudong Zhao, Xu Zhang, Dihua Wu, Haichang Zhang, Fei Ding, and Zhen Zhou. Ab initio investigations on bulk and monolayer V_2O_5 as cathode materials for Li-, Na-, K- and Mg-ion batteries. *J. Mater. Chem. A*, 4:16606–16611, 2016.

[270] Sharmistha Karmakar, Chandra Chowdhury, and Ayan Datta. Two-Dimensional Group IV Monochalcogenides: Anode Materials for Li-Ion Batteries. *J. Phys. Chem. C*, 2016.